UNIVERSITÀ
DI SIENA
1240

Faculty of Mathematical, Physical and Natural Sciences
Department of Physics
Ph.D. thesis in Experimental Physics
XXIV Cycle

Measurement of the forward charged particle pseudorapidity density in pp collisions at $\sqrt{s} = 7$ TeV with the TOTEM experiment.

Submitted in partial fulfilment of the requirements for the degree of
Doctor of Philosophy in Experimental Physics

Thesis Advisors:

Dr. Lami Stefano

Candidate:

Dr. Berretti Mirko

Tutor:

Prof. Scribano Angelo

Abstract: The TOTEM experiment at the LHC is dedicated to the precise measurement of the total pp cross section, to the study of the elastic scattering and of the diffractive interactions. The TOTEM T2 telescope, composed of triple GEM chambers, provides the tracking of the charged particles produced by the inelastic pp interactions in the pseudorapidity range $5.3<|\eta|<6.5$.
In this thesis the offline procedures developed for the event reconstruction in the T2 telescope are reported. They include the tuning of the detector simulation, the track reconstruction algorithm and their characterisation in terms of physics performance. The detector alignment algorithms are also described and the uncertainties on the misalignment parameters are quantified. The thesis is then focused on the measurement of the charged particle pseudorapidity density ($dN_{ch}/d\eta$) obtained in T2 for inelastic pp collisions at $\sqrt{s} = 7$ TeV. This extends the analogous measurement performed by the other LHC experiments to the previously unexplored forward η region. The measurement refers to more than 99% of non-diffractive processes and to single and double diffractive processes with diffractive masses above ~3.4 GeV/c^2, corresponding to about 95% of the total inelastic cross-section. The $dN_{ch}/d\eta$ has been found to decrease with $|\eta|$, from 3.84 ± 0.01(stat) ± 0.37(syst) at $|\eta| = 5.375$ to 2.38 ± 0.01(stat) ± 0.21(syst) at $|\eta| = 6.375$. Several MC generators have been compared to data, most of them have been found to not fully describe the measurement.

Contents

List of Figures

List of Tables

Introduction

The TOTEM experiment at the LHC has been designed to measure the total pp cross section at 14 TeV with an uncertainty of about 1 mb. Moreover the experiment aims to study the elastic scattering on a wide range of four momentum transfer ($10^{-3} < |t| < 10$ GeV^2) and the diffractive dissociation. The T2 telescope, one of the three TOTEM subsystems, is among the most forward trackers ever installed in a collider experiment. It is based on Gas Electron Multiplier (GEM) chambers and can detect the charged particles produced in the inelastic collisions with a polar angle in the range of 3-10 mrad. The experiment is fully operative and has already carried out several important analyses on pp collisions at 7 TeV, as the elastic differential cross section, the total cross section and the forward charged particle density.

In this thesis I report the analysis activities I have done related to the T2 detector. During my Ph.D. studies I had the opportunity to follow the development of the analysis and event reconstruction algorithms currently used in T2 since the very beginning.

When I started the Ph.D. program the installation of the first T2 quarter in the LHC tunnel was ongoing. At that time many of the calibration routines and of the monitoring programs had to be developed. The implementation of these algorithms allowed to have a first feeling on how the pp collisions in the harsh environment of the LHC look like. The settings of the read out chips and of the GEM chambers were optimised in a subsequent period of intense detector commissioning. But there were still several basic quantities which seemed sensibly different from our expectation. The detector occupancy was a factor 6 or more larger than what expected in the simulation and the parameters of the first reconstructed tracks were clearly incompatible with the primary vertex position of the collision.

The simulation of the detector and of the material placed between T2 and IP were therefore revised and tuned carefully. Passive materials as the beam pipe and the inner part of the Hadron Forward (HF) calorimeter of the CMS experiment were found to be responsible for the production of a large amount of secondary particles which arrive in T2. The digitization model was modified and tuned with the data observables. The clustering, hit finding and track finding algorithms were rewritten in order to cope with this more challenging scenario.

Because of the long distance of the T2 detector from the interaction point ($\sim$14 m) it was soon understood that small misalignments of the detector quarters could have a large impact on the parameters of reconstructed tracks which don't point anymore to the IP. This strongly affects the effective selection capability of the primary particles. Proper detector alignment algorithms, allowing to correct for relative movements of the planes inside one quarter and for coherent quarters movements with respect to their nominal position, were therefore developed. This work has been fundamental in order to approach the physics analysis that is reported in this thesis: the measurement of the forward charged particle density ($dN_{CH}/d\eta$) with T2 [1].

Strong interaction processes characterised a small ("soft") four momentum transfer belong to the realm of non-perturbative QCD, which is one of the major unsolved problems in particle physics. Since QCD cannot provide a complete description of the soft hadron interactions, experimental measurements are highly valuable because they represent a guide for the phenomenological models which try to describe these processes.

Moreover, the measurement of the very forward pp $dN_{CH}/d\eta$ is also important to better understand some properties of the soft interaction which occurs when partons with a low fraction of the proton momentum (x) are involved. In particular, there is a theoretical interest in the study of the processes where gluon saturation effects can be probed.

In addition, precise measurements on the forward particles multiplicity and pseudorapidity density are expected to be extremely important also for the improvement of the analyses on very high energy cosmic rays (CR), which heavily rely on the Monte Carlo (MC) description of the showers generated when a CR interacts in the atmosphere.

The measurement of the $dN_{ch}/d\eta$ presented in this thesis refers to inelastic events triggered by T2 in pp collisions at a center of mass energy of 7 TeV, with charged particles reconstructed in the pseudorapidity range $5.3 < |\eta| < 6.4$. This represents the most forward pseudorapidity density ever measured at a collider, obtained in a more challenging experimental condition with respect to the analogous measurements performed by other LHC experiments in the central region, where particles can be tracked very precisely with detectors placed very close to the IP.

When compared to our measurement, the most popular MC generators frequently used in the analysis of collider experiments underestimate the forward particle production, while a better agreement has been found with the prediction of some MC generators commonly used in the CR analyses. A possible explanation could be that the energy dependence of the multiple parton interaction that is assumed in some MC generators is not so accurate and it should be improved.

This thesis is structured as follows:

- Chapter 1 provides an introduction to the physics of soft hadronic interactions. The Eikonal and Regge models, two of the elastic models whose basic idea are currently used even in the most modern descriptions of the elastic interactions, are presented. Important exact relations as the asymptotic bounds and the optical theorem are reported. Several historical models developed for the description and the prediction of the multiplicity and the pseudorapidity density are introduced. These include the Fermi, Landau and Feynman models for the pseudorapidity density and the KNO scaling for the particle multiplicity. The hypothesis of the “extended longitudinal scaling”, already observed in the pseudorapidity density distributions measured in the past, is emphasised as it can be potentially tested with T2. An explanation of this phenomenon in terms of the CGC theory is also mentioned.

- Chapter 2 describes the TOTEM experimental apparatus and the main objectives of the TOTEM physics program. Particular emphasis is given to the description of the T2 detector. The measurements achieved by the experiment at the time of writing are also briefly summarised.

- Chapter 3 reports the work done on the event simulation and reconstruction. The tuning of the digitization models with the data is described together with all the offline procedures that have been developed to reconstruct the event in T2. These include in particular the hit and the track reconstruction algorithms, which are then characterised in terms of their efficiency and resolution with analyses performed on data and on tuned MC simulations. The tracking algorithm has been designed in order to cope with the large amount of secondary particles entering T2. It is able to detect the inelastic events with at least a charged particle generated in the T2 acceptance with an efficiency larger than 99%. The primary track efficiency, which is defined as the efficiency to reconstruct the primary track with parameters still compatible with the vertex position, depends both on the tracking algorithm performance and on the effect that the magnetic field and the passive material have on the particle propagation from the IP to T2. The primary track efficiency was found to depend on the detector occupancy and it is larger than 80% at the average inelastic particle occupancy measured in the data.

- Chapter 4 focuses on the detector alignment. The methods used to align the planes internally to the quarter, the two quarters of an arm with respect to themselves and each quarter with respect to the IP are explained in detail. The uncertainty on the misalignment parameters, of fundamental importance as they represent one of the main biases in the $dN_{ch}/d\eta$ measurement in T2, are evaluated with MC studies. The procedure implemented in order to correct the reconstructed hit position for such misalignment biases is also described in detail. It was optimised in order to minimise the distortion induced by the misalignment correction on the track parameters due to the finite detector resolution.

- Chapter 5 reports the analysis of the charged particle pseudorapidity density measurement. The analysis corrections needed are explained and the associated errors are quantified. The largest contributions to the uncertainty of the measurement are given by the error on the global misalignment parameters and by the track efficiency estimation. While the former is due to the effect that small residual misalignments have on the parameters used to select the primary tracks with the smallest angles, the latter is amplified by the large detector occupancy which makes the primary track reconstruction more difficult and the simulation less reliable. Another important source of systematic error is given by the secondary particle contamination that may be included in the $dN_{ch}/d\eta$ measurement: even if the separation is made directly on data, part of the background can be disentangled from the primary contribution only by using statistical factors suggested by MC generators, which were found to predict different values. Despite the final and conservative $\sim$10% systematic uncertainty, the measurement shows discrimination capability among the different MC generators.

  The achieved measurement has also been compared with the pseudorapidity density measurements obtained by the other LHC experiments.

  The perspective for further measurements on which I'm currently involved, to be performed in the near future with T2, is finally reported. In particular the possibility that TOTEM now has to take data with a common TOTEM-CMS trigger allows us to plan a rich program of physics analyses that can be performed for the first time at such forward pseudorapidities. This includes the studies of forward multiplicities in the underlying event and of hard diffraction. The forward particle $dN_{ch}/d\eta$ obtained in pA interaction at 8 TeV is another topic which is of high interest but feasibility studies on this measurement, which is even more challenging due to the larger detector occupancy with respect to the pp case, are ongoing.

Chapter 1

Physics of soft hadron interactions

In this chapter important theoretical results achieved in the field of the soft hadronic interactions are described. Several phenomenological models that have been used in the past to describe the data are also presented. There is still no ab-initio theory capable to describe the pp interaction at small t[1]. To describe completely the data, phenomenological considerations need always to be introduced and some of the parameters used in the models cannot be predicted but have to be fitted on the measurements.

On the other hand there are rigorous theoretical concepts which regulate some aspects of the soft interaction like the behaviour that some experimental quantities should have at asymptotic energies or the exact relations and bounds which correlate the observables (see sec. 1.1). An example of a theoretical milestone is given by the optical theorem (see sec.1.1.1). The Eikonal model and the Regge theory are presented in sec. 1.2. Although only the original ideas of these models are reported, they still constitute the basis for many phenomenological theories currently used to describe the pp elastic scattering and total cross section.

When a hard partonic interaction occurs, the inelastic hadron-hadron scattering can be described in the framework of the pQCD with the factorisation theorem (see sec. 1.3.1). The description is however limited only to the hard part of the process: as an example the

---

[1] In a two body scattering $1+2 \rightarrow 3+4$, defining the $4-$momentum of the particles with p_i, the kinematics can be described using the Lorentz invariant Mandelstam variables (s, t, u), defined as:

$$s = (p_1 + p_2)^2 = (p_3 + p_4)^2$$

$$t = (p_1 - p_3)^2 = (p_2 - p_4)^2$$

$$u = (p_1 - p_4)^2 = (p_2 - p_3)^2$$

Therefore s represents the square of the center of mass energy and t is the $4-$momentum transfer squared. This notation will be maintained hereafter in the text.

dynamics of the underlying events as well as the hadronisation processes cannot be rigorously described. These processes are usually taken into account with phenomenological models implemented in MC programs (see sec. 1.3.3). One of the aim of the measurement reported in this thesis is indeed to improve the tuning of these models in the very forward region.

The charged particle pseudorapidity distribution and the charged particle multiplicity were extensively measured in the past by several collaborations. A brief account of the experimental results obtained at lower energies is reported in sec. 1.3.6, while in sec. 1.3.4 few “historical” models used to describe these quantities are reported. A special emphasis is given to the “extended longitudinal scaling” phenomena (see sec. 1.3.5). This is one interesting property related to the $dN_{ch}/d\eta$ distribution where the low-x dynamics (see sec. 1.3.2), a regime which is of high interest for the physics community, can be probed.

1.1 Fundamental theorems

Several solid results which allow the theoretical description of the hadron-hadron interaction were already derived before the development of the QCD theory and its establishment as the main theory for the strong interaction. In this section only a few of them are reported, as they are appropriate for the context of this thesis. They had been obtained using very basic principles like unitarity, analiticity of the scattering amplitudes and crossing symmetry. Therefore they will remain valid independently the dynamical theory or model that will be used in the description of the scattering processes.

1.1.1 Optical theorem

In the framework of the S-matrix formalism for the relativistic scattering [2], by using the unitarity condition (i.e. the relation imposing that the sum of all the transition probabilities from the initial state to the final state is 1), the following relation can be derived:

$$2ImT_{if} = \sum_{n} T^{*}_{fn} T_{in} \tag{1.1}$$

where T is the transition matrix of the process, i and f indicate initial and final states, n represents one of the possible n-particle states obtained starting from the initial state. Eq.

1.1 can be rewritten in terms of the scattering amplitude A_{if}:

$$2ImT_{if} = \sum_n \int d\Pi_n A^*_{fn} A_{in} \tag{1.2}$$

where $d\Pi_n$ is the n-particle phase space. In case of $i = f$, where all the quantum numbers remain the same during the collision (elastic scattering at t=0), the previous expression reduces to:

$$2ImT_{if}(s, t = 0) = \sum_n \int d\Pi_n |A_{in}|^2 \tag{1.3}$$

The right hand side of the equation is proportional, a part for a factor s, to the total cross section (σ_{tot}). The following fundamental relation can be therefore obtained:

$$\sigma_{tot} = \frac{1}{s} ImA_{el}(s, t = 0) \tag{1.4}$$

known as the optical theorem. The relation 1.4 can be rewritten by means of experimental measurable quantities introducing ρ which is the ratio between the real and the imaginary part of the elastic amplitude at $t = 0$. Therefore:

$$\frac{d\sigma_{el}}{dt}|_{t=0} = \frac{1}{16\pi\, s^2}|A(s, 0)|^2 = \frac{1}{16\pi\, s^2}|ImA_{el}(s, t = 0)|^2(1 + \rho^2) = \sigma^2_{tot}\frac{1}{16\pi}(1 + \rho^2) \tag{1.5}$$

Combining eq. 1.5 with the basic relation:

$$N_{el} + N_{inel} = L\sigma_{tot} \tag{1.6}$$

(where L is the luminosity, N_{el} and N_{inel} are the elastic and inelastic rates), the total cross section can be obtained in terms of experimental rates, independently on the luminosity. Substituting for L in eq. 1.5 gives:

$$\sigma_{tot} = \frac{16\pi}{1 + \rho^2} \frac{dN_{el}/dt|_{t=0}}{N_{el} + N_{inel}} \tag{1.7}$$

which will be used by the TOTEM experiment for the luminosity-independent σ_{tot} measurement. It is important to remind that using dispersion relations it is possible to relate the real part of the elastic amplitude to its imaginary part. However, the imaginary part at $t = 0$ is related to the total cross section by the optical theorem. As a consequence, it is possible to write the parameter ρ at a given energy as an integral of the total cross section over the energy. Such an integral relation can be approximated by a local expression relating ρ

to the derivative of σ_{tot} with respect to energy:

$$\rho \simeq \pi/(2\sigma_{tot})\frac{d\sigma_{tot}}{d\,lns} \tag{1.8}$$

The relation 1.8 can be very useful to experimentally determine the ρ value [3].

1.1.2 Asymptotic theorems

General considerations based on the properties that the scattering amplitude must have at very high energy allowed the formulation of several rigorous theorems which regulate the behaviour of the hadron scattering in the asymptotic energy regime. One of the most important is the Froissart-Martin bound which states that the total cross section of any hadron-hadron scattering cannot grow faster than $ln^2\, s$:

$$\sigma_{tot} < C\, ln^2 s \ \text{ if } \ s \rightarrow \infty \tag{1.9}$$

where C is a constant and s is in GeV. This theorem put a bound on how fast a cross section can grow with the energy, in the asymptotic region. The constant C is bounded and it is known that it should be larger than 60 mb. Therefore the theorem doesn't constitute an effective constraint at the energy reached so far. The measurements performed in the past, including the TOTEM measurement, predict a growth of the cross section which can saturate or exceed the $ln^2 s$ limit, see for example fig. 1.1, but the magnitude of the cross section is still too small in order to be bounded from this theorem.

The Pomeranchuck theorem for the total cross section states that asymptotically the particle-particle and the particle-antiparticle cross sections became equal.

$$\sigma_{tot}(ab) = \sigma_{tot}(a\bar{b}) \ \text{ if } \ s \rightarrow \infty \tag{1.10}$$

Cornell-Martin theorem states that the equality relation between particle-particle and particle-antiparticle observables holds also for the quantity $B = \frac{d}{dt}(ln\frac{d\sigma_{el}}{dt})|_{t=0}$. Measurements on total hadron-hadron cross section shown that the equality foreseen by the Pomeranchuck theorem was already reached at the previous collider experiments, as shown in fig. 1.2 where the difference between the particle-particle and particle-antiparticle total cross section seems to decrease like $1/\sqrt{s}$.

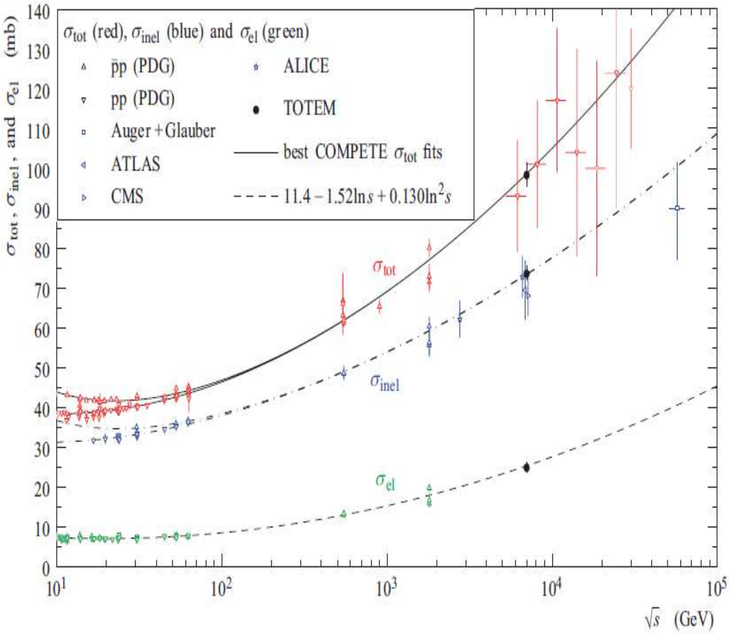

Figure 1.1: Total, elastic and inelastic pp and $p\bar{p}$ cross section data as a function of the center of mass energy. The TOTEM points [4] obtained at $\sqrt{s} = 7$ TeV are shown, together with the phenomenological fit from the COMPETE collaboration [5].

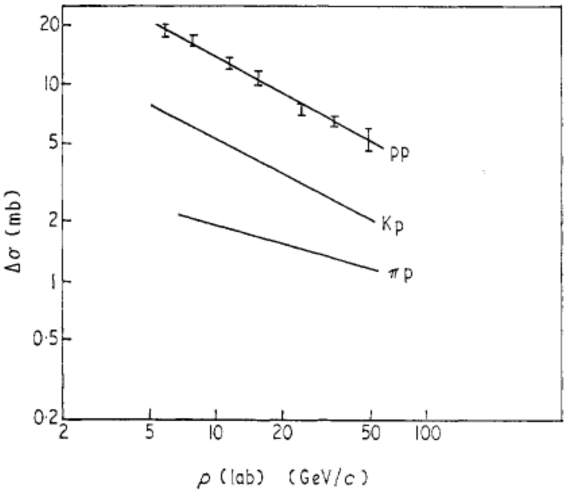

Figure 1.2: $\Delta\sigma = \sigma_{tot}(\bar{a}, p) - \sigma_{tot}(a, p)$ where $\bar{a}, a$ denote $\bar{p}, p$ or K^-, K^+ or π^-, π^+ as a function of the laboratory momentum [6].

1.2 Non perturbative models for total and elastic cross section

1.2.1 Eikonal models

The Eikonal approximation has been introduced for the first time in non relativistic quantum mechanics, for the solution of the scattering problem of a wave by a potential V with finite range *a* and with strength much smaller than the kinetic energy E_k of the particle [2]. In this condition, if *k* is the particle wavelength, the relations $ka >> 1$ and $E_k >> V(r)$ hold. For small scattering angles it can be shown that the Schrödinger equation for the elastic scattering is solved with the following scattering amplitude f:

$$f(k,\theta,\phi) = \frac{ik}{2\pi}\int d^2\mathbf{b}e^{-i\mathbf{qb}}(1 - e^{i\chi(\mathbf{b})}) \tag{1.11}$$

where θ, ϕ is the polar and azimuthal angle of the scattered particle, **b** is a 2D vector perpendicular to the incident propagation (impact parameter), **q** is the 4-momentum transfer, and χ is the "eikonal function" defined in terms of the reduced potential $U = V\ 2\mu/\hbar^2$ as:

$$\chi(\mathbf{b}) = \frac{-1}{2k}\int_{-\infty}^{+\infty} U(\mathbf{b}, z)dz \tag{1.12}$$

where μ is the reduced mass of the system and z is the direction of the incident propagation. The solution has the same form of the one obtained in optics in the studies of the scattering of the light wave by a hole, in the limit of the Fraunhofer diffraction. To maintain this analogy, the profile function $\Gamma(b)$, which in optics describes the geometrical shape of the hole where diffraction happens is defined as:

$$\Gamma(b) = 1 - e^{i\chi(\mathbf{b})} \tag{1.13}$$

If the diffraction of the light is due to an opaque obstacle having the same shape of the hole described by $\Gamma(b)$, the same formulae for the amplitudes hold with the replacement of Γ by the opacity of the obstacle S defined as $S = 1 - \Gamma(b)$. It can be shown that $\Gamma(\mathbf{b})$ is the Fourier transform in the momentum-transfer space of the scattering amplitude $f(\mathbf{q})$, and assuming azimuthal isotropy eq. 1.11 can be rewritten as the Fourier-Bessel transform of Γ:

$$f(k,\theta) = ik\int db\, bJ_0(kb\theta)\Gamma(k,b) \tag{1.14}$$

The elastic cross section σ_{el} can be therefore written as:

$$\sigma_{el} = \int d^2\mathbf{b}|\Gamma(\mathbf{b})|^2 \tag{1.15}$$

while, by using the optical theorem, σ_{inel} and σ_{tot} are:

$$\sigma_{inel} = \int d^2\mathbf{b}[2Re\Gamma(\mathbf{b}) - |\Gamma(\mathbf{b})|^2] \tag{1.16}$$

$$\sigma_{tot} = \int d^2\mathbf{b} 2 Re \Gamma(\mathbf{b}) \tag{1.17}$$

This representation of the amplitudes and of the cross section, useful since it maintains an intuitive relation between the observables and the scattering-potential, is still valid in the description of the relativistic scattering. The Eikonal function is substituted by the "opacity" Ω through $-i\chi(b) \leftrightarrow \Omega(s,b)$, which is now assumed to be also function of the scattering energy s. It is worthy to notice that for a hadron of size R with infinite opacity ($\Omega \rightarrow \infty$) the cross sections reduce to the suggestive black disk limit (see eq. 1.15-1.17):

$$\sigma_{el} = \sigma_{inel} = \frac{1}{2}\sigma_{tot} = \pi\, R^2 \tag{1.18}$$

The dependence on s is not predicted from any theory: indeed many models aim to predict the functional dependence that the opacity or the profile function should have on s. For example, assuming that the scattering amplitude A(s,t) can be described experimentally by:

$$A(s,t) = is\sigma_{tot}\, e^{B(s)t/2} \tag{1.19}$$

then, thanks to the relation (analogous to 1.11) $A(s,t) = 2is \int d^2\mathbf{b} e^{-i\mathbf{qb}}(1 - e^{-\Omega(s,\mathbf{b})})$, the profile function, whose square module is used for the elastic cross section, is a Gaussian:

$$\Gamma(s,b) = \frac{\sigma_{tot}}{4\pi\, B(s)}\, e^{-b^2/2B(s)} \tag{1.20}$$

with standard deviation $R(s) \sim \sqrt{2\, B(s)}$, interpreted as the mean interaction range or hadron radius. According to this picture of the hadron interaction in the impact parameter space, the higher the exponential slope of the elastic scattering, the bigger the radius. This hadronic shape well describes the elastic differential cross section at the lower energies. Analyses performed with data from ISR to SPPS show that increasing the energy s, B and σ_{tot} increase as well, therefore the proton becomes bigger and more opaque. A nice compilation of hadron opacity in the parameter space is given in [7] where the profile function is extracted also from TOTEM elastic scattering data at 7 TeV. The steadily rise of the TOTEM cross section and elastic slope, results in a consequent increase of the opacity at $b = 0$, with the opacity function starting to deviate from a pure gaussian shape. The results are summarised in picture 1.3.

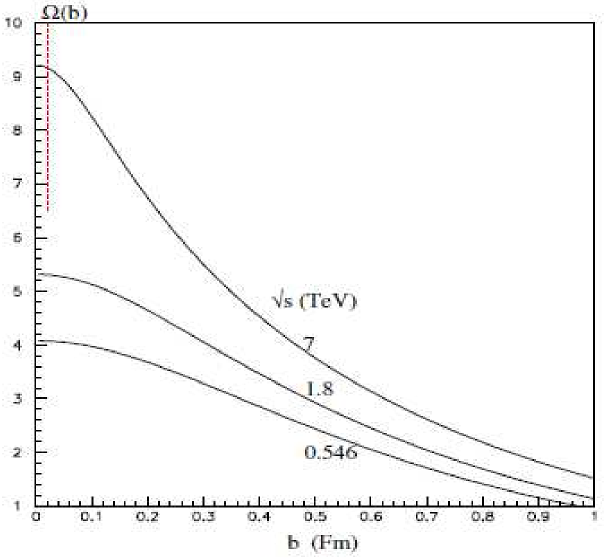

Figure 1.3: Opacity function extracted from elastic scattering data at $Sp\bar{p}S$, FNAL and LHC [7].

1.2.2 Regge theory

To predict the high energy scattering cross sections, Regge theory makes use of the concept of complex angular momentum combined with the requirement of analytical properties of the scattering amplitude. In non relativistic theory, the Schrödinger equation allows to determine the scattering amplitude of a particle with wavelength k impinging on a potential V. The bound states of the potential V appear as singularities of the partial-wave amplitude $a_l(k)$[2]. Regge theory analytically continues $a_l(k)$ to complex values of l. The poles of this emerging function $a(l,k)$ are called Regge poles.

Their location varies with the energy $E = k^2/2m$ and are described by a function $l(k)$ which passes through the physical values of l and E characterizing the scattering process: l is equal to a positive integer or zero when E is the energy of a bound state of the system (or the energy of a resonance of the two colliding particles). For successive integer values of l, the poles describe the energy of the resonant bound state created in the collision process. Another important property of the Regge poles is that they control the asymptotic behaviour of the scattering amplitude $f(k, cos\theta)$ when the cosine of the scattering angle $\cos\theta$ tends to the (unphysical value) infinity. The latter property is important since, in rel-

---

[2] In non relativistic quantum mechanics the scattering amplitude f can be expanded in a partial wave series:

$$f(k,\theta) = \sum_{l=0}^{\infty}(2l+1)a_l(k)P_l\cos\theta \tag{1.21}$$

where P_l are the Legendre polynomials.

ativistic physics, the infinite value of $\cos\theta$ for a two-particle scattering in the "s-channel" acquires a physical meaning in the scattering amplitude of the associated "crossed reaction"[3], that is supposed to happen at infinite values of the energy. Therefore the Regge poles can provide, once extended in the relativistic case, a theory for the high energy scattering of the particles. This is enough of a justification for considering complex values of the angular momentum [6]. In the following the main ideas which allowed to extend the Regge theory to the relativistic case are reported.

In the relativistic scattering the principle of crossing symmetry, consequence of the CPT symmetry, asserts that the same scattering amplitude $A(s,t)$ describes all three scattering $2 \to 2$ processes differing by a particle crossing, provided that suitable values of s, t and u are chosen in each case. In a crossing operation of a 2 body scattering, the ingoing particle transforms in an outgoing antiparticle, changing the momentum sign. The expression of t becomes therefore in the "t-channel" the center of mass energy.

In order to guarantee the crossing symmetry, the amplitude must be consider as a function of the complex variable (s,t). The amplitude will then have a physical meaning only for real and consistent values of (s,t). In the t-channel (where t is the center of mass squared and we suppose equal mass particles) if k is the particle momentum in the center of mass system, the scattering amplitude can be written as:

$$A(s,t) = \frac{8\pi}{k}\, t^{1/2} \sum_{0}^{\infty} (2l{+}1) f_l(t)\, P_l(cos\theta) \quad \text{where:} \;\; t = 4(k^2{+}m^2), \;\; s = -2k^2(1{-}cos\theta) \qquad (1.23)$$

The series converges in the complex $\cos\theta$ planes inside the ellipse with foci at ± 1, to a maximum value of $s = 4m^2$. To allow the amplitude to converge for large s (large $\cos\theta$, unphysical in the t-channel) Regge made use of the Sommerfield-Watson transform which requires an extention of the partial amplitude $f_l(t)$ from integer l to complex-value of l. In the Regge-Pole model (the simplest) the assumption is that $f(l,t)$ is regular for $\Re l > -1/2$

---

[3] More in general s,t,u channel reactions are defined by the processes:

$1 + 2 \to 3 + 4$ s-channel

$1 + \bar{3} \to \bar{2} + 4$ t-channel

$1 + \bar{4} \to \bar{2} + 3$ u-channel

Where the bar indicates the antiparticle. In the s-channel, supposing for simplicity equal masses, the scattering angle is given by:

$$\cos\theta = 1 + \frac{2t}{s - 4m^2} \qquad (1.22)$$

While this expression is always smaller than 1 in the s-channel, in the t-channel where t becomes the center of mass energy it can assume values greater than one.

except for complex poles. After the transformation, it was shown that the form of the amplitude for fixed t and large s is of the form:

$$A(s,t) \sim \sum_n \frac{\beta_n(-1)^{\alpha_n}}{sin(\pi\alpha_n(t))}\left(\frac{s}{s_0}\right)^{\alpha_n(t)} \tag{1.24}$$

Where the sum is over the simple poles $\alpha_n(t)$. Each pole contributes to the scattering amplitude a term which asymptotically behaves like:

$$A(s,t) \to s^{\alpha(t)} \quad \text{t fixed, s} \to \infty \tag{1.25}$$

Therefore the leading singularity (the one with higher real part) in the t-channel determines the asymptotic behaviour of the reaction in the s-channel. The poles of the scattering amplitude in the t-channel can be found looking at the resonances of the crossed reaction where the total cross section (and therefore the imaginary part of the elastic amplitude) rapidly grows. Therefore by the interpolation of the resonances in the crossed channels it was believed to extract the function $\alpha(t)$ where real values of α indicate the angular momentum of the resonances and t its mass square.

It was experimentally found that all the resonances with the same internal quantum numbers contributing in the scattering processes have spin differing by two. These resonances lie in an almost linear relation over the mass-spin plane. This line is called Regge trajectory. This relation was also used to find precedently unknown particles. To make an example of how the Regge theory can be used, let's suppose to study the $\pi^- \, p \to \pi^0 \, n$ reaction in the s-channel: the crossed t-channel reaction $p\,\bar{n} \to \pi^+\pi^0$ must be studied. It is known that the elastic cross section $\pi^+\pi^0$ has the ρ^+ resonances. Therefore the $\alpha_\rho(t)$ trajectory, reported in fig. 1.4, will contribute to the asymptotic behaviour of the $\pi^- \, p \to \pi^0 \, n$ reaction:

$$\frac{d\sigma(\pi^- p \to \pi^0 n)}{dt} \equiv \frac{1}{16\pi\, s^2}|A(s,t)|^2 \sim \, |b(t)|^2 \, s^{2\alpha(t)-2} \tag{1.26}$$

where the relation between the scattering amplitude and the differential cross section has been explicitly shown, and α is the allowed trajectory. Experimentally the measured Regge trajectories have been found to have an intercept smaller than one. Therefore being the trajectory of the form $\alpha(t) = \alpha_0 + \alpha'(t)$ two important predictions of the Regge simple pole model can be obtained (see also the optical theorem):

$$\sigma_{tot} \sim \, s^{\alpha(0)-1}, \qquad \frac{d\sigma}{dt} \sim H(t)s^{2\alpha(0)-2}e^{(2\alpha' log\, s)t} \tag{1.27}$$

where $H(t)$ is a slowly varying function of t.

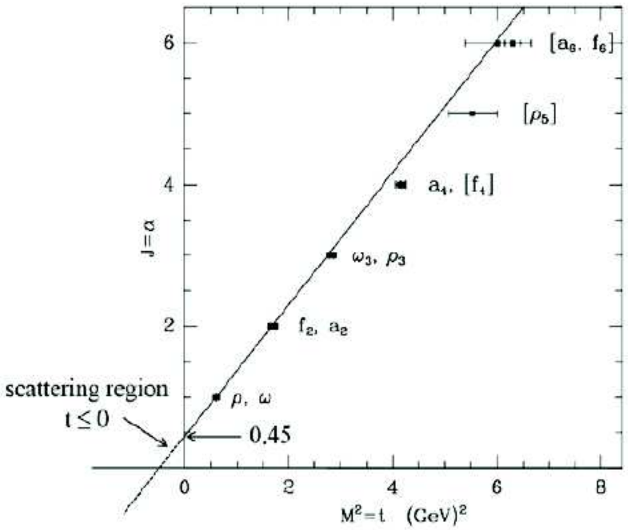

Figure 1.4: Chew-Frautschi plot for the Regge trajectory containing the ρ meson (mass = 770 MeV), practically linear up to very large masses.

Equation 1.27 shows that Regge trajectory exchange predicts an exponential fall-off of the elastic t-distribution, with a slope parameter B which increases logarithmically with the energy. In the 60s these simple predictions were found to be approximately verified in all hadron-hadron scatterings, making Regge theory very popular. Moreover the first relation of eq. 1.27 was also compatible with the fact that, at those energies, cross sections were decreasing or starting to be flat. With the simple Regge pole model it is not possible to predict the rising of the cross section. For this purpose, a new trajectory was introduced with the quantum number of the vacuum: the Pomeron. This should allow to describe the enhancement of the cross section with the energy. For a cross section which rises with the energy, the intercept should be > 1 and the apparent violation of the Froissart bound is not considered harmless if the Pomeron trajectory is taken as an effective quantity, which is allowed to slightly change with the energy. The exact value was proposed by Donnachie and Landshoff [8] who fitted the available data on all hadron-proton cross section at $\sqrt{s} > 6$ GeV with the simple expression:

$$\sigma_{tot} = X s^{\alpha_P(0)-1} + Y s^{\alpha_R(0)-1} \tag{1.28}$$

where the first term corresponds to Pomeron exchange and the second to normal Regge exchange. This model was able to well fit the proton-hadron scattering data with a Pomeron intercept of $\alpha_p(0) = 1.0808$. It is worthy to notice that the TOTEM measurements are important also for the testing of this simple model: fig. 1.5 indeed shows the dependence of

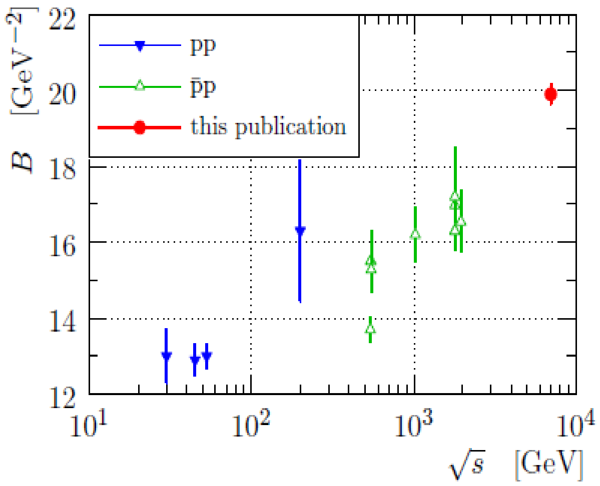

Figure 1.5: The forward slope B for pp and $p\bar{p}$ elastic scattering as a function of the center of mass energy of the collision. The TOTEM measurement shows a fast rise of B at the LHC energies.

the the exponential slope of the elastic scattering B from the energy, including the TOTEM point. These measurements can be used to test wether the rising of B is compatible with the $ln(s)$ behaviour, as predicted by the Regge model.

1.3 Inelastic collisions

1.3.1 Description of the hard hadron interactions

Inelastic hadron-hadron collisions can be described in terms of pQCD only when the process is characterised by a large 4-momentum transfer Q, exchanged between two partons of different hadrons. The fundamental physical concept that makes the theoretical description of these phenomena possible is “factorisation”, namely, the ability to separate independent phases of the overall collision having different time scales. In particular, factorisation allows to decouple the complexity of the internal hadron dynamics and of the final-state hadron formation from the perturbative hard interaction among the partonic constituents [9]. The global state of the proton, is determined by a continous gluons exchange between quarks characterized by interactions that have a time scale of the order of $1/m_p$. When seen in the laboratory frame where the proton is moving with the energy $\sqrt{s}/2$, this time is furthermore Lorentz-dilated by the factor $\gamma = \sqrt{s}/2m_p$. If the quark interacts with a probe of virtuality $Q \gg m_p$, the time for this interaction is enough short ($\sim 1/Q$) that the quark can be considered isolated from the rest of the proton during this time interval. After the hard process, the partons liberated during the evolution prior to the collision and the partons created by the hard collision also emit radiation. The radiation process, governed by perturbative QCD, continues until a low-virtuality scale is reached and hadronisation can start. Hadronisation is assumed to be independent of the initial hard process (universality of hadronisation). The above ideas are embodied in the following factorisation formula:

$$\frac{d\sigma}{dX} = \sum_{j,k} \int_{\hat{X}} f_j(x_1, Q) f_k(x_2, Q) \frac{d\hat{\sigma}_{jk}(Q)}{d\hat{X}} F(\hat{X} \rightarrow X; Q) \tag{1.29}$$

where X is some hadronic observable, j and k range over the parton types inside the colliding hadrons, the function $f_j(x; Q)$ (known as the parton distribution function, PDF) parametrises the number-density of partons of type j with the momentum fraction x in a proton probed at a scale Q. $\hat{X}$ is a parton-level kinematical variable, $\hat{\sigma}_{jk}$ is the parton-level cross section, differential in the variable $\hat{X}$; $F(\hat{X} \rightarrow X; Q)$ is a transition function, taking into account the probability that the partonic state defining $\hat{X}$ gives rise to the hadronic observable X after hadronisation. It turns out that the distinction between gluons that are reabsorbed in the hadron evolution and those that are not depends on the scale Q of the hard probe. As a result the PDF, as written in eq. 1.29, depends on Q. As an example, a gluon emitted at a scale m has a lifetime short enough to be reabsorbed before a collision with a probe of virtuality $Q < m$, but too long for a probe of a virtuality $Q > m$. This effect therefore modifies the effective PDF seen by the probe at a certain x, and the effect of the modification would depend from the Q^2 of the probe. This Q^2-dependence are determined in the Dokshitzer-Gribov-Lipatov-Altarelli-Parisi (DGLAP) equation which allows to include these effects that are intrinsically non perturbative on the PDF definition. It is important to remind that the DGLAP evolution of parton densities, furthermore, requires modifications when x is so small that log(1/x) is of the order of unity, or when the gluon density becomes so large that gluon recombination becomes possible. In section 1.3.2, more details on the high gluon density regime is reported.

1.3.2 Saturation of gluon densities and the Color Glass Condensate

When a nucleon is boosted to a higher energy, its internal time scales are dilated: the interactions among the constituents of the nucleon now occur over much larger time scales, and therefore the probe sees only a collection of free constituents. The life-time of the quantum fluctuations is also time dilated, and thus the number of gluons contributing to the interaction increases with the collision energy. Simultaneously, the fluctuations that were already important at the lower energy are now evolving so slowly that they can be considered static for the probe [10]. Note also that for a fixed virtuality Q^2 of the exchanged boson, the higher the hadron momentum P, the lower the value of $x = Q^2/2P \cdot Q$, probed during the interaction.

However the growth of the number of gluons with the energy cannot continue indefinitely. Indeed, it would imply that nucleon-nucleon cross sections grow faster than what is allowed by Froissart unitarity bound. The BFKL evolution equation[4] for the PDF indeed predicts an exponential growth of the gluon density at low x. The distribution of the number of gluons per unit of rapidity in the hadron wave function, $\sim xG(x, Q^2)$, has been measured by HERA [12] and confirms the fast growing at low x (see fig. 1.6). However, this physics boundary is not violated if one takes into account that gluons can recombine when their occupation number is large. This process is known as "gluon saturation" [13] and it is not taken into account in the standard BFKL equation. To quantify when this new phenomenon occurs, the number of gluons per unit of transverse area, $\rho \sim xG(x, Q^2)/\pi R^2$ and the cross section for recombination, $\sigma \sim \alpha_s/Q^2$ should be evaluated. Saturation is defined by the condition $1 \sim \rho\sigma$, or equivalently $Q^2 \sim Q_s^2(x)$, where $Q_s(x) = \alpha_s xG(x, Q_s^2)/(\pi R^2)$ is known as the saturation momentum. The equation $Q^2 = Q_s^2(x)$ delineates the border of the saturation domain, indicated in figure 1.7. Phenomenologically, Q_s^2 varies like $A^{1/3}x^{-0.3}$ with the nucleus atomic number A and the momentum fraction x. When the probe has

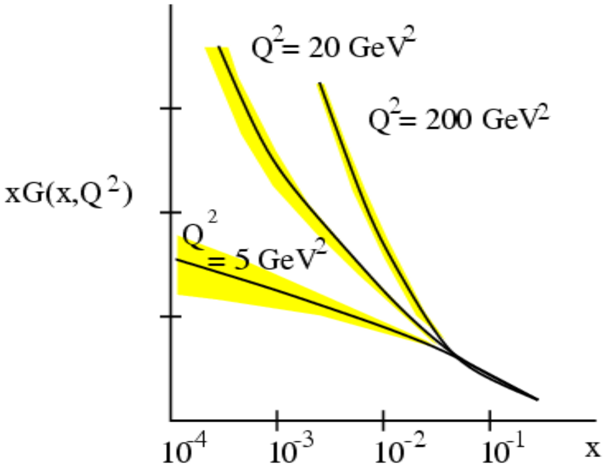

Figure 1.6: The ZEUS data for the gluon structure function. The different value of Q^2 correspond to interactions with different virtuality of the photon.

---

[4] As reported in the previous section, the DGLAP equation allows to predict the evolution of the PDF as the Q^2 of the probe changes. This is technically due to the sum of terms in the perturbative series which are power of $ln\, Q^2$. These logarithms are called collinear since they are picked up from the region of small angles between parton momenta during a splitting. There are logarithms of another kind, which are called soft ones, arising at integration over ratios of parton energies during the branching processes. These logarithms are present both in parton distributions and in partonic cross sections and at small values of x appear to be even more important than the collinear ones [11]. The parton evolution in this regime is resolved with the BFKL equation.

much finer spatial resolution, $Q^2 >> Q_s^2$, the physics is described by the well-studied linear regime of QCD, dominated by gluon splitting. But as Q^2 decreases below Q_s^2 one enters the novel nonlinear regime of saturated gluonic matter. The evolution of the gluon density according to the probe Q^2 and the gluon x is resumed in fig. 1.7.

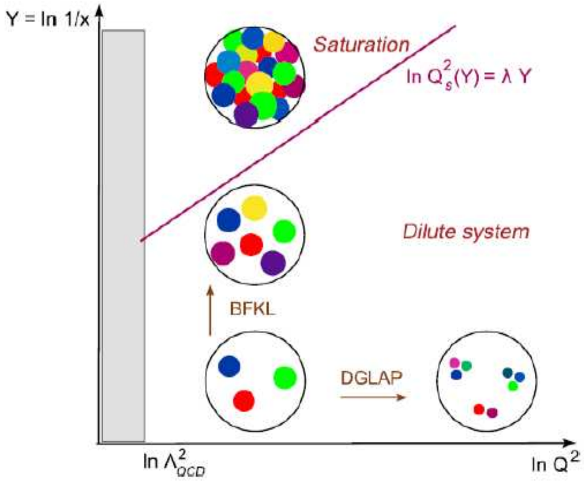

Figure 1.7: Evolution of the partonic density of a nucleus as a function of (Q^2, x). The red line delineates the border of the saturation domain.

To describe the saturation region where both the linear BFKL and DGLAP equations cannot be used for the gluon evolution, an effective theory, the Color Glass Condensate (CGC) has been developed. In the CGC description, the fast partons (large x) are described as static colour sources characterized by a certain density in the transverse plane that act as external sources. Conversely, the slow partons (low x), dominated by gluons, are described by a classical colour field [14]. The word “color glass condensate” has been coined due to the “color” of the gluons which the theory aims to describe; the term “condensate” remind the condensed state of the gluons because of their high density; the word “glass” depicts the behaviour of the gluon fields: the time dilation make the gluons static on a short time scale while on a longer time scale they are not. This resembles the property of the glass that can be see as a solid on short time scale while it is a liquid on longer time scale. It is important to remind that within the formalism of the CGC the non-perturbative region of QCD where high gluon densities are created can be treated, allowing to perform some prediction for the soft inelastic events [15]. One of them is reported in sec. 1.3.5.

1.3.3 Soft inelastic interactions

A large amount of pp interactions at LHC are soft, i.e. there is no evidence in the properties of the measured particles of a high-p_t subnuclear interaction. However only the processes where large four momentum transfer between partons occurs can be described with the QCD theory, where the perturbation theory can be applied. The description of the scattering evolution from the parton level to the hadron level contains non-perturbative aspects that have to be modeled, as well as the "underlying event" defined as the part of the event which excludes the particles related to the hard scattering. This soft physics is extremely important not only because a complete theory for its description is still missing but also because it has to be well modeled as it constitutes the background that experiments have during the analysis of the high-p_t processes. Phenomenological models allowing to describe the soft interaction are encoded in the MC generators. Since the Pythia 6 and Pythia 8 MCs are the most extensively used in this thesis, hereafter a brief resume of the description of the soft inelastic interaction adopted by these MCs, is reported. The total cross section (the value of the latter is predicted according to the Donnachie Landshoff model [8], see eq. 1.28) is expressed in terms of the main soft cross sections:

$$\sigma_{tot} = \sigma_{el} + \sigma_{sd} + \sigma_{dd} + \sigma_{nd} \tag{1.30}$$

A schematic view of the elastic (el), single-diffractive (sd), double diffractive (dd) and non diffractive (nd) events in the $\eta - \phi$ plane is reported in fig. 1.8. The inelastic cross sections predicted by Pythia 8 at $\sqrt{s}$ = 7 TeV are 48.45 mb, 2x6.84 mb and 9.26 mb respectively for the ND, SD and DD events. The multiplicities and the pseudorapidity density of these inelastic event classes are sensibly different. Fig 1.9 shows the Pythia 8.104 dN$_{ch}$/dη for the different inelastic events. The diffractive cross-sections, as a function of the Mandelstam variables s, t are given by:

$$\begin{aligned}\frac{d\sigma_{sd}(s)}{dt\,dM^2} &= \frac{g_{3p}}{16\pi}\beta_{Ap}^2\beta_{Bp}\frac{1}{M^2}e^{tb_{sd}}F_{sd}\\ \frac{d\sigma_{dd}(s)}{dt\,dM_1^2\,dM_2^2} &= 2\frac{g_{3p}^2}{16\pi}\beta_{Ap}\beta_{Bp}\frac{1}{M_1^2}\frac{1}{M_2^2}e^{tb_{dd}}F_{dd}\end{aligned} \tag{1.31}$$

where M (or M_1 and M_2) represents the mass of the diffractive systems. The coupling constant β_{Ap} and β_{Bp} are chosen in order to be consistent with the total cross section model of Donnachie and Landshoff. The triple pomeron coupling is taken as g_{3p} = 0.318 mb$^{1/2}$. F_{sd} and F_{dd} are fudge factors introduced in order to obtain "sensible" behaviour of the Regge models reported above in the full phase space. The exponential slopes b_{sd} and b_{dd} are supposed to have a logarithmic dependence on the center of mass energy.

The Pythia description of the high-energy collision between hadrons can be summarised in the following steps [17, 18]:

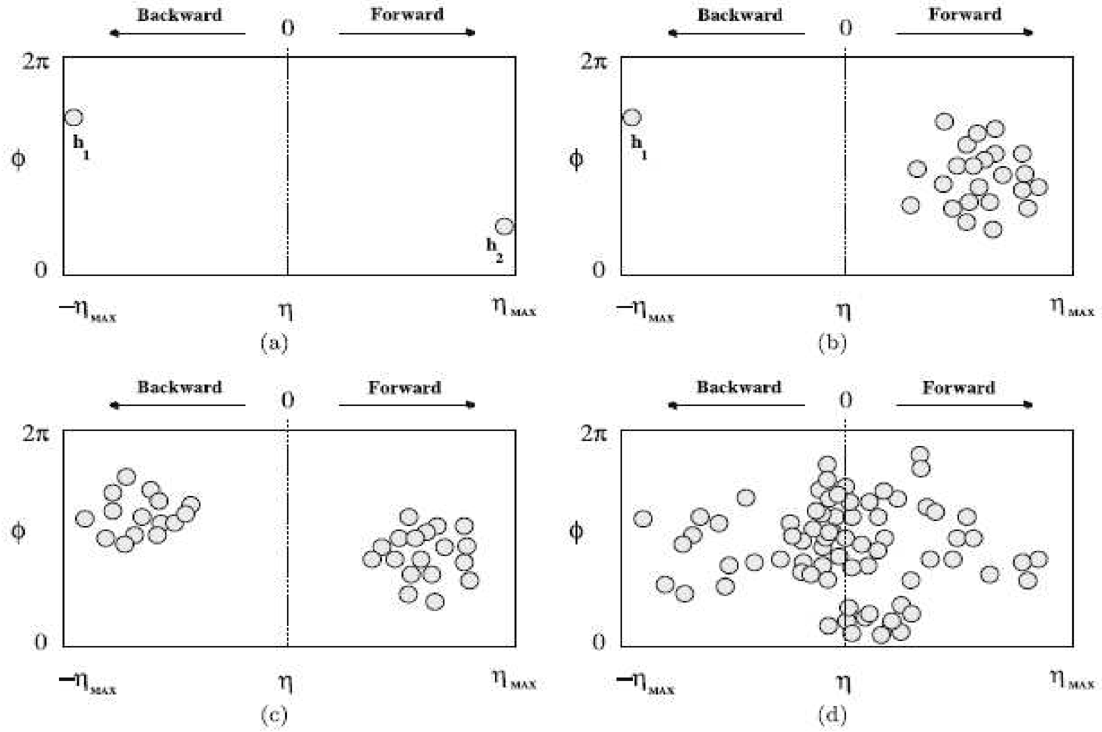

Figure 1.8: Schematic view of (a) elastic, (b) single-diffractive, (c) double-diffractive and (d) non-diffractive h1+h2→X interactions in the $\eta - \phi$ plane [16].

- The two approaching hadrons are characterised by the corrensponding parton distributions.
- One parton shower initiator from each beam starts off a sequence of branching such as q→qg, which build up an initial-state shower (ISR).
- One incoming parton from each of the two showers enters the hard process and a number of outgoing partons are produced, usually two. The scattering is resolved by evaluating the matrix element, which are usually at the leading order. It is the nature of this process that determines the main characteristics of the event.
- Also the outgoing partons may branch, to build up final-state showers (FSR).
- Multiple parton interaction occurs between the parton not involved in the main hard scattering.
- When a shower initiator is taken out of a beam particle, a beam remnant is left behind. These remnants have a net colour charge which will be reconnected to the rest of the

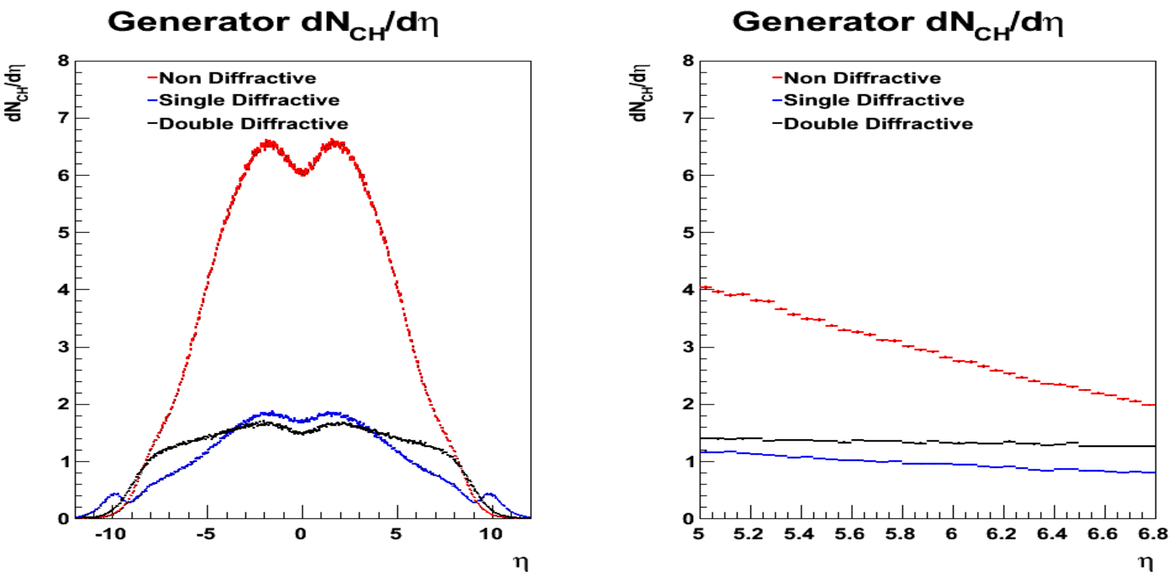

Figure 1.9: Pythia 8.108 $dN_{ch}/d\eta$ for ND (red), SD (blue) and DD (black) interactions. On the right a detail in the pseudorapidity range $5 < \eta < 6.8$ is given.

final state.

- An hadronization model is implemented which evolves the coloured partons to colour neutral hadrons.
- Many of the produced hadrons are unstable and decay further by using the decay-table implemented in the generator.

Soft events are handled by the multiparton-interactions machinery. In this case, no hard process at all is defined during the event generation process but the first, i.e. hardest, subprocess of the multiparton-interactions is selected. The evolution is then described as in the case where a hard scattering is involved.

A schematic picture of the MC event simulation is reported in fig. 1.10 [19].

The traditional approach to handle perturbative corrections (the matrix-element method i. e. to calculate Feynman diagrams order by order taking in account exact kinematics, the full interference and the helicity structure) becomes increasingly difficult in higher orders with the limitation of becoming less relevant with the increase of the available energy that increases the phase space available for gluon emission [18]. So it is replaced by the "parton shower method", where the full matrix-element expressions is not used while approximations derived by simplifying the kinematics are taken into account. As an example, the parton showers constituting the ISR and the FSR have to be intended as an approximation

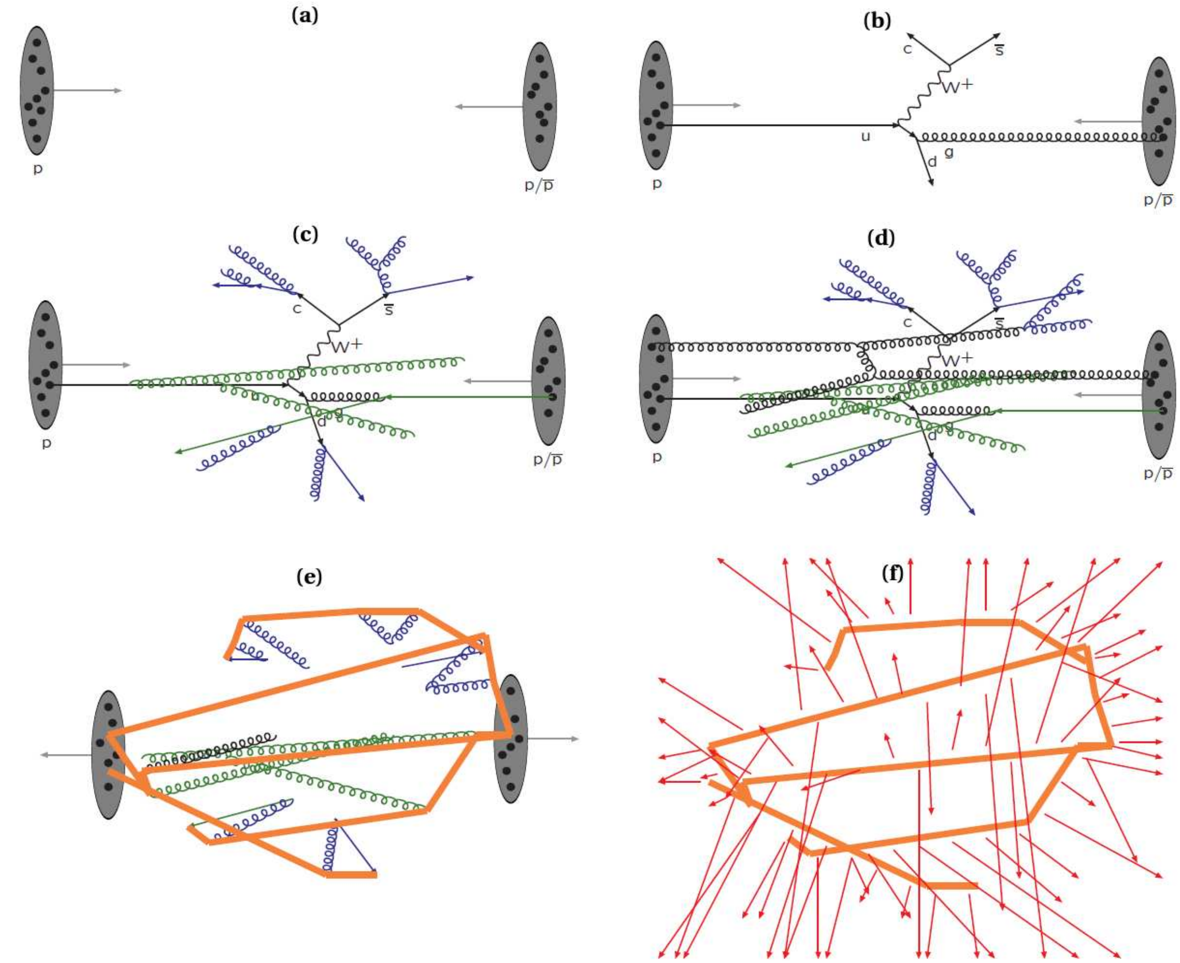

Figure 1.10: Schematic picture of the Pythia MC event [19] (see the text for more details). The partons of the approaching hadron (a) generates an hard interaction (b). The initial and final state radiation associated to this process is shown in fig. (c). Multiple scattering effects (d) are also taken into account, the final colour field (e) is then arranged into final state hadrons (f).

method for higher-order matrix elements. The cross section of the QCD bremsstrahlung which characterises the showers is however divergent for collinear and soft gluon emissions, therefore a strategy has to be introduced to correct for such divergences. In Pythia, the branching probabilities of parton a in partons b,c ($P_{a\to bc}(z)$) are given by DGLAP evolution equations [36, 37] and the parton showers stop their evolution below Q=1GeV.

Below $p_{tmin} = 2$ GeV also the $2 \to 2$ parton scattering cross section $\sigma(p_{tmin})$ exceeds the total inelastic cross section. This scattering is reinterpreted as a parton multiple scattering process where the number of parton-parton interaction N_{pp} is given by:

$$N_{pp} = \sigma(p_{tmin})/\sigma_{nd} \tag{1.32}$$

In particular, in the "complex model" adopted by Pythia for the multiple scattering simulation, the average number of interactions is Poisson distributed and depend on the simulated impact parameter b of the two colliding protons. The proton matter is supposed to be distributed with a density $\rho(r)$ which is the sum of two Gaussians:

$$\rho(r) \propto \frac{1-\beta}{a_1^3} \exp\{-\frac{r^2}{a_1^2}\} + \frac{\beta}{a_2^3} \exp\{-\frac{r^2}{a_1^2}\} \tag{1.33}$$

For a collision with impact parameter b, the time-integrated overlap $\mathcal{O}(b)$ between the matter distributions of the colliding hadrons is given by:

$$\mathcal{O}(b) \propto \int dt \int d^3x \rho(x,y,z)\rho(x+b,y,z+t) \tag{1.34}$$

And the average number of collisions at impact parameter b, n_b, is proportional to $\mathcal{O}(b)$: $\langle n_b \rangle \propto k\mathcal{O}(b)$. Normalising to events with at least one interaction per crossing, the average number of interactions is therefore:

$$\langle n_b \rangle = \frac{k\mathcal{O}(b)}{1 - exp(-k\mathcal{O}(b))} \tag{1.35}$$

where k is fixed requiring that the average number of interactions integrated over b is equal to $\sigma(p_{tmin})/\sigma_{nd}$ (see eq. 1.32).

To regularise the divergent partonic cross sections a cut-off parameter is introduced, defined as: $p_{tmin}(s) = 1.9$ GeV$(\frac{s}{1TeV})^{0.08}$ where $\sqrt{s}$ is the center of mass energy of the collision. Since the matrix element diverges as $1/\mathrm{p}_t^4$, it is multiplied by the factor $\mathrm{p}_t^4/(\mathrm{p}_t^2+\mathrm{p}_{tmin}^2)$, and the same substitution $\mathrm{p}_t^2 \rightarrow \mathrm{p}_t^2+\mathrm{p}_{tmin}^2$ is applied in the α_s term.

For the hadronisation process Pythia uses the Lund model [20], based on the string fragmentation model. The interaction between partons is represented by a colur field string which is stretched as partons move apart. If a critical tension in the string is reached, it breaks and new particles are produced at the ends of the two new strings. According to the invariant mass of the produced particles, the process can be reiterated until only colourless particles are left.

1.3.4 Models for particle pseudorapidity density and multiplicity

Fermi Model

One of the first work on the analysis of the hadronic collisions is due to Fermi [21]. His approach, based only on pure statistical and thermodynamical concepts, allowed to predict the multiplicity dependence on the center of mass energy. Fermi assumed that when two relativistic nucleons collide, the energy available in their center-of-mass frame is released in a very small volume V. Due to the strong field surrounding the two nuclei it is expected that this energy is rapidly distributed among the degrees of freedom present in this volume, according to statistical laws. Because of the Lorentz contraction of the nuclei, the volume is taken energy dependent:

$$V = V_0 \, 2Mc^2/W \qquad , \qquad V_0 = 4\pi(\hbar/\mu c) \tag{1.36}$$

where W is the center of mass energy and μ is the pion mass. Subsequently, such a dense system (fireball) decays into one of the many accessible multiparticle states. The decay probability is calculated in the framework of the standard statistical physics. For highly relativistic final state particles, the energy density of the system (ϵ) has the same form predicted by the Stefan law, $\epsilon \sim W/V \; \sim kT^4$. Apart from the different statistical weights, the density of pions n_p and nucleons is expected to depend on the temperature (T) as $\sim kT^3$, like for a gas of photons. From the energy density the relation $T \sim W^{1/2}$ is obtained, therefore the number of produced particle N_p is expected to follow the law: $N_p = n_p V \sim W^{1/2}$. Experimentally it is found that the particle production actually grows slower than this power law. Moreover assuming a decay of the system from a rest source at equilibrium, the isotropic emission would reflect in a universal shape of the $dN/d\eta$ distribution: $dN/d\eta \sim 1/cosh^2(\eta)$. When compared with the data, this model showed disagreement in reproducing the relative abundance of K over π and furthermore the model predicted an isotropic momentum distribution which did not agree with the observed spectra [22]. This was because the particles were assumed to be emitted directly from the hot and dense matter formed in the high-energy nuclear collision, which was supposed to be at equilibrium and at rest. Even if these assumptions are too strict, this model is valuable since it introduced the study of the relativistic collisions by means of thermodynamical and statistical physics concepts.

Landau model

Some of the problems shown by the Fermi model were solved by the hydrodynamical description of the high energy nucleus-nucleus collisions introduced by Landau [23, 24].

According to his ”Hydrodynamical Model“, the description of high-energy nuclear collisions proceeds in three main steps. At the beginning, two Lorentz contracted (in the c.m. frame) nuclei collide and it is assumed that, as for the Fermi model, a hot and dense matter is formed in local thermal equilibrium.

Then, it follows a hydrodynamical expansion, described by the relativistic equation of the fluid motion, obtained from the conservation of the stress-energy tensor and of specific quantum numbers (as the baryon number):

$$\partial_\nu T^{\mu,\nu} = 0 \quad ; \quad \partial_\mu(n_i u^\mu) = 0 \tag{1.37}$$

where $T^{\mu\nu} = (\epsilon + p)u^\mu u^\nu - p g^{\mu\nu}$ is the energy-momentum tensor, n_i, ϵ, p are, respectively, the density of the conserved quantum number, the energy density and the pressure, calculated on the fluid element, while u is the four-velocity of the fluid. Moreover the equations of state $p = p(\epsilon)$, which depend on the nature of the hot matter produced, have to be specified[5]. A larger gradient pressure is expected along the beam direction with respect to the transverse one. As the expansion proceedes, the fluid becomes cooler and cooler and more rarefied, occurring finally in the decoupling of the constituent particles which are not anymore interacting. At the freeze out temperature (T$\sim m_\pi$), the pions are expected to follow an ideal Bose distribution in the comoving frame. The solution of the equations leads to the prediction of a Gaussian particle rapidity distribution:

$$\frac{dN}{dy} \sim \frac{1}{\sqrt{2\pi\, L}}\, e^{-\frac{1}{2}\frac{y^2}{L}} \qquad \text{with} \qquad L = ln\frac{\sqrt{s}}{m_p} \tag{1.38}$$

The width of the distribution grows logarithmically with the energy. Moreover, this model already predicts the interesting behaviour of the “Extended Longitudinal Scaling”, addressed in more details in sec. 1.3.5.

Feynman model

According to Feynman [25], the interaction field created during a high energy hadron interaction should be narrowly distributed along the beam axis (z-axis), so that the corresponding particle p_z-distribution is uniform. For low values of $x = p_z/W$ (the variable $x = p_z/W$ is called Feynman-x where W is the center of mass energy) and a fixed p_T he argued that the particles should be distributed as $dN/dp_z \sim 1/E$. The probability to produce

---

[5] In the first works, the same equation as the one for the black body radiation was used.

a particle of "kind i" with a given p_T and p_z is therefore given by:

$$P_i(p_T, p_z) = f_i(p_t, x)\frac{dp_z}{E}\, d^2\, p_T \qquad (1.39)$$

f_i describes the particles distribution. The Feynman hypothesis [26] is that f_i becomes independent of W at high energies. This assumption is known as Feynman scaling and f_i is called Feynman function. By also taking into account the experimental information that f_i can be factorised $f_i(p_t, x) = f_i(x)g_i(p_t)$, he deduced an analytical expression for the average number of particles produced in the collision ($\langle N \rangle$):

$$\langle N \rangle = \int f_i(p_t, x)\frac{dp_z}{E}\, d^2\, p_T = 2B[ln(1 + \sqrt{1 + (\frac{m_T}{W})^2}) + ln\frac{m_T}{W}] \qquad (1.40)$$

where $m_T = \sqrt{m^2 + p_T^2}$ and B is the value expected to be reached at x=0. Therefore in the Feynman model the average total multiplicity scales with $\ln W$. Moreover since it holds[6]:

$$\frac{E}{p_T}\frac{d^2N}{dp_T dp_z} = \frac{1}{p_T}\frac{dN}{dp_T} = \frac{1}{p_T}\frac{d^2N}{dp_T dy} \qquad (1.41)$$

it follows that dN/dy is constant. Therefore, as a consequence of eq. 1.40, the $dN/d\eta$ can only be wider by increasing the center of mass energy with its midrapidity value being constant. The prediction of a costant dN/dy at $y = 0$ was not supported already from the ISR data which showed an increase of the $dN/dy|_{y=0}$ with W. Moreover, the total charged particle multiplicity has been measured to have a faster increase with W with respect to the $\ln W$ dependence.

Charged particle multiplicity: KNO scaling and the Negative Binomial distribution

The probability $P(n)$ of producing n charged particles in the final state can be used to investigate the production mechanism of the particles. For a particle source without any correlations the multiplicity distribution follows a Poisson distribution. Data clearly reject this hypothesis, therefore the production of an additional final state particle is not independent from the configuration of the particles already produced. One of the main hystorical models, able to predict the charged particle distribution, was published in 1972 by Koba, Nielsen, and Olesen where the famous "KNO scaling" [27] of the multiplicity distribution has been formulated. According to this model, at very high energies ($s \to \infty$),

---

[6] Where in the first equality the hypothesis of the Feynman scaling is exploited and the last term is by definition equal to the first one.

the probability distributions $P_n(s)$ of producing n particles in a certain collision process should exhibit the scaling relation:

$$P_n(s) = \frac{1}{\langle n(s) \rangle} \psi(\frac{n}{\langle n(s) \rangle}) \tag{1.42}$$

where $\langle n(s) \rangle$ is the average charged particle multiplicity and ψ is an universal function. The scaling law was derived by using the Feynman scaling. The measurement at ISR seems to confirm this behaviour. However the UA5 collaboration found that already at 200 GeV this scaling is not valid anymore [28]. Experiments performed at higher energies showed instead that the multiplicity can be fitted with a negative binomial distribution $P^{NBD}_{p,k}$. This gives the probability to obtain in a sequence of $n+k$ Bernoulli trials, n failures before k successes, the order of the failures and successes being irrelevant. It is usually expressed as:

$$P^{NBD}_{p,k} = \binom{n+k-1}{n} (1-p)^n p^k \tag{1.43}$$

where p is the probability of a success. Being $p^{-1} = 1 + \langle n \rangle / k$, eq. 1.43 it is also rewritten as:

$$P^{NBD}_{p,k} = \binom{n+k-1}{n} \left(\frac{\langle n \rangle / k}{1 + \langle n \rangle / k} \right)^n \frac{1}{(1 + \langle n \rangle / k)^n} \tag{1.44}$$

The physical origin of a multiplicity distribution following a negative binomial shape has not been ultimately understood. One phenomenological explanation has been provided by the Clan model [29, 30, 31]. Here it is supposed that during a collision a set of N_c clusters, distributed according a Poissonian distribution, is created. These can emit additional particles due to decays and fragmentation. The probability to produce n_i charged particles in the clan i-th, $F(n_i)$, is supposed to be regulated by the relation:

$$\begin{aligned} F(0) &= 0 \\ (n_i + 1) F(n_i + 1) &= p n_i F(n_i) \end{aligned} \tag{1.45}$$

So clusters have at least one particle and the probability (p) to emit an additional particle is proportional to the number of existing particle (n_c). It can be shown that the probability to produce n particles (which is the sum of the contributions given by the different clans) is distributed according to a negative binomial distribution, with:

$$\begin{aligned} k &= \langle N_c \rangle F(1)/(p) \\ \langle n \rangle &= \langle N_c \rangle F(1)/(1-p) \end{aligned} \tag{1.46}$$

From the $Sp\bar{p}S$ collider it has been found [32] that the particle multiplicity distributions so far obtained are better fitted by a sum of two negative binomial distributions (two component fit). It is supposed that one describes the contribution of the soft processes, which follows the KNO scaling, while the other which contains the contribution of the hard and semihard interactions (like mini-jet production) violates the KNO.

1.3.5 Extended longitudinal scaling

The violation of the Feynman scaling in the central pseudorapidity region has been clearly shown by measurements from ISR, S$p\bar{p}$S, CDF and LHC. But the validity of the Feynman scaling in the fragmentation region (extended longitudinal scaling or hypothesis of limiting fragmentation) is still under discussion. This states that for very high energy collisions in the target system (target at rest) some of the outgoing particles approach to a limiting distribution which doesn't depend anymore on the collision center of mass energy. Because rapidities add under a Lorentz boost (see appendix .1), the rapidity distributions in the beam frame (y′) is obtained with a shift in the rapidity axis:

$$y' = y - y_b \tag{1.47}$$

where the beam rapidity is y_b =2ln$\sqrt{s}/m \sim 8.84$ at $\sqrt{s}$ =7 TeV. The fragmentation region is usually defined requiring particles with $|x| > 0.05$ [33]. This condition, for $y > 0$, implies:

$$\frac{1}{2} e^y \sim sinhy = \frac{P_L}{\sqrt{P_T^2 + m^2}} \geq \frac{0.05\sqrt{s}}{2\sqrt{P_T^2 + m^2}} \tag{1.48}$$

For a pion, assuming $\langle P_T \rangle$ ∼0.5 GeV/c (see sec. 1.3.6), it results $y > 4.36$ and therefore $y' > -4.48$. Fig. 1.11 shows a compilation of the inelastic dN_{ch}/dη measurement in the target frame, performed with the TOTEM T2 detector at 7 TeV and by other experiments at lower energies. For the UA5 measurements at 900, 546, 200, 53 GeV, the fragmentation region starts at $y' \sim -2.2$ [33] so the TOTEM measurement are slightly higher at this point.

The extended longitudinal scaling was found to be valid also in Pb-Pb collisions, as shown in fig. 1.12 [34], where the rapidity distributions are reported for two different

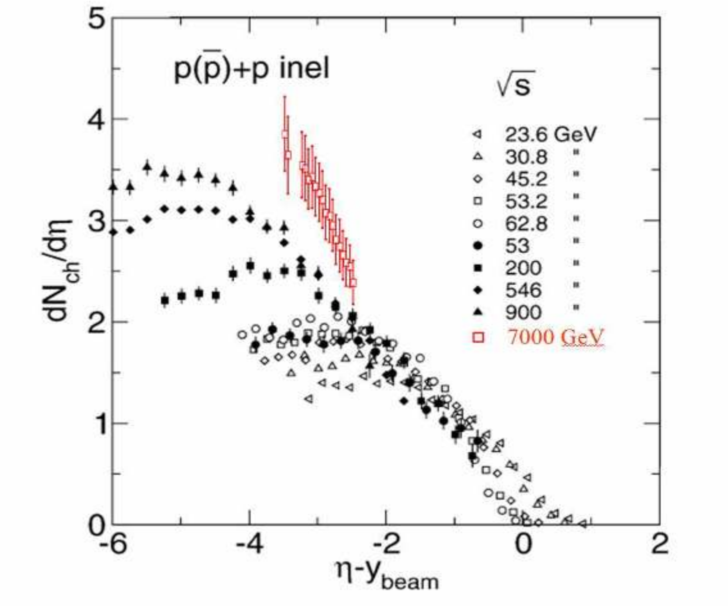

Figure 1.11: Distributions of the charged particles pseudorapidity density emitted in $p(\bar{p})$ or pp inelastic events as a function of the variable η - y$_{beam}$ [34]. The TOTEM result has been superimposed [1].

centrality-class of the collision.[7].

The extended longitudinal scaling has been already predicted by the Landau model: from eq. 1.38, the rapidity distributions in the beam frame is given by:

$$\frac{dN}{dy'} \sim \frac{1}{\sqrt{2\pi\, L}}\, e^{-\frac{y'^2}{2L} - y'} \tag{1.50}$$

which is compatible with the longitudinal scaling hypothesis since it only varies weakly with L ($L \sim \ln \frac{\sqrt{s}}{m_p}$) around $y' = 0$.

According to [35] the limiting distribution is due to the broken-up fragments of the target while the fragments of the projectile move with increasing velocity as $\sqrt{s}$ increase and do not contribute to the limiting fragmentation. The production process of the soft particles coming from the broken target is instead independent on the energy of the other particle. According to [36] this phenomenon indicates that some kind of saturation is taking place in high energy collisions. Indeed data show that for a fixed rapidity in the target frame it exists a maximum value of the projectile rapidity above which the increasing of

---

[7] The collision centrality is experimentally defined according to the global event multiplicity. In particular, the higher the multiplicity, the smaller the nucleon-nucleon impact parameter, the higher the centrality of the event. Let $P(n)$ denote the probability of obtaining a particle multiplicity equal to n. The centrality c is defined as the cumulant of $P(n)$:

$$c(N) = \sum_{n=N}^{\infty} P(n) \tag{1.49}$$

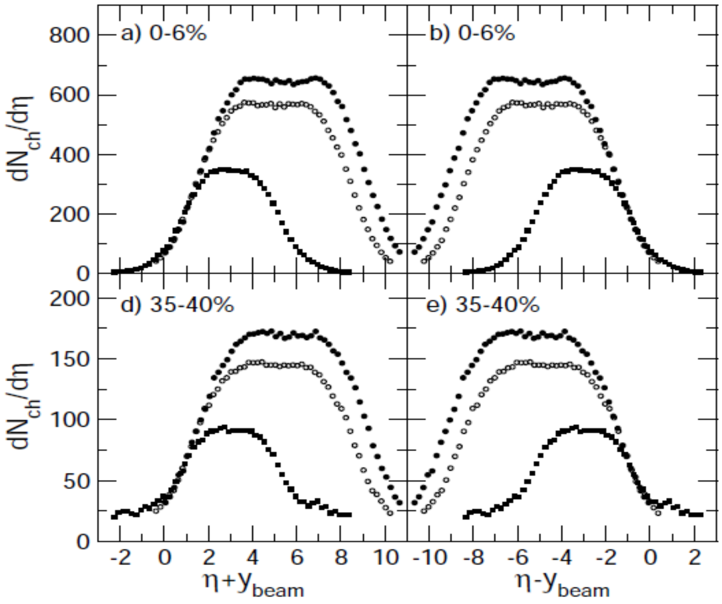

Figure 1.12: Pseudorapidity density distribution of charged particles measured at RHIC in Au+Au collisions at $\sqrt{s_{NN}}$ =200, 130, 19.6 GeV, for two different centrality ranges. The distributions are shown as a function of η+y_{beam} (left) or η-y_{beam} (right).

the energy of the projectile does not contribute to the production of additional particles, i.e. the “potential” that the target could produce more particles is saturated. It is interesting to note that the existence of a saturated “potential” of the slowest particle to produce forward hadrons, suggests to try the description of this phenomenon within the CGC model. This will be presented in the next section.

1.3.5.1 A modern interpretation of the limiting fragmentation

In [37] the limiting fragmentation phenomenon is explained in terms of the Color Glass Condensate model. Unlike the mid-rapidity region, the fragmentation region (very forward rapidities) in a high energy heavy ion collision, is expected to be quite similar to high energy proton nucleus collisions, up to shadowing nuclear corrections. This is because the Quark Gluon Plasma is expected to be formed only in the mid-rapidity region of an ION-ION collision and will not affect the particle production in the very forward rapidity region. Also, in the fragmentation region, one can treat the target nucleus as a dilute system of quarks and gluons while the projectile nucleus must be treated as a Color Glass Condensate due to its large number of gluons. The scattering between the gluon field of the projectile and the partons of the target can be carried out considering exactly also the contribution of low p_t particles. This leads to the following expression for the

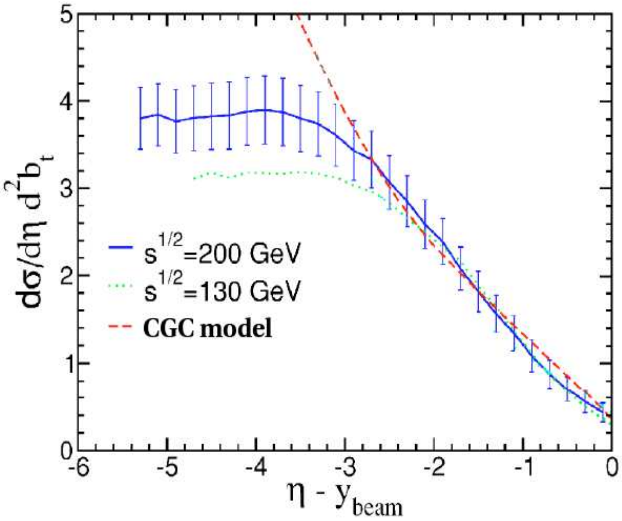

Figure 1.13: $dN_{ch}/d\eta$ distributions in the fragmentation region as obtained from the CGC model compared to data from RHIC.

nucleus-nucleus cross section:

$$\frac{d\sigma^{AA}}{d\eta\, d^2b_t} \sim [f_q^A(x) + xG^A(x)] \tag{1.51}$$

Where η is the parton rapidity, A is the atomic number of the nucleus, $x = e^{\eta_h - y_{beam}}$, f and G are the quark and gluon distributions of the target nucleus, in the frame where it is at rest.

Fig. 1.13 shows the comparison between the model and the most central data (with a centrality bin of 0-6%) from RHIC at $\sqrt{s} = 200$ and 130 GeV. The agreement with the data is quite good for the first three (two) units of rapidity. The physical picture behind the limiting fragmentation phenomenon in the Color Glass Condensate model is the following: in the rest frame of the target nucleus, the projectile nucleus is highly Lorentz contracted and due to its large number of gluons, looks black to the partons in the target nucleus which interact with the projectile nucleus with unit probability (the black disk limit). In other words, due to a large boost factor, the projectile nucleus has a saturation momentum scale which is larger than the momenta of most particles produced. In this kinematic region, the partons from the target nucleus (whose properties are independent on the collision energy since the process is described in the frame with the target at rest) interact with the projectile nucleus (Color Glass Condensate) with unit probability.

Even if this model is consistent with the longitudinal scaling, it cannot predict the overall normalisation and the Q^2 scale of the eq. 1.51 is fixed by requiring a good agreement of the model with the RHIC data at $\sqrt{s} = 20$ GeV. Moreover the model cannot be extended at midrapidities since high gluon density effects of the target would become important. Nevertheless it is intriguing to know that CGC theory can shed light on some aspects of the $dN_{ch}/d\eta$ distribution of the soft inelastic processes.

1.3.6 Experimental results on soft inelastic interactions

The properties of the charged particles produced in the hadronic interactions have been extensively studied in the past using cosmic rays, fixed targets and colliders data. Hereafter a brief summary of the main fixed target and collider experiments is reported. More details are reported in [38].

- FNAL (Fermi National Accelerator Laboratories): measurement of $dN_{ch}/d\eta$ and charged particle multiplicity in pp collisions with a hydrogen bubble chamber (full η acceptance). The equivalent center of mass energy achieved were $\sqrt{s}$: 13.8, 19.6, 23.8, 27.6 GeV [39, 40].

- CERN (ISR): measurement of the inelastic charged particle multiplicity at $\sqrt{s}$: 23.6, 30.8, 45.2, 53.2, 62.8 GeV, with streamer chambers detector at $|\eta| < 4$ [41].

- CERN (ISR): measurement of the NSD and inelastic pp charged particle multiplicity at $\sqrt{s}$: 30.4, 44.5, 52.6 and 62.2 GeV, with the "Split Field Magnet“ detector (almost full η acceptance) [42].

- CERN ($Sp\bar{p}S$): the UA1 collaboration measured the charged particle multiplicity and the pseudorapidity density at 200 < $\sqrt{s}$ < 900 GeV, for $|\eta| < 5.5$ [43].

- CERN ($Sp\bar{p}S$): the UA5 collaboration measured the charged particle multiplicity and pseudorapidity density at $\sqrt{s}$:53, 200, 546, 900 GeV. A 95% geometrical acceptance is reached at $|\eta|$ < 3 [44].

- CERN ($Sp\bar{p}S$): the P238 collaboration with the forward geometry micro-vertex silicon detector measured the $dN_{ch}/d\eta$ for NSD events at 630 GeV in the range $1 < |\eta| < 6$ [45].

- FNAL (TeVatron): the CDF collaboration measured the $dN_{ch}/d\eta$ at $\sqrt{s}$: 630, 1800 GeV in the range $|\eta|$ < 3.25 [46].

- FNAL (TeVatron): the E735 collaboration measured the NSD charged particle multiplicity at $\sqrt{s}$: 300, 546, 1000 and 1800 GeV, in the range $|\eta|$ < 3.25 [47].

- BNL (RHIC): the PHOBOS experiment measured the inelastic and NSD $p\bar{p}$ $dN_{ch}/d\eta$ at 200 and 410 GeV, with acceptance $\eta < 5.4$ [48].
- BNL (RHIC): the STAR experiment measured the NSD $p\bar{p}$ $dN_{ch}/d\eta$ at 200 GeV, mainly with a time projection chamber covering $\eta < 1.8$ [49].

Some of the most important experimental results are hereafter reported. Fig. 1.14 (left) shows the charged particle multiplicity distributions at energies lower than 1.8 TeV. On the right side the distribution is measured as a function of the KNO variables $N_{ch}/\langle N\rangle$, see sec. 1.3.4. The data showed that starting from the $Sp\bar{p}S$ measurements, the distributions seem to deviate from a unique and universal function. The distributions can always be fitted with two negative binomial distributions.

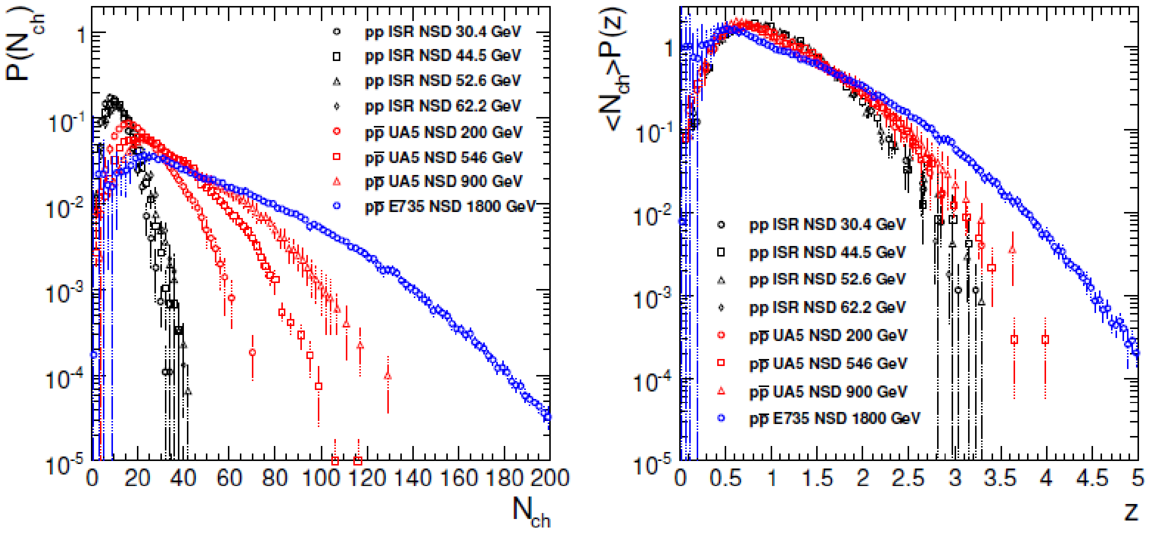

Figure 1.14: Charged particle multiplicity measurements from ISR, $Sp\bar{p}S$ and TeVatron data. On the right side the same distribution is reported as a function of the variable $z = N_{ch}/\langle N\rangle$. This figure is a courtesy of Dott. Yen-Jie Lee [38].

The measurement of the inelastic $dN_{ch}/d\eta$ from 23.6 to 900 GeV is reported in Fig. 1.15. The distributions clearly show an increase with the energy of the pseudorapidity density at mid rapidity and of the distribution width.

Fig. 1.16 (right) shows the value of $dN_{ch}/d\eta$ at $\eta = 0$ as a function of $\sqrt{s}$ for both the NSD measurements and the inelastic ones in the range 50 GeV $< \sqrt{s} <$ 7 TeV. A fit of second degree in $\ln(s)$ has been found to well describe the data.

The left part of fig. 1.16 shows the NSD average charged particle P_t as a function of $\sqrt{s}$, from 23.6 GeV obtained at ISR to the measurement of the CMS collaboration at 7 TeV. A fit

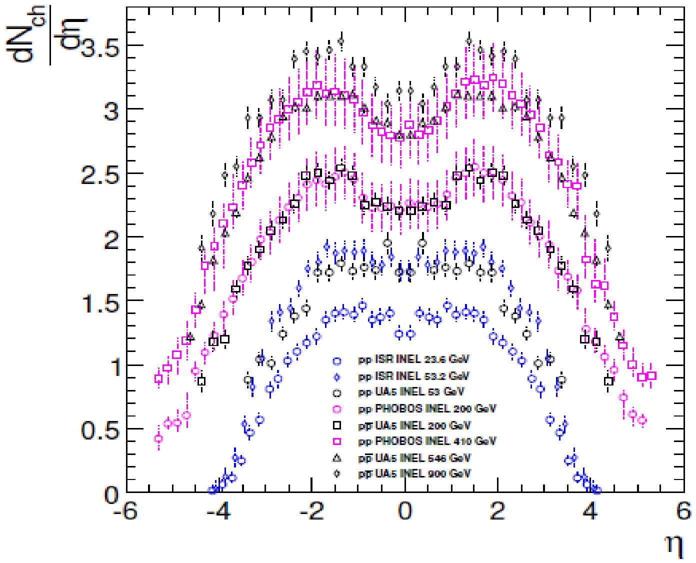

Figure 1.15: Charged particle pseudorapidity density measurement from ISR, $Sp\bar{p}S$ and RHIC data. This figure is a courtesy of Dott. Yen-Jie Lee [38].

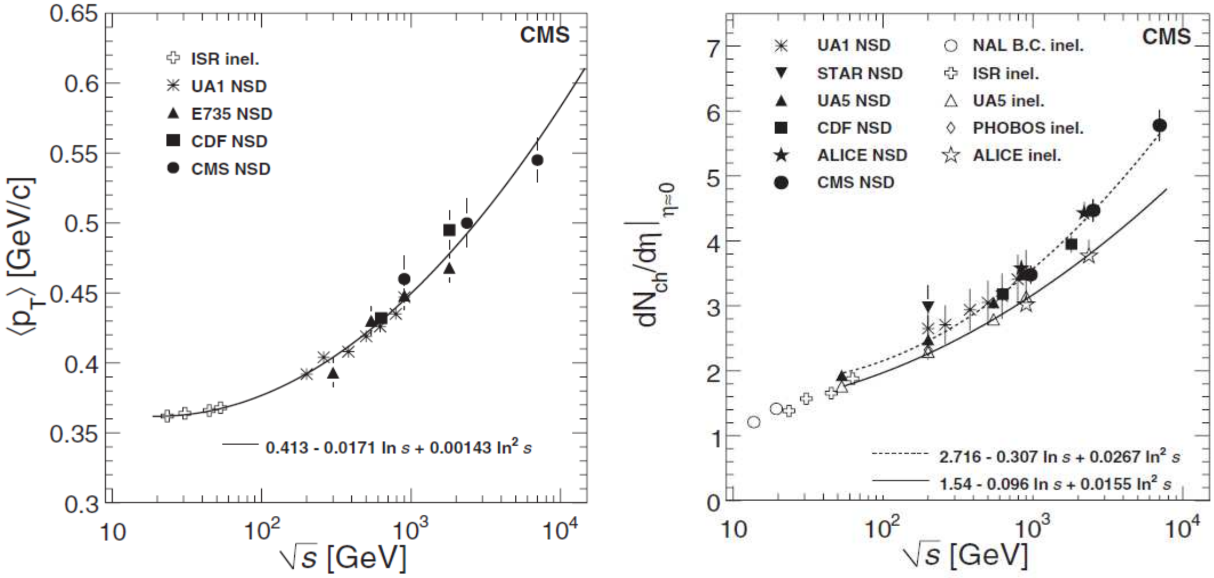

Figure 1.16: Left: average charged particle P_t as a function of $\sqrt{s}$ for NSD events. Right: charged particle $dN_{ch}/d\eta|_{\eta=0}$ as a function of $\sqrt{s}$ for NSD and inelastic pp (or $p\bar{p}$) events [50].

of second degree in ln(s) has been superimposed. It is also important to remind that the CMS measurements of the NSD event charged particle $\langle P_t \rangle$ showed no dependence on the selected pseudorapidity interval [50].

Chapter 2

The TOTEM experiment at the LHC

The TOTEM experiment [51, 52] is dedicated to the precise measurement of the total pp cross section, to the study of the elastic pp scattering and of the inelastic processes. TOTEM is located at the interaction point 5 of the LHC, shared with CMS, its detectors being designed to detect with high efficiency the very forward particles produced in pp collisions. The experimental apparatus is described in sec. 2.1. In particular the elastically scattered protons and the leading protons produced in the diffractive interactions are measured by the Roman Pot ("RP") stations (see sec. 2.1.1), composed of silicon detectors placed in special movable beam-pipe insertions located at about 147 m and 220 m from the interaction point. These edgeless silicon detectors can approach the beam down to few mm from the beam-axis, so that the proton can be detected down to few μrad, if proper machine optics are provied. Both sides of the interaction point are also equiped with Cathode Strip Chamber detectors ("the T1 telescope", see sec. 2.1.2) and with GEM-based detectors ("the T2 telescope", see sec. 2.1.3) allowing to detect the very forward charged particles produced in the inelastic interactions down to 3 mrad.

A description of the TOTEM Physics program is reported in sec. 2.2. The main Physics results achieved by the collaboration at the time of writing will be briefly summarised in sec. 2.3.

2.1 TOTEM Experimental Apparatus

The TOTEM (TOTal Cross Section, Elastic Scattering and Diffraction Dissociation Measurements at the LHC) experiment is composed of three different detectors located symmetrically on both sides of the interaction point (IP5). Fig. 2.1 shows the experimental apparatus and its location partly embedded in the forward region of the CMS experiment: one arm of the T1 and of the T2 detector, placed in front of the HF and CASTOR calorimeters of CMS respectively on the top picture; the RP stations at about 147 m and 220 m on the bottom one. Only the stations at 220 m have been used so far, although the stations at 147 m are equipped and fully operative. They are planned to be used for further analyses on elastic and diffractive scattering that will be carried out in the near future. The read-out of all TOTEM detectors is based on the “VFAT” front-end ASIC, which provides as output the digital information of the active channels and the trigger signal [53].

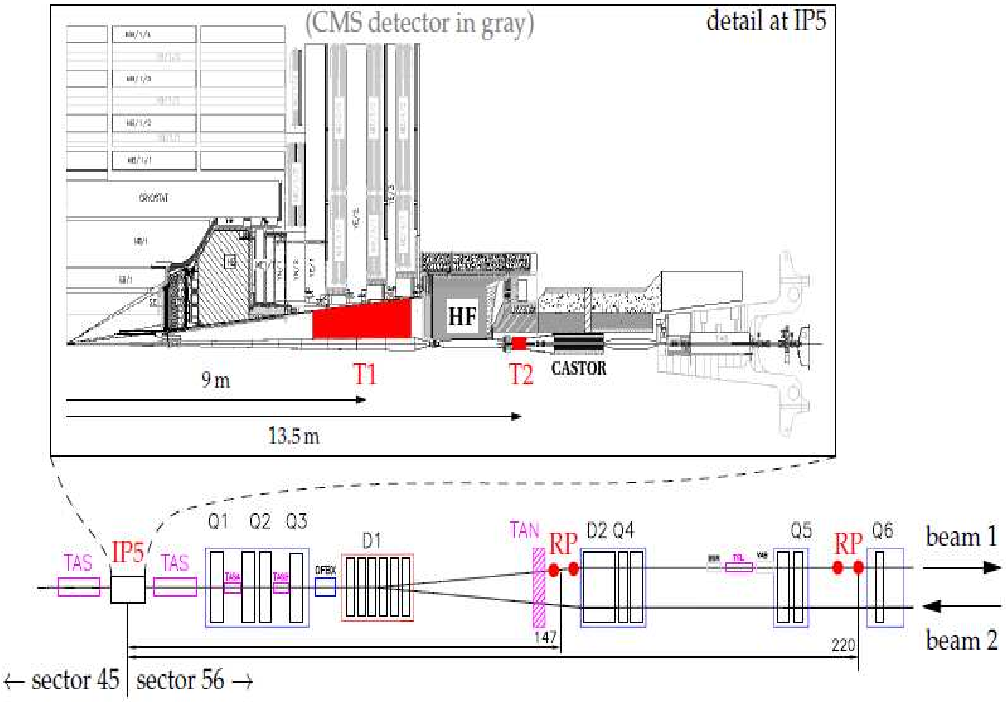

Figure 2.1: The TOTEM detectors placed around IP5. Top: the TOTEM forward trackers T1 and T2 embedded into the forward region of the CMS detector. Bottom: the TOTEM Roman Pots location along the LHC beam line at a distance of about 147 m (RP147) and 220 m (RP220) from the interaction point IP5. All TOTEM detectors are located on both sides of IP5.

The combination of the CMS and TOTEM experiments represents the largest acceptance detector ever built at a hadron collider. To facilitate the implementation of a common triggering system which is necessary in order to perform common TOTEM-CMS data taking, the TOTEM data acquisition system (DAQ) is designed to be compatible with the CMS one. A common trigger system has already been successfully commissioned and common Physics analyses are ongoing. Since the Physics processes studied by TOTEM have large cross sections, TOTEM is designed to cope with a low pile-up configuration. Indeed, with the current spatial vertex resolution, it is not possible to disentangle additional events vertices. Moreover, the cathod strip chamber technology is not suitable for the hard radiation environment associated to high luminosity scenarios. A program of detectors upgrade is currently under study: the aim is to provide the TOTEM detectors with timing information, to be used in order to associate the TOTEM tracks to the correct vertex reconstructed by CMS. The realisation of this program would provide CMS and TOTEM with a powerful tool for the identification of the rapidity gaps in hard and semi-hard diffractive interactions, even in a high luminosity scenario. This can potentially allow the study of very rare events produced diffractively.

2.1.1 The RP detector

The detection of the leading protons from diffractive and elastic interactions is performed by movable beam insertions called "Roman Pots" (RP). The Roman Pot is an experimental technique introduced at the ISR and successfully employed in later colliders like the $Sp\bar{p}S$, TeVatron, RHIC and DESY. The TOTEM silicon detectors are placed inside a secondary vacuum vessel, called "pot", and moved into the primary vacuum of the machine through vacuum bellows. In this way the detectors are physically separated from the primary vacuum which is so preserved against an uncontrolled out-gassing of the detector materials. Moreover, once a stable beam condition is reached, they can be moved very close to the beam axis, which allows to detect the protons at very small angles. The RP system consists of of four stations (placed at about ±140 and ±220 m from the IP), each one composed by two units, about 4 m distant. Each unit is composed by one RP approaching the beam horizontally and two RPs approaching the beam vertically from below or above the z axis (see fig. 2.2). Each pot is equipped with a set of 10 planes of edgeless planar silicon strip detector. Half of them have their strips oriented at an angle of $+45°$ with respect to the edge facing the beam, and the others at an angle of $-45°$. Each plane has 512 strips with a pitch of 66 μm, allowing a single hit resolution of about 20 μm. A scheme of the silicon detector and a picture of a stack of 10 detectors placed in a pot are reported in fig. 2.3.

The silicon detectors inside the pots are characterized by an "edgeless" technology: the physical edge of the detector is provided with a "Current Terminating Structure" where the potential applied to bias the device is applied also across the cut edges via a guardring running along the die cut and surrounding the whole sample. This external guardring, also called "Current Terminating Ring", collects the current generated in the highly dam-

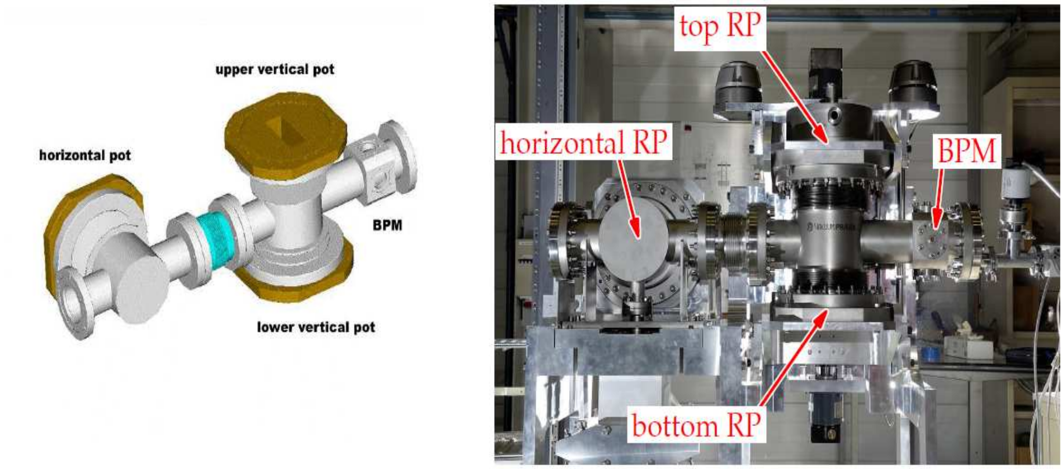

Figure 2.2: Left: scheme of a RP unit. Right: one RP unit installed in the tunnel.

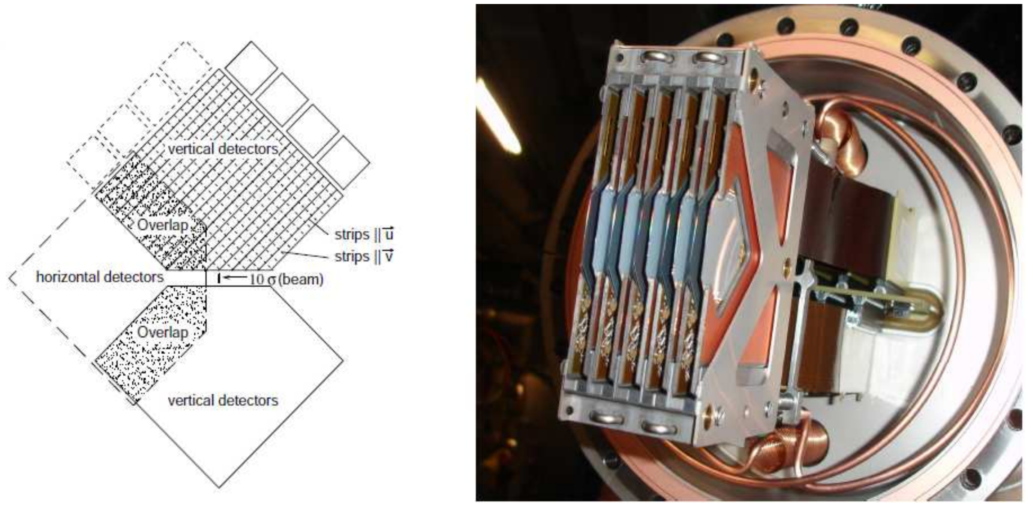

Figure 2.3: Left: the overlap among the horizontal and vertical silicon detectors. Right: a set of 10 detectors placed in a RP.

aged region at the cut edge, avoiding its diffusion into the sensitive volume. With this technology the sensitive volume starts at less than 50 μm from the cut edge.

The measurement of the leading proton strongly depends on the beam optics configuration. The so called "optical functions" determine the explicit path of the proton through the magnet elements as a function of the particle parameters at the IP (see fig. 2.5, top). Their values are known as a function of the proton position along the LHC orbit (s) and depend both on the magnet configuration and on the process of the bunches preparation.

The equations which relate the proton kinematical quantities measured at the RP position to the original values at the IP (the ones which are relevant for the Physics) are given by:

$$\begin{pmatrix} x \\ \theta_x \\ y \\ \theta_y \\ \xi \end{pmatrix} = \begin{pmatrix} v_x & L_x & 0 & 0 & D_x \\ v'_x & L'_x & 0 & 0 & D'_x \\ 0 & 0 & v_y & L_y & 0 \\ 0 & 0 & v'_y & L'_y & 0 \\ 0 & 0 & 0 & 0 & 1 \end{pmatrix} \begin{pmatrix} x^* \\ \theta^*_x \\ y^* \\ \theta^*_y \\ \xi^* \end{pmatrix}$$

where the right (left) hand side of the equation refers to the kinematical quantities at the IP (RP) position respectively. In particular x, y, θ_x and θ_y are the proton transverse position and the projections of the polar angle in the XZ and YZ planes. The prime symbol indicates the derivative with respect to the beam axis coordinate (s) and $\xi \equiv \frac{\Delta p}{p}$ is the fractional momentum lost by the proton during the physics process. The matrix, called "transport matrix", contains the optical functions.

The "effective lengths" and the "'magnifications" are given by $L_{x,y} = \sqrt{\beta_{x,y}\beta^*} \sin \Delta\mu_{x,y}$ and $v_{x,y} = \sqrt{\frac{\beta_{x,y}}{\beta^*}} \cos \Delta\mu_{x,y}$ respectively. β is the "beta function" and $\Delta\mu_{x,y}$ is the "phase advance" relative to the IP. The effective length and the magnification are reported in fig. 2.4, as function of the distance s to IP5 for $\beta^* = 90$ m and $\beta^* = 1540$ m optics.

In order to maximise the sensitivity of the position measurement to the scattering angle, while minimising its dependence on the vertex position, special optics are designed with a minimum beam divergence (σ_θ) at the IP (therefore a large β^* is needed since $\sigma_\theta = \sqrt{\epsilon_n/\beta_*}$ where ϵ_n is the normalized emittance), large values of L and v = 0 (which means $\Delta\mu_{x,y} = \pi/2$ in at least one projection at the RP location). The independence of the measured scattering angle on the vertex position is called "parallel to point focussing condition". For the largest β^* optics planned for TOTEM, with $\beta^* = 1540$ m, this is fulfilled in both x and y projections. With $\beta^* = 90$ m, already used for the first publications on total and elastic pp cross section measurements (see sec. 2.3), the parallel to point focussing condition is achieved only in the vertical plane ($\Delta\mu_y \sim \pi/2$, $L_y \sim$ 260m, $v_y \sim 0$), whereas in the horizontal plane $\Delta\mu_y \sim \pi$ and hence $L_x \sim 0$ (see fig. 2.4) . The typical beam divergence for this optics is $\sigma^*_\theta \sim 2.5$ μrad. With this optics the angle at the interaction point of the elastically scattered protons is therefore given by:

$$\theta^*_y = \frac{y}{L_y} \qquad , \qquad \theta^*_x = \frac{1}{\frac{dL_x}{ds}}(\theta_x - \frac{dv_x}{ds}x^*) \tag{2.1}$$

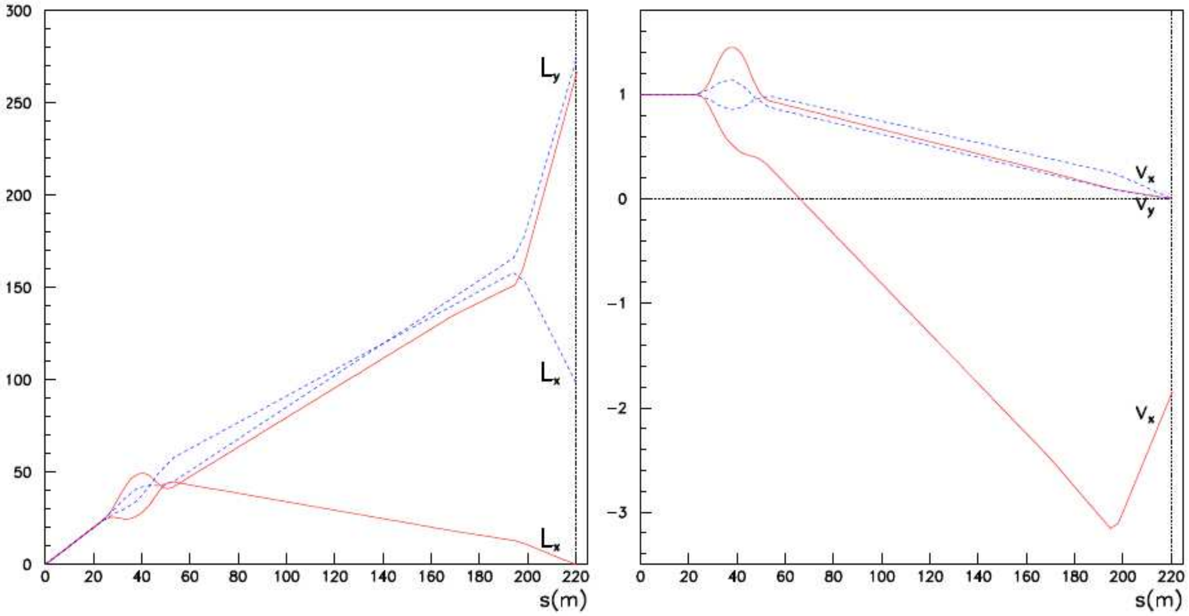

Figure 2.4: The effective length L (left) and the magnification v (right) for $\beta^* = 90$ m (solid curve) and $\beta^* = 1540$ m (dashed curve).

The vertical scattering angle θ_y^* is directly reconstructed from the track position y whereas (due to $L_x \sim 0$) the horizontal component θ_x^* is optimally reconstructed from the track angle $\theta_x = dx/ds$, estimated from the reconstructed proton position in the two units of the RP station. The unmeasured vertex produces a smearing term due to x^*. However, this dependence doesn't affect the analysis of the elastic scattering since the vertex term cancels due to the correlation between the collinear tracks of the two outgoing protons.

Is it also important to notice that the t-acceptance of the proton is also dependent on the optics. A measurement of the RP acceptance for elastic events is shown in fig. 2.6, for three different values of β^*.

Fig. 2.5 (bottom) shows the scatter plot of the hits mainly due to elastically scattered protons, for the plus and minus vertical RPs, in runs at $\beta^* = 3.5$m (90 m) where $L_y \sim$ 20 m (200 m). With the larger β^* optics (fig. 2.5 left), because of the larger L_y only protons scattered at smaller angle can enter in the sensitive part of the RP while larger angle protons are lost. Instead the smaller β^* optics (fig. 2.5 right) allows the protons at larger scattering angle to reach the RP, while the smallest angles ones are not extracted from the beam and cannot reach the RP edges. More details on the proton transport and measurement can be found in [54, 55].

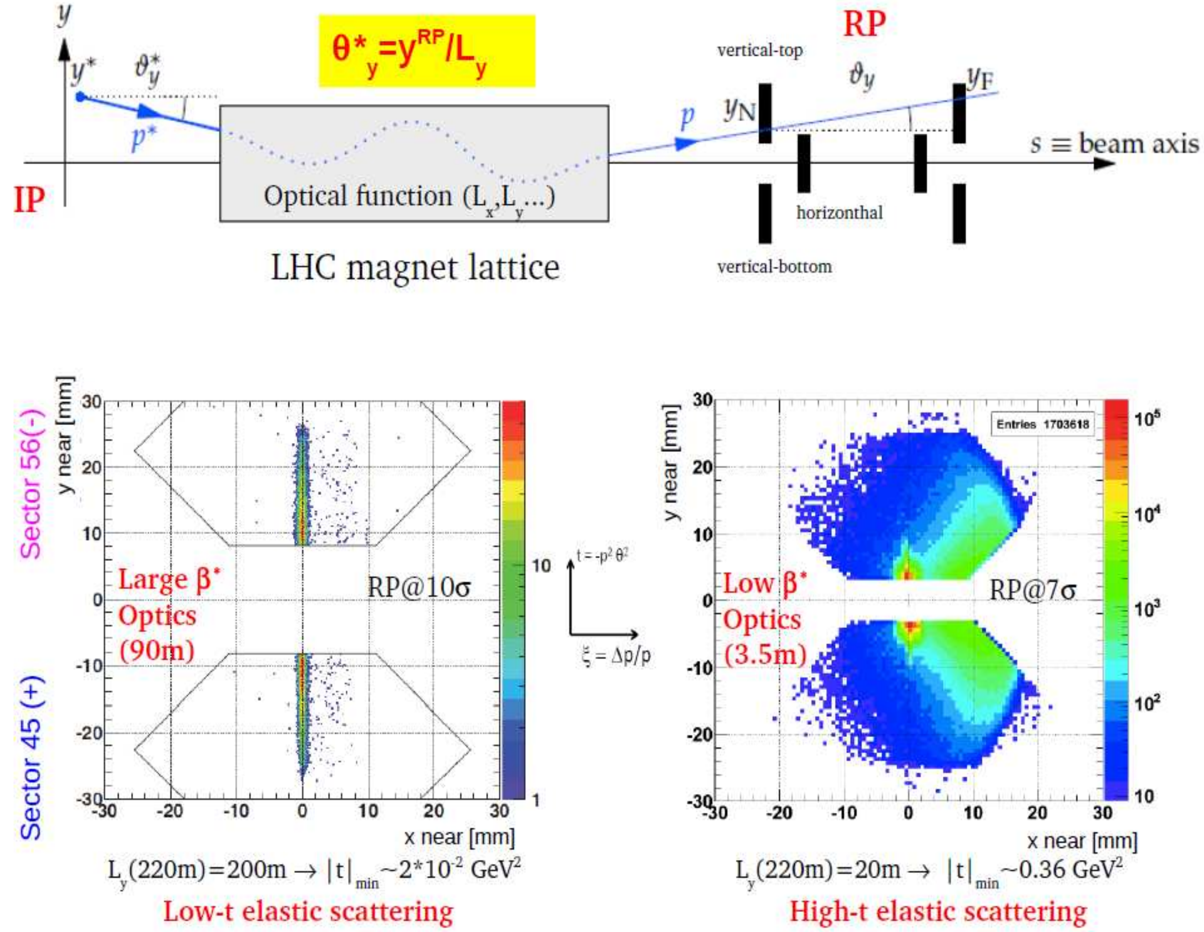

Figure 2.5: Top: Scheme of the proton transport from the IP to the RP stations. Bottom: hit distributions obtained for elastic scattering candidates (the elastic trigger condition has been required [4]) in the plus and in the minus vertical RP for a low β^* optics (right) and a high β^* optics (left) scenario.

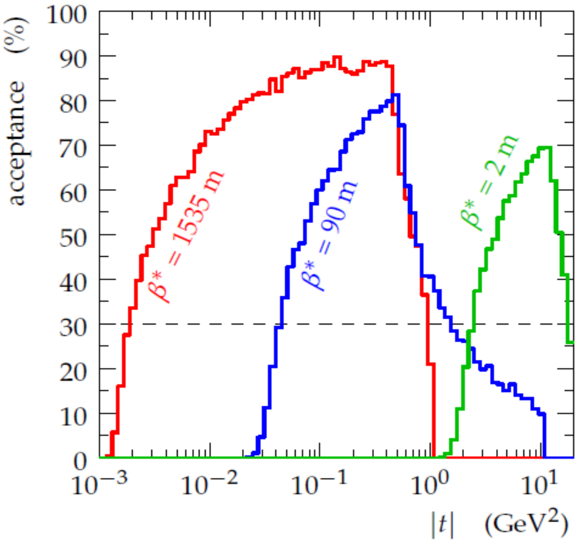

Figure 2.6: RP elastic events acceptances for three different optics at $\sqrt{s}$ = 14 TeV, with the RP sensors at $10\,\sigma_{beam}$ + 0.5 mm. The horizontal line marks the points where the acceptances reach 30% [54].

2.1.2 The T1 detector

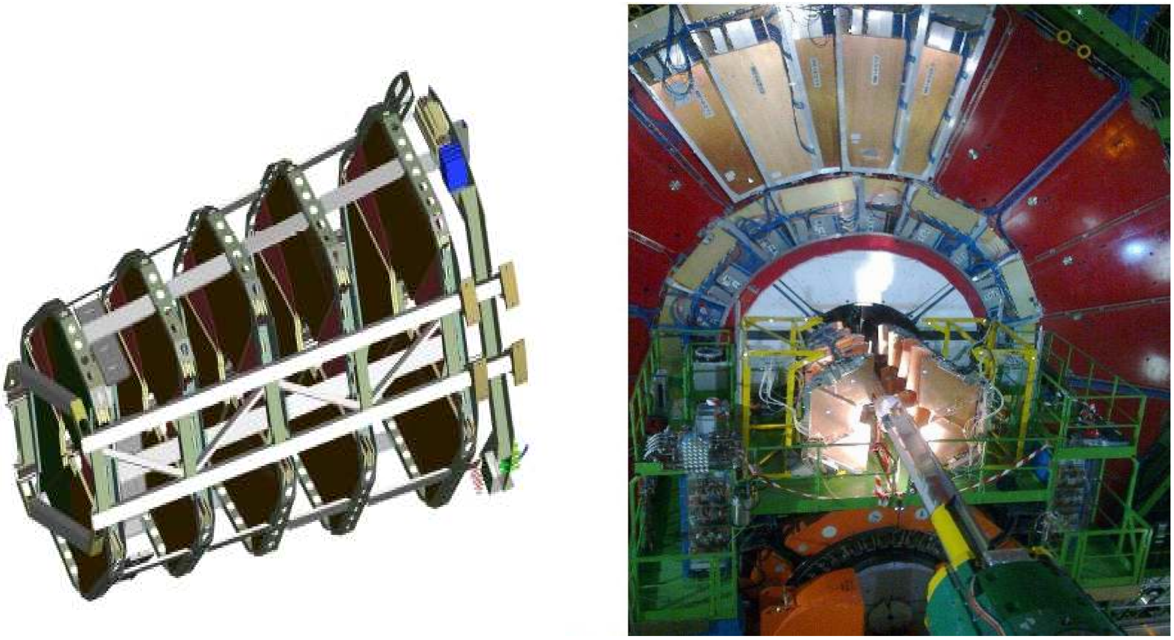

Figure 2.7: The TOTEM T1 telescope. Left: sketch of one arm. Right: installation of one arm in the CMS end-cap region.

The T1 telescope [52] is installed in the CMS endcaps region, at a distance of 7.5 to 10.5 m from the IP5. Each arm of T1 (see fig. 2.7), covers the pseudorapidity range $3.1 < |\eta| < 4.7$ (corresponding to a polar angle $18 < \theta < 90$ mrad) and is composed of five planes of Cathode Strip Chambers (CSC), equally spaced in z. Each plane consists of six trapezoidal detectors covering roughly a region of $60\,^{\circ}$. The Cathode Strip Chamber is a multi-wire proportional chamber with segmented cathode read-out. The detector sextants in each plane are rotated with respect to the corresponding ones in the other planes by angles varying from -6° to $+6^{\circ}$ in steps of 3°, in order to improve the pattern recognition for track reconstruction and to reduce the localised concentration of material in front of the CMS HF calorimeter. The printed boards for the two sides of a CSC are identical and give an assembled detector with cathode strips having an angle of $\pm 60^{\circ}$ with respect to the orientation of the gold-plated tungsten anodic wires used for the radial coordinate measurement. The disposition of the cathodic strips and anodic wires fired in one plane of T1 traversed by three charged particles is sketched in fig. 2.8 (left). One cathodic strip plane is shown in fig. 2.8 (right).

Table 2.1 [52] summarises the basic parameters of the T1 CSC detectors.

Full gas gap	10 mm
Wire spacing	3 mm
Wire diameter	30 μm
Strip pitch	5 mm
Strip width	4.5 mm
Chamber thickness	43 mm

Table 2.1: T1 CSC chamber basic parameters.

Measurements performed on the LHC data have shown that a spatial resolution of about 1 mm in the three coordinates can be obtained. By requiring at least a charged particle with $\mathrm{p}_T > 100$ MeV, the T1 individual arm inelastic event reconstruction efficiency was estimated to be $\sim$98 %, using a simulation where the CSC efficiencies are tuned on the data. From studies on primary vertex resolution in the Z direction the position of each chamber along the Z axis is known with a precision of 4 mm. By studying the hit residuals, the misalignment uncertainty on the plane transverse position has been found smaller than 100 μm. Aging studies, performed at the CERN Gamma Irradiation Facility, have shown no loss of performance after an irradiation resulting in a total charge integrated on the anode wires of 0.065 C/cm, which corresponds to an accumulated dose equivalent to about 5 years of running at a luminosity of 10^{30} cm^{-2}s^{-1}.

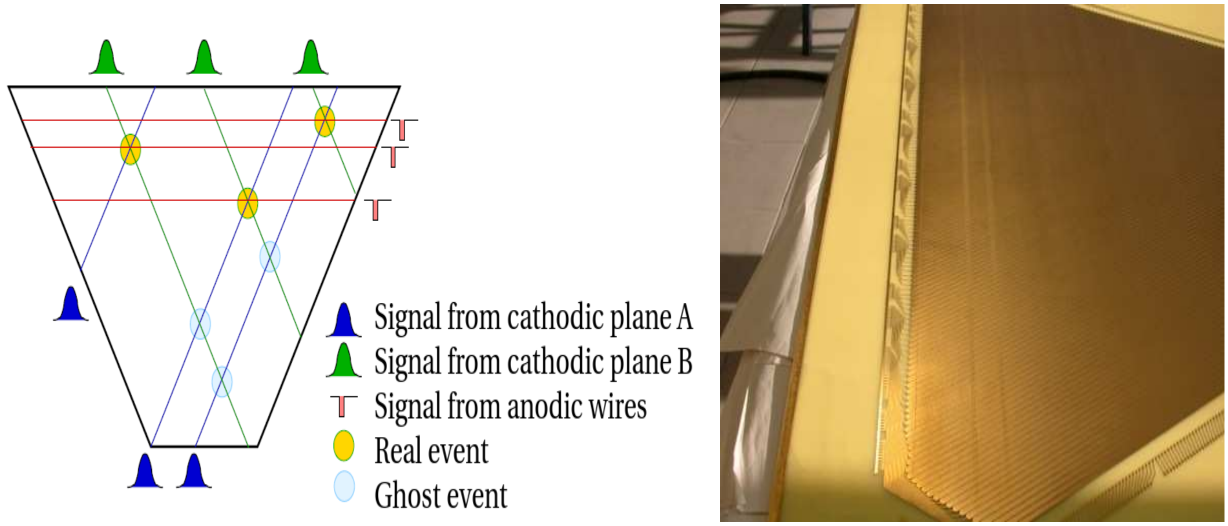

Figure 2.8: Left: cathodic strips and anodic wires fired in one plane of T1. Real (ghost) particles are represented by yellow (light blue) circles. Right: picture of a cathodic strip plane.

2.1.3 The T2 detector

The T2 telescope, placed at about 14 m from the IP, detects charged particles produced in the pseudorapidity range $5.3 < |\eta| < 6.5$ (corresponding to a polar angular range $3 < \theta < 10$ mrad). One arm of the T2 telescope consists of 2 quarters, each one composed by 10 triple-GEM (Gas Electron Multipliers) semicircular chambers [56] (see fig. 2.9).

The T2 GEMs [57, 58] use the same baseline design as the one adopted by the COMPASS experiment [59] with a "triple-GEM" structure (see fig. 2.10, left): three GEM foils are used in cascade in order to achieve a high gain ($\sim$ 8000), reducing at the same time the discharge probability (below 10^{-12}). Each GEM foil consists of a 50 μm polyimide plane with 5 μm copper cladding on both sides. By using conventional photo-lithographic methods, a high density of double conical holes (with a distance of 140 μm) is realised (see fig. 2.11, left). The diameter of the holes used in the T2 GEMs is 55 μm in the middle of the plane and 70 μm on the surface.

Ionizing particles interact with the gas filling the chamber (Ar/CO_2 70/30 at atmospheric pressure) in the drift zone (see left picture on fig 2.10), producing primary electrons. An electric field of about 2.4 KV/cm carries the electrons towards the holes of the top GEM-plane, where an electric field of about 67 KV/cm is present. Such high field generates the electron multiplication (about a factor 20 for this configuration) inside the GEM channels. In the transfer zone 1 and 2 an electric field of about 3.6 KV/cm guides

Figure 2.9: The TOTEM T2 telescope. Left: one detector plane. Right: installation of one arm in the CMS hadron-forward region.

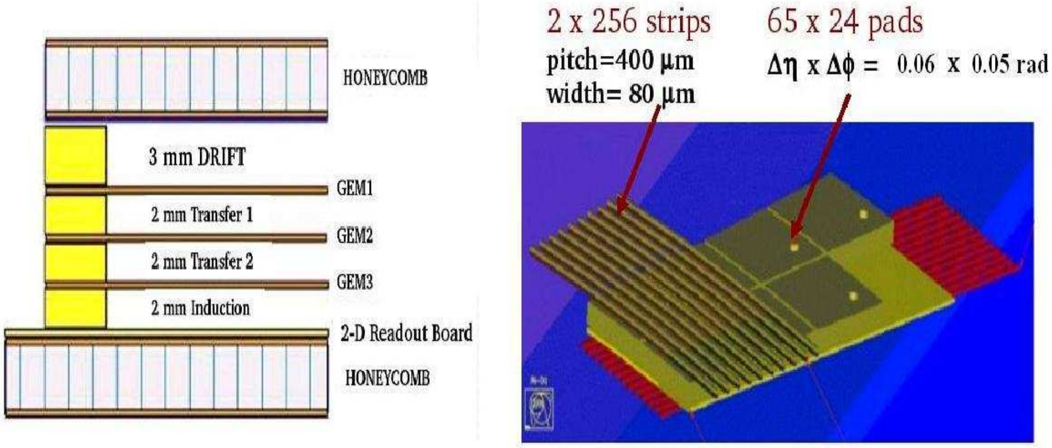

Figure 2.10: Left: transverse view of the T2 triple GEM detector. The charges released by the ionizing particle in the 3 mm drift zone are amplified by each GEM foil and then collected on the read-out board. Right: part of the read-out board showing the patterns of the two separate layers.

the electron cloud towards the successive GEM planes which have an internal electric field of about 61 and 55 KV/cm for the central and the bottom foil respectively. The charges

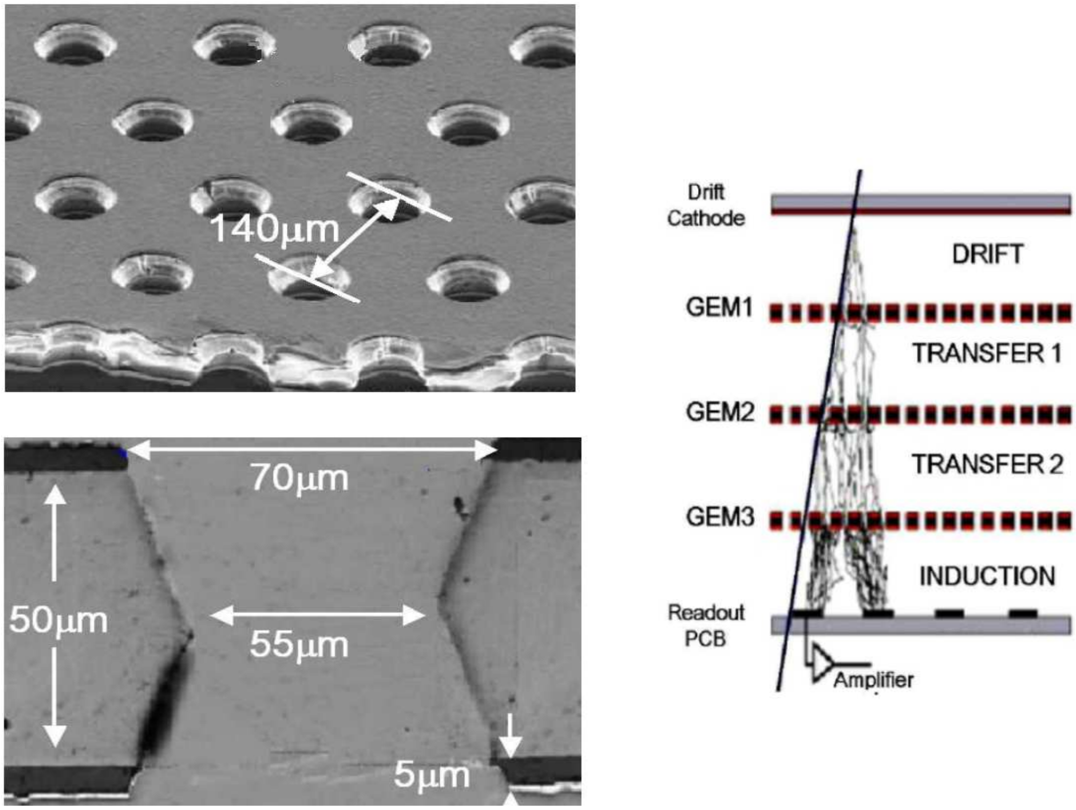

Figure 2.11: Left: picture of a GEM foil. The foil is made with a 50 μm polyimide foil with 5 μm copper cladding on both sides. The distance of the hole is 140 μm. A bidirectional wet etching process caused the double conical shape of the holes [60]. Right: sketch of the amplification processes of a ionizing particle through the three GEM foils.

are finally collected on the readout board through an electric field of about 4.4 KV/cm. The above description, resumed also in fig. 2.11 (right), reveals a key feature of the GEM detectors: the amplification and the readout stages are fully decoupled, allowing a more powerful chamber optimisation.

Each chamber provides a two-dimensional information of the track position in the plane transverse to the beam axis, with an azimuthal coverage of $192\,^{\circ}$ [58]. The small overlap region around the vertical axis between the two neighbouring quarters (of about $12\,^{\circ}$) is used for alignment purpose (see ch. 4) and also allows to minimise inefficiencies at the detectors edges. Every chamber has a double layered read-out board containing two columns of 256 concentric strips ($400\,\mu m$ pitch, $80\,\mu m$ width) for the measurement of the radial coordinate and a matrix of 1560 pads, each one covering $\Delta\eta \times \Delta\phi\ \simeq 0.06 \times 0.018$ rad, for the measurement of the azimuthal coordinate and for triggering (see fig. 2.10, right).

More details on the hit and tracking resolution are reported in ch. 3. The total amount of material of 10 chambers placed in one T2 quarter corresponds to only $\sim 0.05\ X_0$ [60].

The GEM technology is characterized by a high rate capability and a good resistance to radiation. These characteristics are very important especially if T2 will be used in high luminosity runs together with the CMS detectors. Simulation studies have shown that in the T2 region at a luminosity of $\mathcal{L} = 10^{33}$ cm^{-2}s^{-1} a charged hadrons rate of 1-2 MHz/cm^2 is expected. When the contribution of the secondary particles is included, this rate has to be multiplied by a factor 10, which means that on average a pad is hit with a frequence of 4 MHz. For this luminosity, the dose received by electronics are expected to be $\sim$ 5Mrad/year. The time response of the detector should be compatible with this requirement. Indeed the VFAT2 chip has its time constants below 25 ns and the GEM gaseous detectors, chosen for the T2 telescope, have shown no variation in performances at rate of $\sim$20 MHz/cm^2.

Fig. 2.12 shows the neutron equivalent particle fluence (Φ_{eq}) measured in both arms of the T2 telescope until the end of the winter technical stop (February 2011) [61].

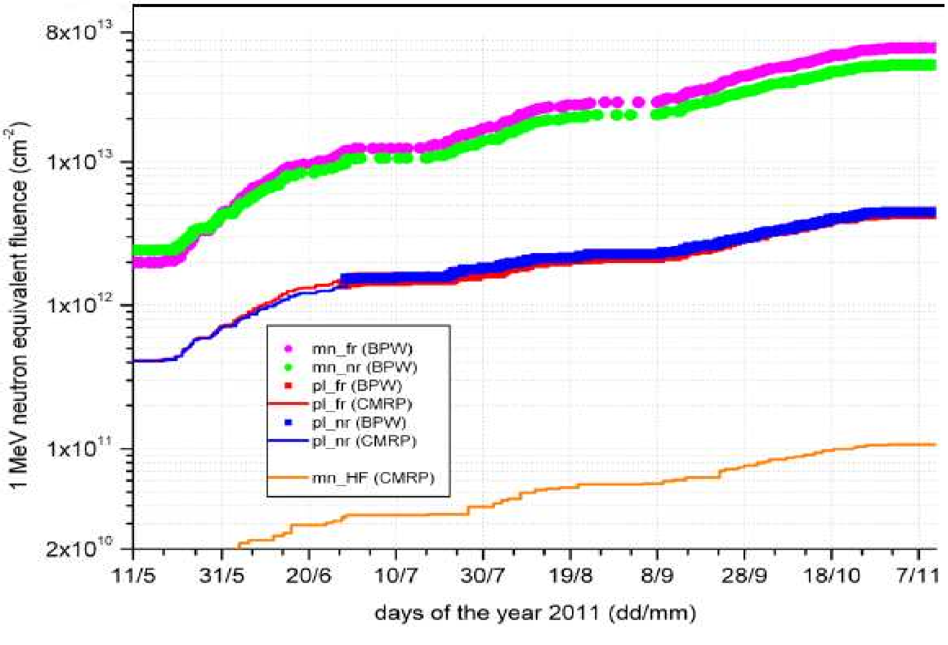

Figure 2.12: Φ_{eq} measured in both arms of the T2 telescope with high-sensitivity p-i-n diodes. The four upper curves shows the measurements of the fluence for each of the T2 quarters. In particular, pink and green curves refer to the minus side while blue and red ones represent the measurements on the plus side.

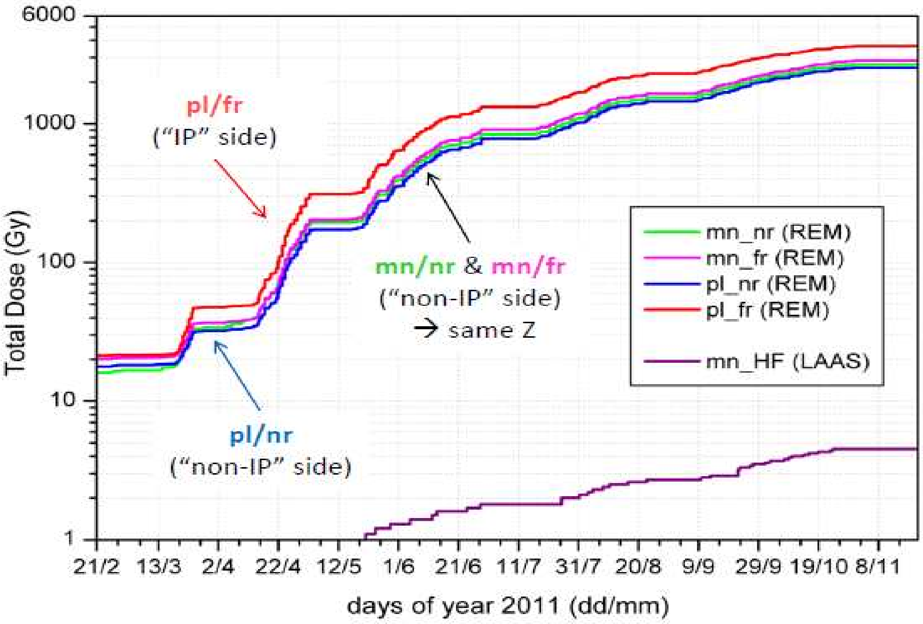

Figure 2.13: Total dose measured in both arms of the T2 telescope with active sensors, sensitive to γ, $e^{\pm}$ and hadrons. The four upper curves shows the measurements of the total dose for each of the T2 quarters.

The blue and red curves show the Φ_{eq} recorded on the plus arm of T2, while the other two refer to the minus arm. The difference between the two arms (of about a factor 8) is due to high-energy neutrons generated by the CASTOR calorimeter which sits only on the minus side of the CMS experiment. The dose associated to the delivered 50 pb^{-1} of 7 TeV pp integrated luminosity in T2 reached already the level of about 1 kGy in the first semester 2011, making T2 the most exposed TOTEM sub-detector. The total dose integrated by the T2 detector as a function of time, is reported in fig. 2.13. Studies performed on triple GEM detectors ensure that no aging effects will take place for a time period equal to the one needed to perform all the relevant measurements for TOTEM. The front end electronics chosen has been tested up to 10 Mrad without any degradation of its nominal performances.

2.1.4 The forward region and the beam pipe

A large amount of secondary particles is generated by the interactions of the primary particles with the material placed in front and around T2. Part of these secondary particles is subsequently reconstructed in the T2 detector and contributes to the worsening of the performances of the reconstruction algorithms (see ch. 3). This section is therefore dedicated to the description of the regions most relevant for the secondary particles production. These were found to be the beam pipe (BP) and the lower edge of the HF calorimeter.

For what concerns the BP region this is typically described in terms of two region: the "endcap region" is defined at $|z| < 10600$ mm while the "forward region" [51] is defined as the zone around IP5 ranging from $|z| = 10600$ mm to 18000 mm (see Fig. 2.14). The former, being of minor importance in terms of secondary particle production is not furthermore described. From $|z| = 10600$ mm a conical section with an angle of 30° and a wall thickness of 2.5 mm reduces the diameter from 313,8 mm (reached at the end of the EndCap region) to 170 mm. This section covers a pseudo-rapidity region from $\eta = 4.9$ to $\eta = 5.53$. From $|z|$ = 10720 mm to $|z| = 13340$ mm another conical section, pointing to IP with $\eta = 5.53$, runs under the CMS Hadronic Forward (HF) calorimeter. This section ends with a stainless steel window, perpendicular to the beam axis, which reduces the beam pipe diameter from 210 mm to 55 mm and has a thickness of 0.1 mm. Inside the beam pipe a perforated conical copper section 0.2 mm thick (acting as a "R.F. shield") performs the same diameter reduction. The window and the copper cone intercept all particles with η from 5.53 to 6.88. Close to the window, three ion pumps (see fig. 2.14, bottom) are installed at $\eta < 5.3$. T2 is placed immediately behind these pumps, starting at $|z|$ = 13828 mm. The last beam pipe section of interest is the cylindrical pipe starting from $|z| \sim 13340$ mm and running inside the T2 telescope (see fig. 2.14). It is 1 mm thick, with an inner diameter of 55 mm and intercepts particles with $6.88 < \eta < 6.94$[1]. Considering the radiation length ($X_0 = 17.35$ mm) and the nuclear interaction length ($\lambda_I \sim$ 17 cm) for stainless steel, it is possible to estimate the amount of beam pipe material (in terms of X_0 and λ_I) which is crossed by a particle generated at the IP as function of its η.

particle η	t/λ_I	t/X_0	σ_θ (mrad)
$4.9 < \eta < 5.53$	< 0.03	< 0.3	~ 0.7
$\eta \sim 5.53$	> 15	> 150	-
$5.53 < \eta < 6.88$	0.0006	0.006	~ 0.32
$6.88 < \eta < 6.94$	2.8-3.0	27-29	7.1-7.4

Table 2.2: Beam pipe effective thickness (in units of radiation length and interaction length in steel) traversed by a particle generated at the IP, as a function of its η. The polar angle spread due to multiple scattering (for a π^- of E = 10 GeV) is also shown as reference. The effect of the thin conical copper section inside the beam pipe at η from 5.53 to 6.88 is neglected.

---

[1] The last value is calculated at z = 14228 mm

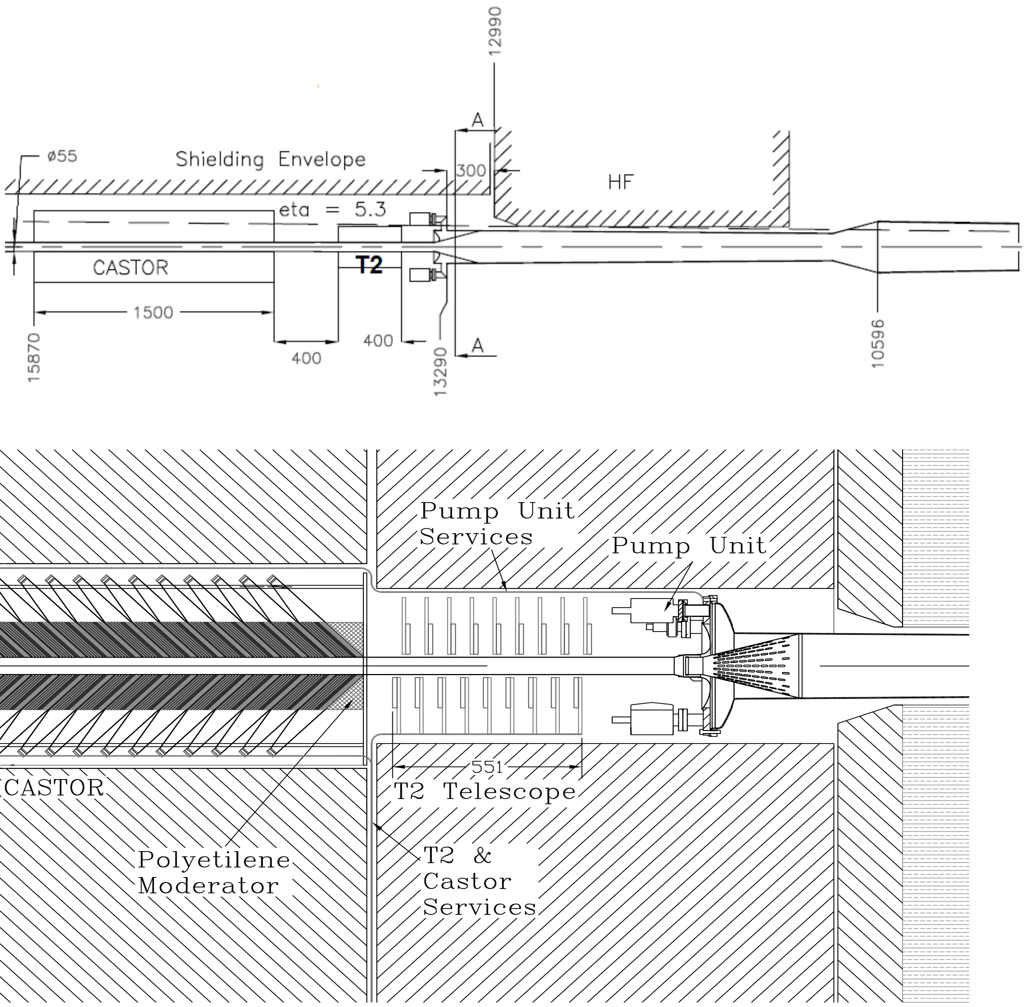

Figure 2.14: Top: the beam pipe in the forward region with the specification of the distances from IP. The location of the TOTEM T2 telescope and of the CMS CASTOR and HF calorimeters is also shown. Bottom: location of the T2 telescope, installed between the ion pumps and the CMS CASTOR calorimeter.

Table 2.2 summarises the results [62], also showing (as reference) the RMS of the polar angle distribution σ_θ for a π^- with E = 10 GeV, due to multiple scattering[2]. It is thus clear

---

[2] The calculation of σ_θ is done by using the following equation [63]:

$$\sigma_\theta = \frac{13.6\mathrm{MeV}}{\beta c p}\, z \sqrt{\frac{t}{X_0}}\,[1 + 0.038\ln(t/X_0)] \qquad (2.2)$$

where p, βc and z are the momentum, velocity and charge number of the incident particle and t is the effective amount of traversed material that particles generated in the $6.88 < \eta < 6.94$ range, crossing up to more than 40 cm of steel, can start nuclear or electromagnetic showers. The same considerations are valid also for η around 5.53, where more than 2.5 m of steel can be crossed by the particle.

An additional contribution to the production of the secondary particle going in T2 is given by the HF calorimeter. In particular the lower edge of this calorimeter is responsible for the generation of electromagnetic and hadronic showers. In fig. 2.15 the average pad cluster multiplicity reconstructed in the first plane is shown as a function of the simulated particle η, both for π^+ (left) and photon (right) uniformly generated in the energy range $10 <$ E < 60 GeV [64]. As fig. 2.15 (left) shows, a single photon generated in the pseudorapidity range of $5.3 < |\eta| < 5.32$ can produce more than 20 pad cluster per plane.

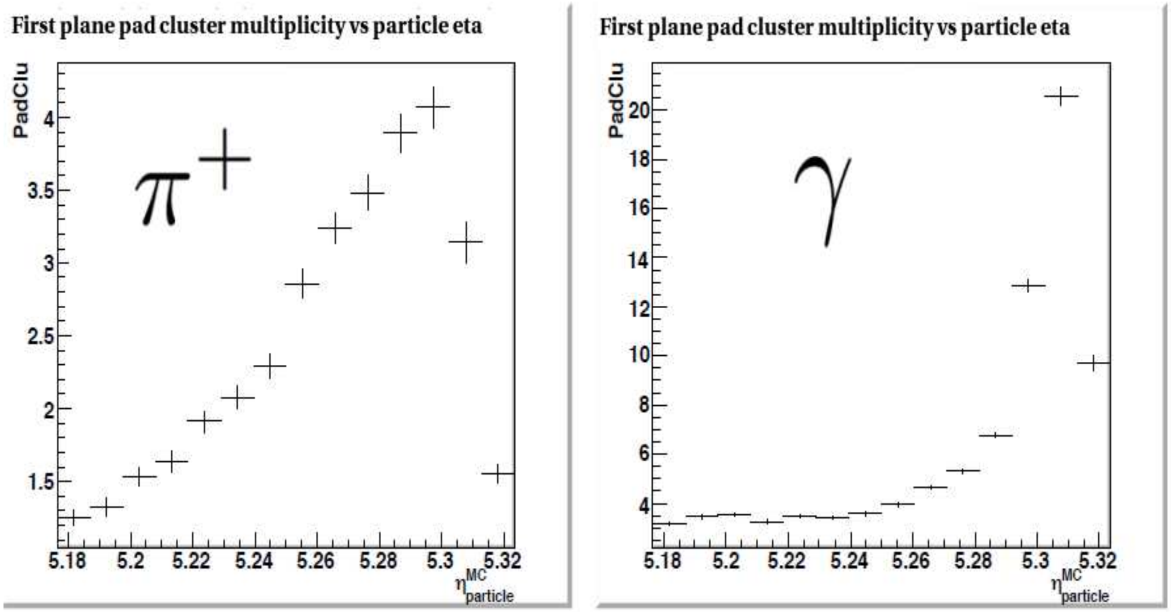

Figure 2.15: Average pad cluster multiplicity in the first plane of a quarter as a function of the particle η for π^+ (left) and photon (right).

2.2 The TOTEM Physics Program

The TOTEM experiment has been designed to measure the pp total cross section at LHC with an uncertainty of about 1 mb. Moreover, the experiment aims to measure the elastic scattering on a wide range of the squared four momentum transfer $10^{-3} < |t| < 10$ GeV^2 and to study the diffractive dissociation, partially in cooperation with CMS. The measurement of the total cross section is achieved by using the luminosity independent method (see sec. 1.1.1). This requires the determination of the total elastic (N_{el}) and inelastic (N_{inel}) rate, as well as the extrapolation of dN_{el}/dt to $t = 0$ and the estimation of ρ.

The prediction of $d\sigma_{el}/dt$ at 14 TeV obtained from several theoretical model is reported in fig. 2.16. Depending on the physics involved, several regions in t can be identified to describe the differential elastic cross section[3]:

- $|t| < 10^{-5}\,\mathrm{GeV}^2$: the Coulomb region, where elastic scattering is dominated by one photon exchange described by the Rutherford formula: $d\sigma/dt \sim 1/t^2$.
- $2 \times 10^{-3}\,\mathrm{GeV}^2 < |t| < 0.4\,\mathrm{GeV}^2$: the hadronic region, where the differential cross section is approximately exponential: $d\sigma/dt \sim \mathrm{e}^{-B\,|t|}$.
- Between the above two regions, the interference between the nuclear and Coulomb scattering complicates the extrapolation of the nuclear cross section to $t = 0$.
- $|t| > 0.4\,\mathrm{GeV}^2$: the region of the diffractive deep. As shown in fig. 2.16 the appearance of diffractive maxima and minima recalls the distribution of the light intensity of a plane wave diffracted by a circular disk.
- $|t| > 1.5 \div 3\,\mathrm{GeV}^2$: in this region there is the domain of central elastic collisions which might be described by perturbative QCD, e.g., in terms of three gluon exchange with a predicted cross section proportional to $|t|^{-8}$ [65].

All models predict (with the exception of the one of Islam et al. [66]) an almost exponential behaviour of the differential cross section at small t (up to about 0.2 GeV^2).

The interference region and the beginning of the hadronic region are important for the extrapolation of the differential elastic rate (dN_{el}/dt) to the optical point ($t = 0$), therefore for the σ_{tot} measurement. The exponential slope, defined as $B(t) \equiv \frac{d}{dt} \ln \frac{d\sigma}{dt}$, are reported in fig. 2.17. The elastic scattering cross section can be described by means of an exponential only for $|t|$ down to 1-2$\cdot 10^{-3}$ GeV^2. Indeed, at lower $|t|$ the Coulomb scattering becomes important and so also the interference between hadronic and Coulomb scattering has to be taken into account. In this region, the t-dependence of the exponential slope $B(t) = \frac{d}{dt} \ln \frac{d\sigma}{dt}$ is model dependent. This theoretical uncertainty contributes to the systematic error on the total cross-section measurement. The elastic scattering can be indeed described by the following expression:

$$\frac{d\sigma}{dt} = \frac{16\pi}{s^2} |F_c\, e^{\mp i\alpha\phi} + F_h|^2 \tag{2.3}$$

---

[3] The value reported hereafter refers to the elastic scattering at 14 TeV.

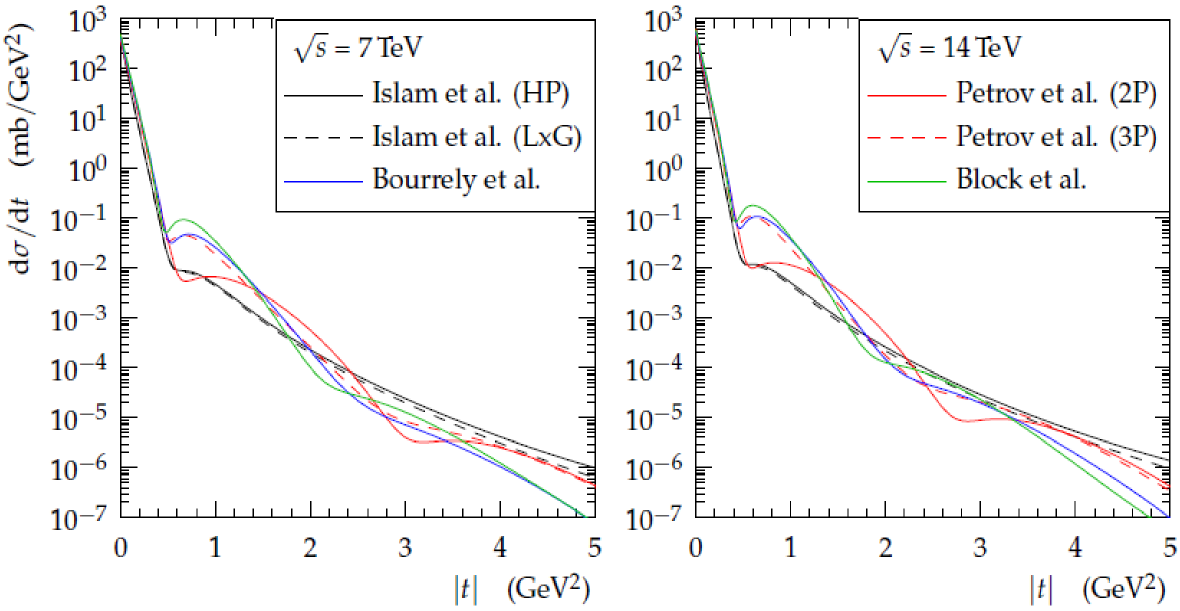

Figure 2.16: Differential elastic cross section for several theoretical models obtained at 7 TeV (left) and 14 TeV (right)[54].

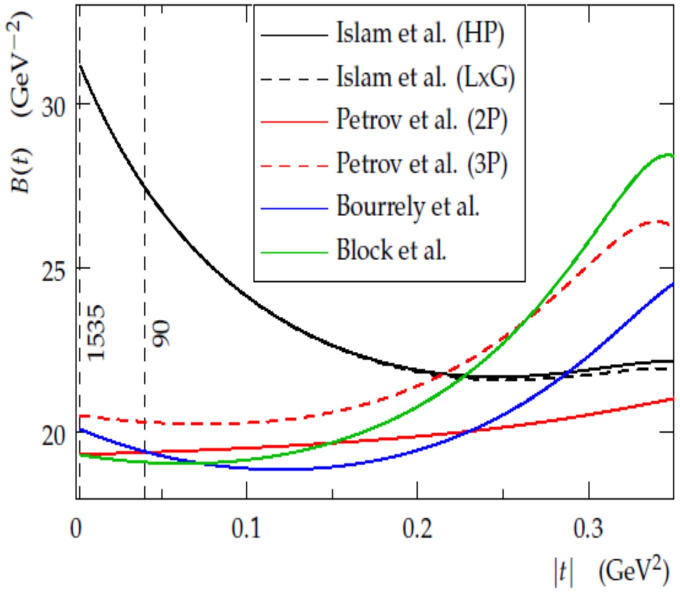

Figure 2.17: Elastic slope $B(t)$ for several theoretical models obtained at 14 TeV [54]. The vertical dashed lines show the values of t for which the acceptance is 30% for $\beta^* = 90$ m and $\beta^* = 1535$ m .

with:

$$F_c = \pm\frac{1}{2}\alpha\frac{G^2(t)}{|t|}$$

$$F_h = \frac{s}{16\pi}\sigma_{tot}(\rho+i)e^{-B|t|/2} \tag{2.4}$$

(2.5)

where F_c and F_h are the Coulomb and hadronic scattering amplitude. The lower (upper) sign refers to pp ($p\bar{p}$) interactions. $\alpha\phi$ is the relative Coloumb-hadronic phase (with α being the fine structure constant) and $G(t)$ is the nucleon electromagnetic form factor. The function $\alpha\phi$ is usually taken as $\mp(\ln -B(s)t/2 + \gamma)$, where γ is the Euler constant, but presently it is known that this parametrisation is not fully theoretically consistent [67].

At a first stage the value of ρ used by the TOTEM experiment for the σ_{tot} measurement is taken from the COMPETE collaboration which found $\rho \sim 0.14$ [5]. In a later stage ρ may be directly determined by measuring the elastic differential cross section in the interference region. Fig. 2.18 shows the value of t where 50% of the acceptance is reached as function of the distance of the RP from the beam centre, for different value of the center of mass energy. The curve showing where the hadronic cross section equals the Coloumb one is also superimposed. Since above 1 TeV a low dependence of ρ on the energy is expected, it is easier to determine ρ at lower center of mass energies. The possibility to perform this measurement at 8 TeV, with an already available optics of 1 Km, is under study by the Collaboration.

The RP acceptance for elastic events (see sec. 2.1.1) is limited and depends on the optics configuration. Larger β^* optics allow to reach smaller values of $|t|$ and to minimise the error due to the extrapolation of $\mathrm{dN}_{el}/\mathrm{dt}$ to the optical point.

The importance of the measurement of the elastic cross section is not only at low $|t|$ where the cross section is large. At high $|t|$ it is indeed possible to distinguish among the many theoretical models describing the elastic interaction (see fig. 2.16, obtained before the publication of the TOTEM results on the elastic differential cross section).

The main contributions to the uncertainty on the inelastic rate is due to the limited acceptance of the experimental apparatus to diffractive processes at low masses. Indeed, while TOTEM can detect more than 99% of the non diffractive events, the detection efficiency of diffractive events at 7 TeV is about 80%, according to Pythia 6 and Pythia 8 MC. In particular the detection efficiency of diffractive masses (M) of ~3.4 GeV is 40-60% [64], being smaller for lower values of M.

The measurements of the diffractive cross sections are ongoing. In particular the differential cross section at low masses will be of much interest, since TOTEM is the only experiment able to put precise constraints on that. It is important to notice that during these years it has been realised that TOTEM has the potential to carry out several Physics measurement of great interest, beyond its standard program. In particular, the measurements of the forward charged particle pseudorapidity density and multiplicity have been proved in this thesis to be possible. These analyses can have a large impact on the physics com-

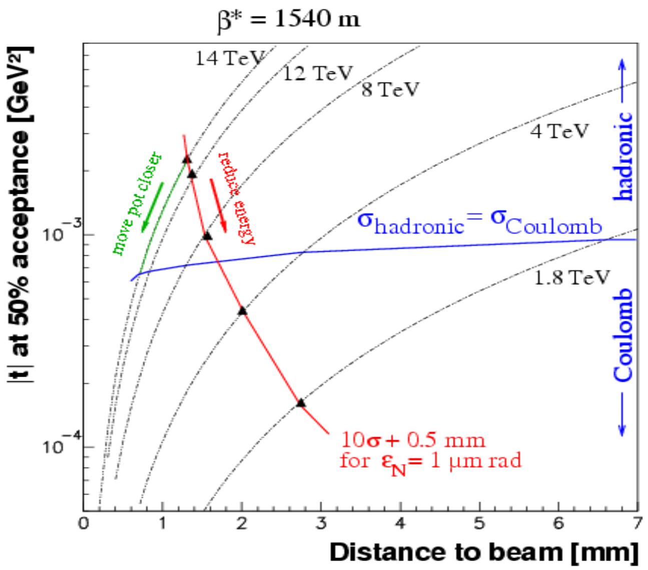

Figure 2.18: t value where 50% of RP acceptance is reached as a function of the RP distance from the beam centre, for different values of the center of mass energies. The blu curve indicates where the hadronic and Coloumb cross section are equal.

munity, especially if the data collected with a common CMS-TOTEM trigger will be used. With this common data acquisition large central rapidity gap can be identified and the presence of central jets can be established. Moreover the forward multiplicity and the particle correlations can be studied both in purely soft events and in events where central jets are produced (underlying event characterisation).

2.2.1 Connection with the cosmic rays Physics

The measurements performed by TOTEM are expected to be extremely valuable also for the improvement of the analyses on very high energy cosmic rays (CR).

When a hadronic high-energy particle enters the Earths atmosphere, it interacts with a nucleus of the air elements (mainly nitrogen, oxygen, and argon) at a typical height of 15 to 35 km, producing a shower of secondary particles[4]. Air shower simulation programs are essential tools for the analysis of data from cosmic ray experiments, as they are used to estimate the energy and the mass of the primary CR interacting in the atmosphere [68, 69]. While the incident direction of a CR can be reconstructed from the arrival times of the shower particles at different positions at the observation level, the primary energy and the mass of the CR are deduced by comparing the measured shower with model calculations for various primaries. The CR energy is approximately proportional to the total number

---

[4] In the CR-analysis jargon, the CR is also called “primary particle” while “secondary particles” are the ones produced in the showering processes.

of secondary particles produced and the CR mass is reflected in the depth of the shower maximum (X_{max}), and in the muon-to-electron ratio of the shower. The precise relations, however, depend on the shower model used for the comparison.

All interaction models used in the CRs analyses are developed on the basis of the physics knownledges from accelerator experiments. The models are tuned to reproduce measured cross-sections, multiplicities, p$_T$ and rapidity distributions, particle fractions and many other experimental data. Nuclear CR-Air reactions are reduced to nucleon-nucleon collisions via the Glauber theory [70]. Aiming at energies up to 10^{19} eV, the models are extrapolated far beyond the energies available at accelerators. Unfortunately model uncertainties translate directly into systematic errors in the energy and mass determination. The main uncertainty of contemporary models comes from our poor knowledge of the (soft) hadronic interactions at high energies. Very precise measurements of the quantities from which the models depend can be used to constraint and tune them at the energies reached at the LHC[5]. Fig. 2.19 shows the uncertainty on the proton-air cross section for particle production, as calculated with the Glauber framework due to the different predictions obtained by the models extrapolation from lower energies. More in general, the important experimental quantities that can be measured at a collider and which determine the properties of the air shower observables are: the hadronic particle production

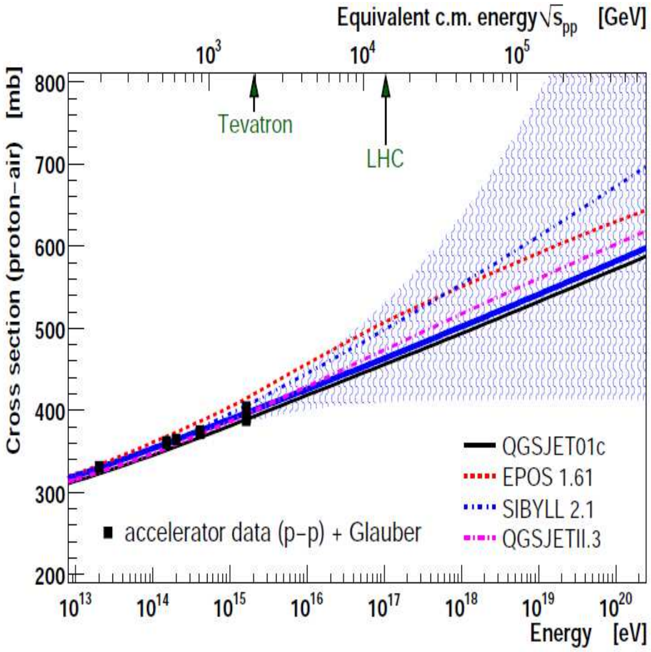

Figure 2.19: Uncertainty of the extrapolation of the proton-air cross section for particle production, due to different models of the pp cross section [71].

---

[5] A 14 TeV pp collisions center of mass energy corresponds to a CR proton energy of 100 PeV.

cross sections; the forward multiplicity (since only forward particles are of interest for the shower development); the elasticity[6] and the pion charge-ratio $c = n_{\pi_0}/(n_{\pi_0} + n_{\pi_+} + n_{\pi_-})$, which determines the fraction of particles going into the electromagnetic cascade of the air shower after each interaction. More detailed studies showed that the maximum depth air shower fluctuations, RMS(Xmax), depends mainly on the cross section and less strongly on the elasticity. This makes fluctuations in Xmax a good parameter to study hadronic cross sections at ultra-high energies. The electron number is negatively correlated with the multiplicity, whereas the muon number shows a positive correlation. The electron vs. muon number ratio in air showers are found to be very sensitive to the the secondary particle multiplicity models: in order to increase the muon number in air showers the multiplicity of interactions can be increased, or the charge-ratio decreased. Therefore a good knowledge of particle production multiplicity is also needed to be able to use the muon number in showers for absolute measurements of the mass of the primary particle [71, 72]. The measurement of the forward $\mathrm{dN}_{ch}/\mathrm{d}\eta$ can be therefore valuable to test the validity of the multiplicity models. The TOTEM experiment can perform the precise measurement of the pp cross section, elasticity of the diffractive proton, and multiplicity in the forward region and it is therefore expected to significantly contribute to the improvement on the CR analyses.

2.3 Main TOTEM Results

At the time of writing this thesis, TOTEM has already carried out several important analyses, obtained for pp collisions at 7 TeV. Apart from the $\mathrm{dN}_{ch}/\mathrm{d}\eta$ analysis presented in this document [1], the measurement of the differential elastic cross section in the range $5 \cdot 10^{-3} < t < 2.5$ GeV^2 and the total pp cross section have been performed by using the luminosity provided by the CMS experiment [73, 4, 74]. The results on the elastic scattering cross sections are summarised in fig. 2.20 (left). A compilation of the measurements, obtained with different optics configurations and different RP distances to the beam centre, is reported. In particular the analysis of the elastic scattering at $|t| > 0.36$ GeV^2 [4] was performed with an optics at $\beta^* = 3.5$ m, with the RP detectors edge placed at a distance from the beam axis of 7 time the transverse beam size (σ_{beam}). The results at lower |t| were obtained with a $\beta^* = 90$ m optics, where RP approached the beam down to $10\,\sigma_{beam}$ [73] and $5\,\sigma_{beam}$ [74].

---

[6] The elasticity is defined as $\mathrm{E}_l/\mathrm{E}_{tot}$ with E_l being the energy in the laboratory system carried by the leading particle after the collision and E_{tot} the energy of the projectile in the laboratory system.

The data can be described with a single exponential in the range $5\cdot 10^{-3} < t < 0.2$ GeV^2, with a slope B of 19.89 ± 0.02(stat) ± 0.27(syst) GeV^{-2}. The diffractive peak was found at $t = 0.53 \pm 0.01$(stat) ± 0.01(syst), while the cross section at large t decrease as $t^{-\gamma}$ with $\gamma = 7.8 \pm 0.3$(stat) ± 0.1(syst). The total cross section can be computed using the optical theorem and the luminosity, even without the inelastic rate measurement, by using the following relation:

$$\sigma_{tot}^2 = \frac{16\pi}{1+\rho^2}\frac{1}{L}\frac{dN_{el}}{dt}\bigg|_{t=0} \tag{2.6}$$

The luminosity dependent method for the measurement of σ_{tot} gave $\sigma_{tot} = 98.6 \pm 2.2$ mb[7]. Similarly, by using the elastic rate (properly extrapolated to $t = 0$) and the CMS luminosity the elastic cross section was found to be $\sigma_{el} = 25.4 \pm 1.1$. For all the analyses reported above, the larger systematic uncertainty is given by the CMS luminosity ($\sim$ 4% on σ_{el}, $\sim$ 2% on σ_{tot}).

The luminosity independent cross section measurement has been also performed with a dedicated $\beta^* = 90$ m run and the results will be soon submitted for publication. The TOTEM results, already shown in fig. 1.1, were found to be:

$$\sigma_{tot} = 98.0 \pm 2.5 \quad mb \tag{2.7}$$

$$\sigma_{inel} = 72.9 \pm 1.5 \quad mb \tag{2.8}$$

$$\sigma_{el} = 25.1 \pm 1.1 \quad mb \tag{2.9}$$

The systematic error of the luminosity independent σ_{tot} measurements is related to the elastic measurements for about 1.8 mb, while the uncertainty on the inelastic part contributes for about 1.7 mb. The contribution of the ρ uncertainty is $\sim$ 0.2 mb. The systematic uncertainty on the elastic measurement will be furthermore reduced by using a larger β^* optics. These measurements are consistent with the fits provided by the COMPETE collaboration and, thanks to their small error, they already represent a good constraint for the theoretical models. The inelastic cross section has also been measured by triggering with T2 and by using the CMS luminosity. The T2 visible cross section ($\sigma_{inel,VIS}$) and the cross section for events with at least a charged particle in $|\eta| < 6.5$ ($\sigma_{inel,6.5}$) has been also

---

[7] Notice that the presence of the square in eq. 2.6 reduces the uncertainty contribution that the luminosity has on σ_{tot}

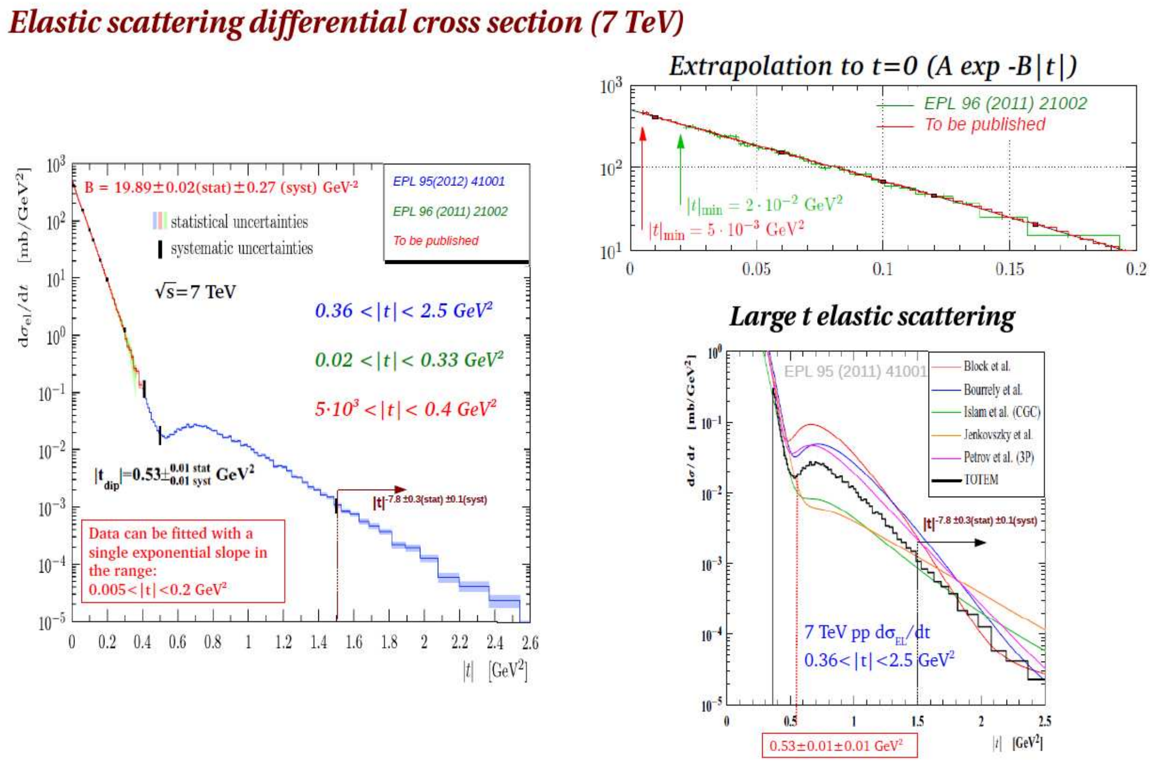

Figure 2.20: TOTEM differential elastic cross section measurement at 7 TeV. The left plot shows a compilation of the measurements performed in the range $5{\cdot}10^{-3} < t < 2.5$ GeV^2. The right part shows a detail of the differential cross sections: the top right picture shows the measurement in the t-range used for the extrapolation; the bottom right picture shows the differential cross section measurement at high t, which is valuable for model discrimination.

estimated including T1. These are found to be:

$$\sigma_{inel,VIS} = 69.73 \pm 2.79 \quad mb \tag{2.10}$$

$$\sigma_{inel,6.5} = 70.53 \pm 2.82 \quad mb \tag{2.11}$$

Apart from the luminosity, the main source of systematic uncertainty which affects the σ_{inel} measurement is given by the correction for the losses of diffractive events at low masses which cannot be triggered. The inelastic cross section for events with all charged particle beyond the T2 acceptance has been estimated with an upper limit of 6.3 mb at 95% confidence level. Other analyses, which are almost completed, concern the single diffractive differential cross section and the measurement of the visible double diffractive cross section.

Chapter 3

T2 simulation and event reconstruction

This chapter describes the offline procedures implemented to simulate and to reconstruct the event in the T2 detector. The TOTEM software [75], based on the CMS framework [76], embeds the necessary interfaces to the GEANT4 [77] simulation toolkit, the description of the material placed between the IP and T2 and the offline software used for the event reconstruction. The description of the T2 detector and the related reconstruction algorithm are also implemented within this framework. The algorithms developed to simulate the signal generated by the T2 planes are presented in sec. 3.2, together with the analysis studies done in order to tune the simulated response with the data (sec. 3.3.1 and 3.3.2). The cluster and hit reconstruction procedures, which allow to measure the particle position in the T2 plane, are presented in sec. 3.3 and 3.5. The description of the tracking algorithm, used to reconstruct the trajectories that particles have through the detector, is reported in sec. 3.6. The evaluation of the tracking algorithm performance is of fundamental importance for any physics analysis performed with T2. The main results on track reconstruction efficiency and resolution are reported in sec. 3.6.4. In sec. 3.7.1 an overview of the main results obtained from the tuning of the GEANT4 simulation on the pp inelastic events (sec. 3.7) is reported. The MC-based analysis, from which the T2 P_T acceptance is evaluated, is described in sec. 3.7.2.

3.1 Naming conventions and reference system

A coordinate system with the origin located at the nominal collision point, the X axis pointing towards the centre of the LHC ring, the Y axis pointing upward (perpendicular to the LHC plane), and the Z axis along the counterclockwise beam direction is used. The R-Φ coordinates are the standard cylindrical coordinates, with Φ measured counterclockwise from the positive X-axis. The four quarters are indicated with the name plus-near (PN), plus-far (PF), minus-near (MN) and minus-far (MF) according to the sign of the Z position where they are installed and according to the side where a quarter is installed with respect to the beam pipe (the near side is the closest one to the LHC centre). The plane numbering, ordered according to their increasing |Z|, ranges from 0 to 9 when only planes of one quarter are shown. To avoid ambiguity, if planes from more than one quarter are shown, they are indicated with [0..9] for PN, [10..19] for PF, [20..29] for MN and [30..39] for MF.

3.2 Digitization model

The main program used to simulate the T2 triple GEM is Garfield [60, 78], a specific computer program for the detailed simulation of gaseus detectors. Other dedicated programs perform specific tasks [60]: a precise definition of the electrostatic configuration inside the detector is obtained interfacing Garfield with Maxwell 2D SV, a finite-elements based software; the simulation of the transport and ionization properties in gas mixtures is done using the Garfield interface to Magboltz, Imonte and HEED. Magboltz solves the Boltzmann transport equations for electrons under the influence of electric and magnetic fields in various gas mixtures; imonte is used to calculate the Townsend and the attachment coefficients for a given gas mixture, while HEED computes the energy loss of fast charged particles or the absorption of photons in gases. These dedicated software tools allow the study of the response of the detector in terms of spatial charge distribution and signal induced on the electrodes. Unfortunately this detailed simulation cannot be used to study the detector response on proton-proton (pp) Monte Carlo (MC) events, since it would take too much CPU-time. Therefore, a proper parametrisation is needed, allowing one to reproduce the detector response on both data and detailed simulation [60]. A geometrical approach has been used in order to create a model reproducing the detailed simulation: the contribution of one ionizing particle (called C) to the charge in the α-th electrode is given by[1] N^{α}:

---

[1] This formula is valid for the pad case, after the charge of the overlapping strips has been subtracted. A similar formula is applied for the strips simulation.

$$
\begin{array}{rcl}
N^{\alpha} & = & \sum_{C} N_{C}^{e^{-}} \cdot G \cdot n^{\alpha}(X_C, Y_C, \sigma_{ch}(Z_C)) \qquad (3.1) \\
\sigma_{ch} & = & \sqrt{Z_C} \times \sigma_0\,, \quad \sigma_0 = \text{gas diffusion coefficient} \qquad (3.2) \\
n^{\alpha}(X_C, Y_C, \sigma_{ch}) & = & \frac{1}{100} \times n(d_{x1}^{\alpha}, d_{x2}^{\alpha}, \sigma_{ch}) \cdot n(d_{y1}^{\alpha}, d_{y2}^{\alpha}, \sigma_{ch}) \qquad (3.3) \\
d_{i1,i=x,y}^{\alpha} & = & \text{Transversal distance between the first ionisation cluster} \\
 & & \text{and the first border of the } \alpha\text{-th pad.} \\
d_{i2,i=x,y}^{\alpha} & = & \text{Transversal distance between the first ionisation cluster} \\
 & & \text{and the second border of the } \alpha\text{-th pad.} \\
n(d_1, d_2, \sigma_{ch}) & = & 50 \times |1 \mp 1 \pm [(1 - erf(\frac{d_1}{\sqrt{2}\sigma_{ch}})) \mp (1 - erf(\frac{d_2}{\sqrt{2}\sigma_{ch}}))]| \\
 & & \text{The upper (bottom) sign is used when the first} \\
 & & \text{ionisation cluster is inside (outside) the } \alpha\text{-th pad.}
\end{array}
$$

Where $N_C^{e^-}$ is the number of primary electrons released in the drift space by the ionizing particle, G is the gain of the triple GEM and $n(d_{y1}^{\alpha}, d_{y2}^{\alpha}, \sigma_{ch})$ is an error function (erf) combination performing the integration in the range of the electrode area of the gaussian cloud generated by one of the primary electrons after the amplification. Notice that the integral depends on the X_C, Y_C, Z_C position of the primary electron (Z_C is the electron distance with respect to the RO board). Only the electrodes with a collected charge N^{α} larger than an "equivalent VFAT threshold" are set as active. After taking into account some particular electrostatic effects which give a larger effective width to the strips (see fig. 3.1), it has been found that this simple model reproduces well the detailed simulation. More details about the tuning of the parameters used in the digitization is given in sec. 3.3.1.

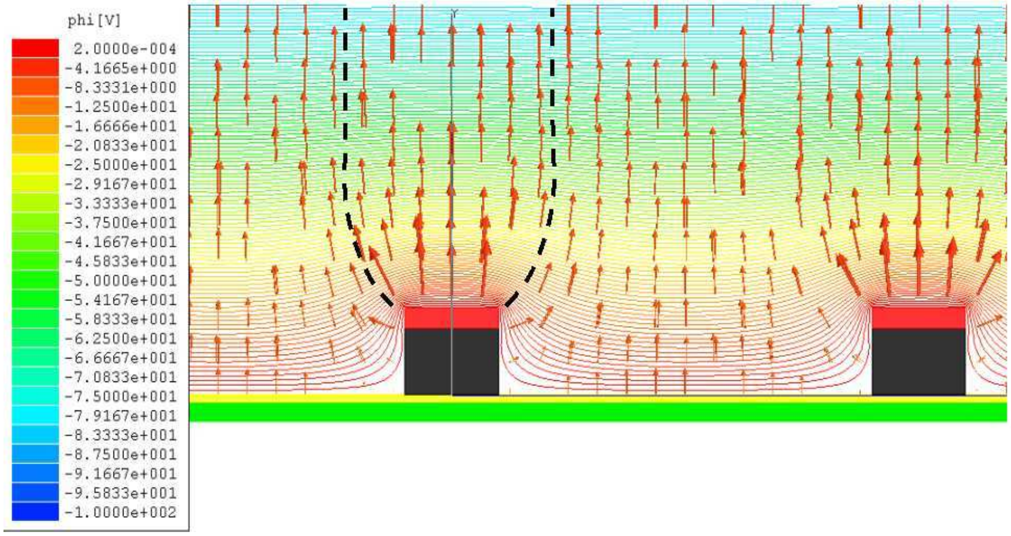

Figure 3.1: Electrical field lines and equipotential curves in proximity of a strip [60].

3.3 Cluster reconstruction

The purpose of the clustering algorithm is to opportunely group the neighbouring pads or strips fired by the same charged particle in a particular plane. Pad and strip clusters are considered independently. Data from Pb-Pb collisions, taken in 2010, have been used to better understand the expected shape of the pad-cluster. Indeed the Pb-Pb cross section is dominated by electromagnetic processes [79] with most of the T2-triggered events with one muon or electron in T2. This very clean sample of single track events has been utilized to make studies on the cluster topology.

It has been found that less than 2% of the pad clusters are made by a set of pads where at least one pad is touching the neighbouring ones only with its corner. This fraction can be explained in terms of clusters which originally were touching only by edges but are affected by pad inefficiencies, noisy pads which randomly touch the physical cluster and a small contamination from δ-ray production. Therefore we assume that a pad cluster associated to a single particle is made by pads touching by an edge, while the clustering algorithm recognizes pads touching only by a corner as associated to different particles.

From commissioning studies (see sec. 3.3.1) it is known that for low multiplicity events the pad clusters size associated to a primary track is smaller than 5 in more than 99% of the cases. In real pp events however primary and secondary signals can overlap on closer pads. The pad cluster shape can also be distorted by noise effects, as shown for example in fig. 3.2 where the green pad cluster seems to be made by 3 pad clusters joined by a column of noisy pads. Since the Front End electronics is not able to measure the charge collected by the pads, the pad cluster $R{-}\Phi$ position is evaluated according to the geometrical properties of the cluster: for large cluster size (≥ 5) the weighted average of the $R-\Phi$ projections are used as the best estimation of the cluster position[2], while the position error is taken as the RMS of these distributions. For smaller pad clusters a faster algorithm is used which calculates the cluster $R-\Phi$ position considering only the $R-\Phi$ widths of the cluster: the centre is therefore calculated as the mid-point of the unweighted $R-\Phi$ projections, and the associated error is half of the projection size. A new feature of the clustering algorithm has been developed and it is planned to be used in future studies, which allows to partially recuperate clusters affected by noise, as the one shown in fig. 3.2: the cluster projections in the row-direction and in the column-direction are computed. The pads which contribute less than a programmable fraction to the projection are removed from the initial cluster: if the cluster breaks in more pieces, the new fragments become new independent clusters.

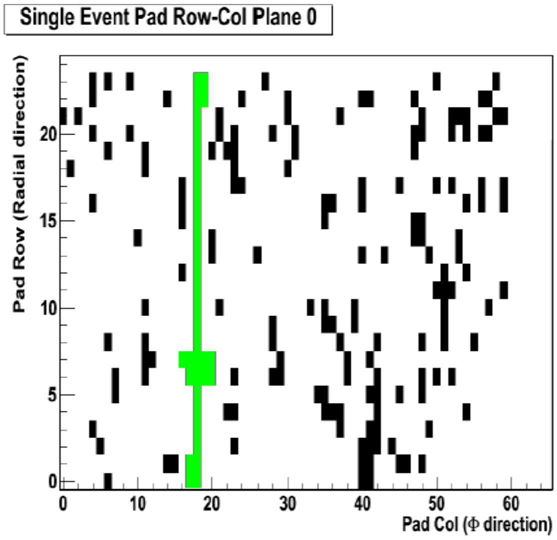

Figure 3.2: Active pads for one of the T2 planes in a very high multiplicity event (88 pad clusters in the plus near quarter). In green, a big cluster affected by noise is shown.

For the strip clustering strategy, there is instead no need of any topological study: only neighbouring strips of the same strip-column are grouped. The $R{-}\Phi$ position is calculated as the simple average of the channels radial coordinates and the Φ coordinate of the centre of the strip, respectively. The error on the radial direction is given by $\Delta R/\sqrt{12}$ where ΔR is the strip pitch (400 μm).

---

[2] For example, a projection along the ϕ direction is obtained integrating (counting) for each column the pads of the cluster.

3.3.1 Measurement and tuning of the cluster size

In order to tune the digitization model with the data, some of the free parameters introduced in sec. 3.2 have to be evaluated. The two main parameters that were found to be effective for the digitization tuning are: the effective strip width (ESW) and the equivalent chip-threshold (Eq-Thr). The former is needed for the tuning of the strip cluster size, the latter has been introduced in order to properly reproduce the cluster reconstruction efficiency of each RO chip, as measured from data.

Single particle event simulation has been utilized in order to convert the chip cluster reconstruction efficiency measured on data in an equivalent threshold of the chip to be applied in the simulation. Fig. 3.3 shows the cluster reconstruction efficiency in simulation as a function of the effective chip threshold utilized by the digitization. Once the cluster efficiency of the chip (ϵ) is measured in the data, as explained in sec. 3.3.2, a data efficiency file is created and taken as an input from the digitization: the equivalent threshold to be applied in the chip simulation is then calculated by inverting the Gaussian parameters C, μ, σ of the fit curve of fig. 3.3:

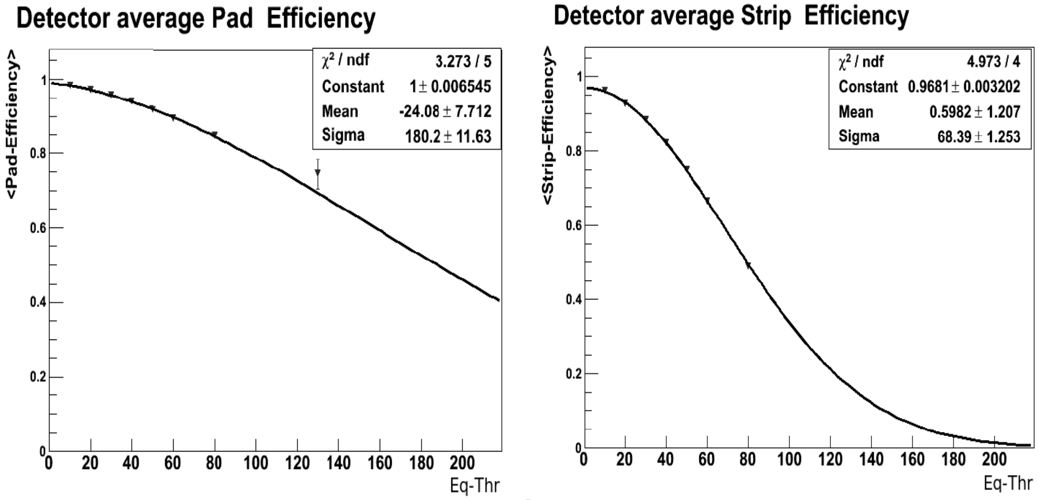

Figure 3.3: Simulated cluster reconstruction efficiency as a function of the effective chip threshold for pad cluster (left) and strip cluster (right).

$$\text{Eq-Thr} = \mu + \sigma * (-2ln(\epsilon/C)) \tag{3.4}$$

The concept of the Eq-Thr allows one to maintain the properties for which the bigger the charge in the electrode, the larger the probability to switch it ON. The curves in fig. 3.3 have been obtained using a plane strip gain and pad gain of 30K and 15K respectively. It is worth to remind that in principle a single gain value should work both for strip and pad, and its value should be determined only according to the HV value applied to the foils. However, since the cluster efficiency is directly measured on data, the foil gain acts as a free parameter rather than a predictive parameter. In addition, measurements performed in tests with cosmic rays have also shown that the same HV applied in different chambers doesn't necessarily produces the same collected signal. An effective gas drift coefficient $\sigma_0 = 0.34$ mm cm$^{-1/2}$ (the nominal one for ArCO$_2$ with a longitudinal electric field in the range of 3-4 kV/cm should be 0.25-0.26 mm cm$^{-1/2}$) has been used. The use of an effective gas coefficient is necessary in order to obtain a high strip efficiency without enlarging too much the strip cluster size. The precise value of σ_0 has been decided according to the best tuning of the strip cluster size, while the reduction of the pad gain with respect to the strip one was found necessary in order to obtain a better matching of the pad cluster size, which is instead quite stable for small variation of σ_0. Using $\sigma_0 = 0.34$ it is possible to reach a good tuning of the strip cluster size by an optimisation of the effective strip width (ESW). The ESW parameter is defined as half of the transverse length to be added to the nominal strip width in order to obtain the transverse size of the electron cloud which is focused on the strip. Fig. 3.4 shows the relative population of the cumulative strip cluster size obtained in pp minimum bias simulation as a function of the ESW parameter. In particular, the fractions of clusters with size 1, 2, 3 are shown. From this figure the best value of the ESW parameter is determined as the one for which the difference between the relative cluster size populations shown in the figure and the ones obtained from the data, is minimal. The value of the ESW parameter which minimises the difference between data and MC in the strip cluster size distribution is ESW $= 0.036$ mm, where only clusters with sizes ≤ 3 have been considered. A comparison of the strip and pad cluster sizes obtained with pp low luminosity data and a MC simulation after the digitization tuning is shown in fig. 3.5.

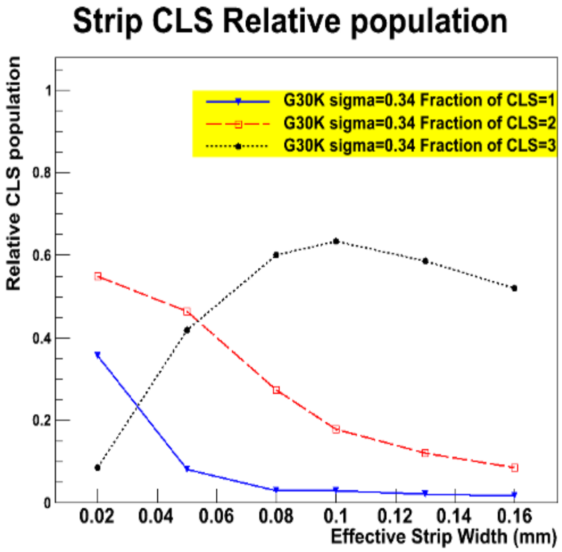

Figure 3.4: Tuning of the strip cluster size as a function of the ESW parameter. Blue, Red and Black curves represents the fraction of strip cluster with size equal to 1,2,3 respectively.

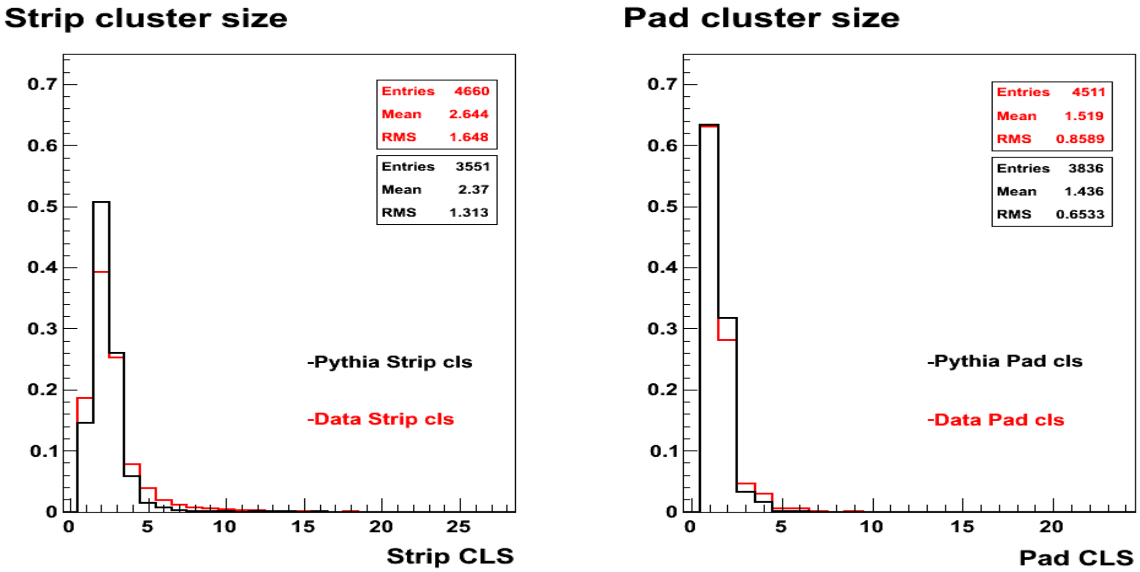

Figure 3.5: Comparison of data (red curve) and MC (black curve) cluster size. Left: strip cluster size; right: pad cluster size. All the clusters reconstructed in the PN quarter have been included.

3.3.2 Measurement and tuning of the cluster reconstruction efficiency

The cluster reconstruction efficiency reported in this section has been measured on the same *pp* data sample used for this thesis analysis. The cluster reconstruction efficiency is calculated for strip and pad clusters separately and for each VFAT chip of the T2 detector. This is because the efficiency is mainly driven by problems due to the front-end electronics, rather than by an inhomogeneous signal formation and collection by the triple GEM detectors. The limitation of this strategy is that the cluster reconstruction efficiency is averaged over the 128 (strip) or 120 (pad) VFAT channels. Therefore a localised inefficiency, affecting only a limited geometrical region covered by the channels of a chip, cannot be correctly measured on data and reproduced in the simulation. This is the case for the regions at the edges of the T2 planes (like part of the overlapping region), which are not included in the cluster efficiency calculation.

This analysis should be repeated for each new data sample utilized for Physics studies. Indeed, even if the GEM planes themselves have been found to be very stable in their performance, recalibration of the chip latencies and thresholds is sometime needed between different runs. Moreover the probability that the data frame sent by the VFAT is corrupted can change with time with a consequent variation of the cluster reconstruction efficiency.

In this analysis only events having a low average pad cluster multiplicity (≤ 5 pad clusters per plane) are selected. This allows the tracking algorithm (see sec. 3.6) to produce a sample of high quality tracks, avoiding ambiguity due to close clusters produced by different particles. Tracks are reconstructed excluding the plane under test, and only tracks with $\chi^2/N < 2$ and $|\eta| > 5$ are kept for the analysis. The efficiency is calculated requiring for the pad cluster to be reconstructed within $3\sigma_{X,Y}$ from the extrapolated track position and for the strip to be in the same column of the strip cluster forming the track and within $3\sigma_R$ from the expected position. The correctness of the procedure and of the requirements have also been checked by comparing the output of the algorithm with the one expected from an event display analysis. The cluster reconstruction efficiency of each VFAT is saved in a text file; this file is an input for the digitization algorithm which converts the data efficiency to the equivalent threshold, as described in 3.3.1. The results of the measured VFAT efficiencies on data are shown in fig. 3.6. The averaged strip and pad cluster efficiency per plane are shown in fig. 3.7 for both data and tuned simulation. The measurement has been repeated also selecting events with an average pad cluster multiplicity (APCM) of $5 <$ APCM < 10 and $10 <$ APCM < 15. The results were found to be stable within 1-2%. Excluding planes where one or more chips are not sending data, and planes where a sector in the GEM foil is short-circuited (see for example the plane 1 in Fig. 3.6) the average pad cluster reconstruction efficiency is between 90% and 100%, while the strip cluster reconstruction efficiency is between 85% and 95%.

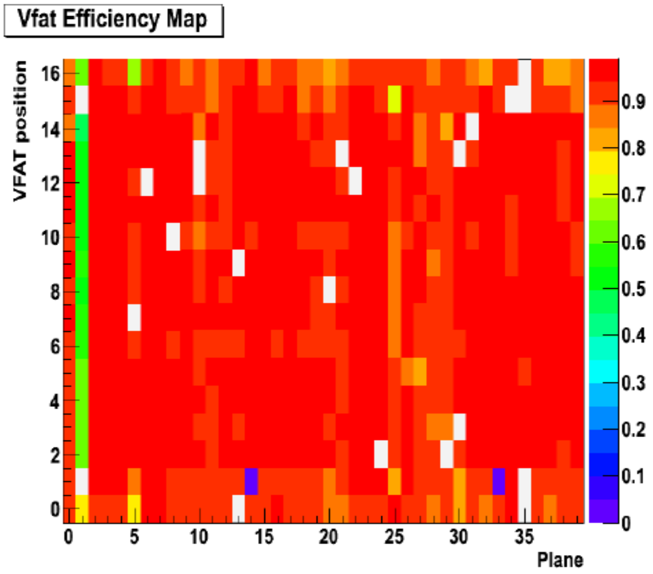

Figure 3.6: Average cluster reconstruction efficiency per VFAT. The X axis shows the detector number (see sec. 3.1). The Y axis shows the VFAT chip number: [2..14] are for the VFATs reading the pad channels, while numbers 0,1,15 and 16 are for the VFATs associated to the strips.

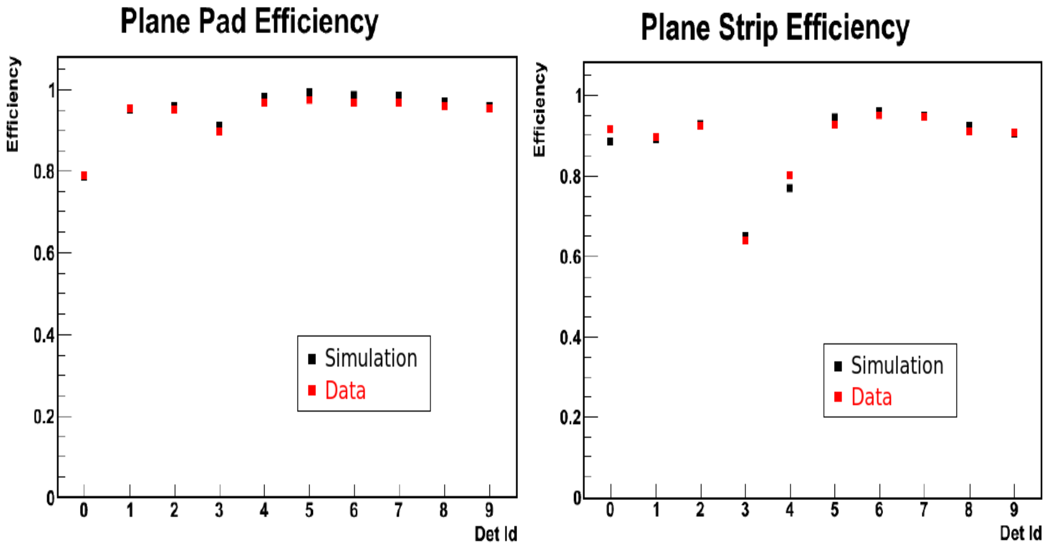

Figure 3.7: Average reconstruction efficiency for pad clusters (left) and strip clusters (right) as a function of the detector plane, for the PF quarter. Red and black points show, respectively, the measurements performed on the LHC pp data and on MC pp inelastic events with the tuned simulation.

3.4 Noisy and dead channels

Offline algorithms have been developed in order to quickly determine for each run the noisy and the dead channels of each of the T2 planes. To evaluate if a channel is noisy the algorithm compares the number of times when the selected channel is ON to the average value of the counts obtained from the corresponding channel in all the other planes. If the count obtained by the channel under study is larger than 50% of the average value, the channel is declared as noisy. Dead channels are instead selected as the ones with a number of entries smaller than the 30% of the average value. The position of the noisy channels and of the dead channels are saved in a file to be used for the data simulation and reconstruction, where they are set "OFF". In the 2011 data taking the fraction of noisy channels was found to be lower than 2%. The same fraction has been measured also for the dead channels[3]. The histogram of the number of noisy channels and dead channels per VFAT, as a function of the plane, is reported in fig. 3.8.

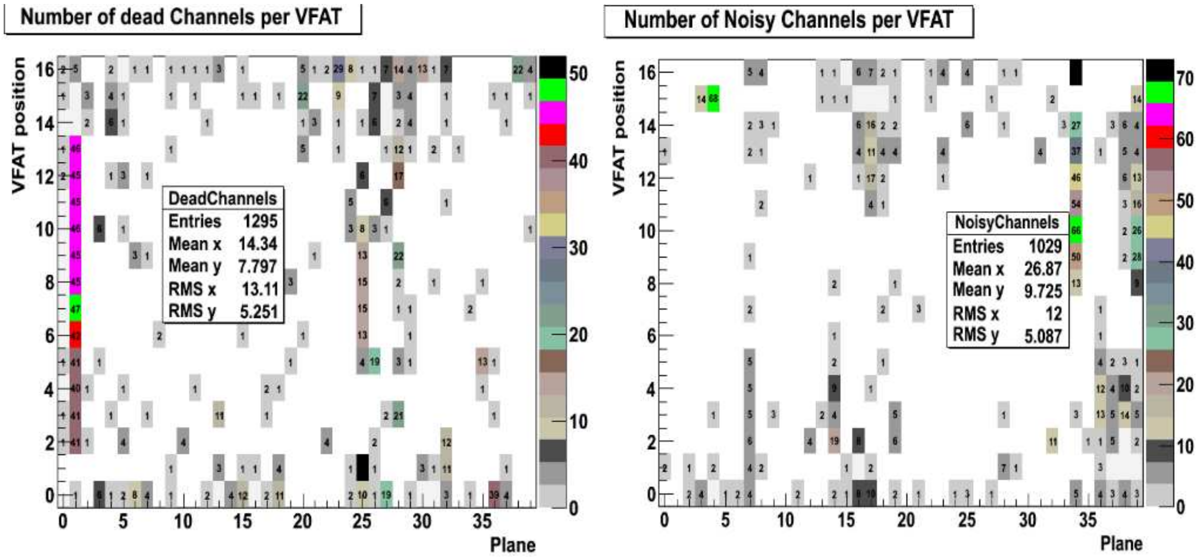

Figure 3.8: Number of dead channels (left) and noisy channels (right) per VFAT, measured in the 2011 data sample.

3.5 Hit reconstruction

The purpose of the hit reconstruction is to optimally combine the position information from the pad cluster and the strip cluster associated to the same particle. In the following the hits are classified as "class-1,-2,-3" hits according to their content in term of clusters. A class-1 hit is made by an overlap between a strip cluster and a pad cluster. Therefore the best radial coordinate is given by the strip cluster, while the azimuthal coordinate is taken from the pad cluster. A class-2 and a class-3 hit is respectively made by a pad cluster

---

[3] This fraction is calculated only taking into account channels from active VFATs.

or a strip cluster only, because a strip or pad cluster overlap is not present in this case. If a pad cluster has N strip clusters which overlap its area, then N class-1 hits are created. "Ghost hits" can therefore be created at this stage due to particles which fire the same pad-row but different pad-columns on the same detector plane. This kind of ambiguity can be resolved only at the track level. The resolution of the reconstructed hit has already been measured during the T2 commissioning activity with cosmic-ray [58]. The hit resolution measurements have also been repeated on pp collision data, where the correction for detector misalignment is applied during the event reconstruction. The radial class-1 hit residuals for low multiplicity events, obtained using primary track candidates, are shown on the left side of fig. 3.9 for data and simulation. The residual is defined as the difference between the hit reconstructed position and its expected position according to the track extrapolation. The track are reconstructed without including the plane under test and the primary tracks are selected according to the $|\text{ZImpact}| < 5$ m[4] condition. The RMS of the two distributions are compatible with a class-1 hit radial resolution of about $100\ \mu$m[5]. The resolution of the Φ coordinate cannot be obtained with the same track-residual analysis. Indeed, primary tracks are characterised by having in most of the planes the same row and column of the active pads, because of the smaller charge sharing between the pads with respect to the strip case (see for example the cluster size result reported in section 3.3.1). To avoid an underestimation of the azimuthal resolution this quantity has been obtained from MC studies, looking at the difference between the GEANT hit azimuthal position of the particle and the hit reconstructed azimuthal coordinate. With this method a resolution better than 1° is measured, as shown in fig. 3.9 (right).

---

[4] See 3.6 for the ZImpact parameter definition.

[5] The standard deviation of the residual distribution is actually an overestimation of the hit resolution because both the hit resolution and the error affecting the track parameters (and therefore the predicted point) contribute to its width. The uncertainty on the track prediction is expected to contribute to the residual width for about 20%.

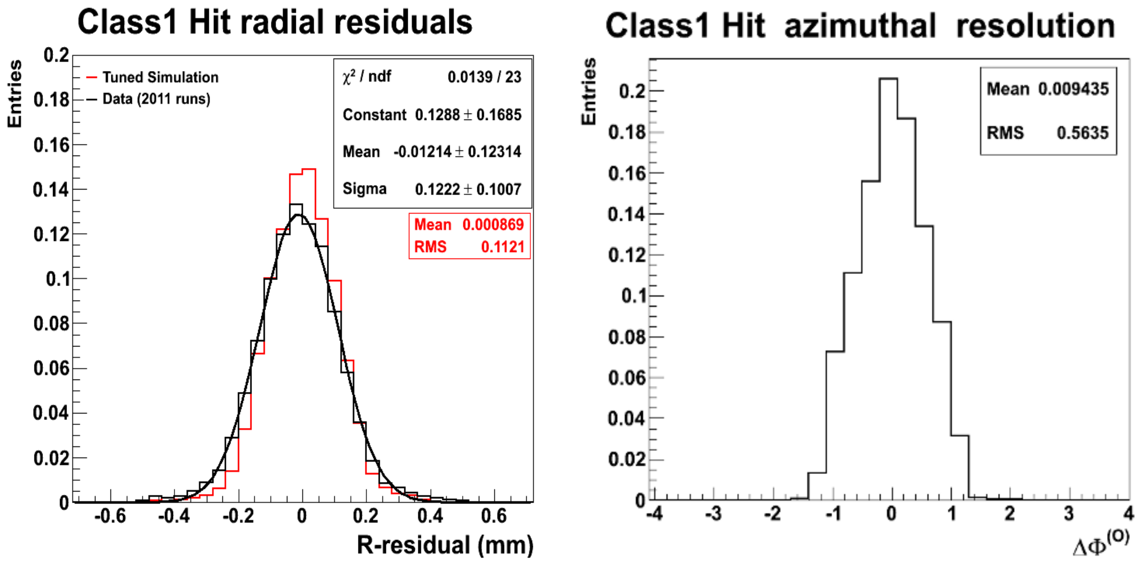

Figure 3.9: Left: radial class-1 hit residuals, with the comparison between the 2011 data (black curve) and the tuned simulation (red curve). Right: azimuthal class-1 hit resolution, calculated with a MC method. The measurements have been performed with hits reconstructed in a central plane of the PN quarter.

3.6 Tracking algorithm

The track reconstruction is based on a Kalman filter algorithm [80] that is simplified due to the small amount of material traversed by the particle crossing the 10 GEM planes ($\sim 0.05X_0$ [60]) and to the low local magnetic field in the T2 region. The particle trajectory can, therefore, be successfully reconstructed using a straight line. As a consequence, the particle momentum cannot be reconstructed. The tracking algorithm described in this section has been developed in order to increase the track reconstruction efficiency, respect to the one obtained with the simpler algorithm described in [62]. The needs of a better algorithm became evident as soon as the large impact that secondary particles have on the worsening of the tracking performance was established by the simulation. Fig. 3.10 shows a simulated high multiplicty event-display, where interactions with the material produce a large amount of reconstructed tracks in T2.

The track finding algorithm is implemented in three steps, described in more details in the next sections:

- *Road finding (sec. 3.6.1):* by using the pad clusters, the algorithm looks for 3D collinear clusters (pad roads) through the 10 planes of each quarter. The algorithm is inspired to the Kalman Filter technique, where the multiple scattering sources have

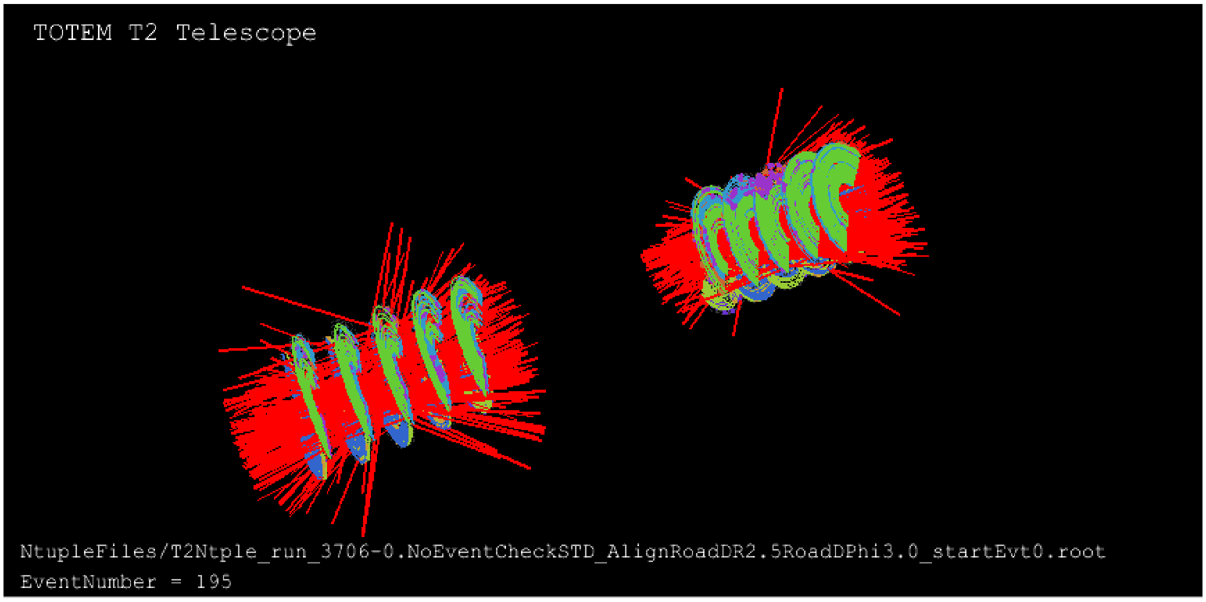

Figure 3.10: Event-display of a high multiplicity event in T2, with more than 100 reconstructed tracks per side.

been assumed to be negligible.

- *Track finding (sec. 3.6.2):* for each pad road, the overlapping strip clusters are associated to each pad cluster and all the possible combinations among the strip and the pad clusters are generated.
- *Track fitting (sec. 3.6.3):* the hits associated to each track are fitted, proper geometrical and quality track parameters are computed.

3.6.1 Road finding

The reconstructed pad cluster positions are the basic quantities used by the road finding algorithm. A road is defined as the set of pad clusters associated to the crossing particle. Pad clusters are preferred with respect to the strip clusters since they have smaller occupancy, smaller noise and higher efficiency. Moreover, each pad cluster provides at the same time, with a reasonable resolution, the X,Y and Z position of the crossing particle. The road finding algorithm processes each quarter independently and it is inspired to a seedless Kalman filter technique, where the multiple scattering sources are assumed to be negligible. The algorithm has been designed to reconstruct the primary tracks with a high efficiency[6]. Therefore MC studies have been preliminarily done to understand the pattern that pad clusters associated to a primary particle would have. It has been found that pions associated to 7 TeV inelastic events generally show a very clean pattern, easy to be identified at least when the event is not affected by a large production of secondary particles. Indeed, a large fraction of pion roads appears as a set of pads mostly with the same row and column coordinates or which differ by one only. This feature is used by the algorithm during the road construction.

Starting from the closest plane to the IP, each cluster with a size smaller than CLS_{seed} ($\text{CLS}_{seed} = 5$ by default) is associated to a cluster in the neighbouring forward plane. These pairs, hereafter called segments, constitute the seeds of the algorithm, i.e. the sample of the starting trajectories. In this sense the algorithm is seedless, i.e. it does not need a dedicated seed algorithm for its starting[7]. For each plane, starting from the second one, the algorithm repeats the following steps:

1. Propagate the segments along a 3D straight line in the forward direction from plane i to plane i+1. A searching window is defined according to the segment precision and a list of compatible hits of the plane i+1 is associated to the segment. In particular, each time that the algorithm searches for new pad clusters to be associated to the segment, the error on the point predicted by the segment propagation is evaluated according to a straight line fit of the pad clusters already composing the segment. The hits of the plane under investigation are associated to the segment if:

$$|m_{i+1} - p_{i+1}| \; < \; N_\sigma \sqrt{\sigma_p^2 + \sigma_m^2} \tag{3.5}$$

   where m_{i+1} and p_{i+1} represent, respectively, the measured hit position in the plane i+1 and the related prediction from the segment propagation, σ_p and σ_m are the associated uncertainties and N_σ is an input parameter of the algorithm ($N_\sigma = 2$ in the default setting). The condition needs to be satisfied in both the XZ and YZ planes. If more than one pad cluster fulfils the condition 3.5, two possible solutions have been programmed: either only the pad cluster which gives the minimum χ^2 of the segment fit is taken (default setting, see sec. 3.6.3 for more detail on the χ^2), or concurrent branches are created. In this latter case, the segment is split in two independent

---

[6] In this chapter a primary particle is defined as a charged particle produced at the IP which arrives in T2 without having any interaction with the material, except multiple scattering.

[7] When the average pad cluster multiplicity per quarter is larger than 10, a preliminary step is performed before the starting of the seedless algorithm. Clusters having the same rows and columns are grouped into a segment. This ensures a higher efficiency in the primary track finding. These segments are then processed by the road finding algorithm in the standard way described in the text.

segments and only when the algorithm will process the last plane, the branch having more pad clusters or, in case of equality, a better χ^2, is kept. To include with a high efficiency the primary clusters to the segment, if the difference in the pad-row or a pad-column between a pad cluster in the searching plane and the closest cluster in Z in the segment is 1, then the cluster is associated.

2. Decide if the segment can propagate: if the pad in the segment which is closest to the plane i+1 is however more distant than $N_{Empty\,plane}$ planes and if there is no cluster that can be associated to the segment in the plane under investigation, then the segment propagation is stopped. $N_{Empty\,plane}$ is an input parameter of the algorithm. This condition has been introduced since, from efficiency studies, it is known that a particle has a negligible probability to have 3 consecutive pad clusters OFF, therefore $N_{Empty\,plane} = 2$ in the default settings of the algorithm. This check allows to reduce the CPU time and, especially in high multiplicity events, to reduce the probability to include in the segment clusters generated by a different particle.

3. New segments are created from plane i+1 to the next plane, using as starting point only pad clusters not already included in any of the propagating segments. Only pad clusters with a low cluster size (by default less than 5) are used to create a new starting point of the segment. Large cluster sizes (> 5) are still used in point 1 and 2, in order to not kill the segment too early, especially in high multiplicity events where a merging of clusters is more likely. A backward propagation is also provided, which guarantees the inclusion of unassociated pad clusters in some critical cases. As an example, if a quarter has the second plane completely OFF, the first plane would not contribute to any segment if a backward propagation procedure would not be provided.

When also the last plane has been processed, only segments with at least 4 pad clusters are kept as road candidates and are then processed by the track finding algorithm.

3.6.2 Track finding

For each pad cluster of a road, the track finding algorithm searches the overlapping strip clusters. Especially for pad clusters at large R and in high multiplicity events, a pad cluster can overlap with more than one strip cluster. All the class-1 hits which are compatible with the road are found and the best combination, in terms of a minimum χ^2 criteria, is determined. If none of the combinations has enough large χ^2 probability (by default

$\chi^2 - p_{min} = 0.01$) the sample of class-1 hits is stripped of the outermost hit giving the largest contribution to the χ^2. The set of the found hits, constitutes a first track. Simulation studies have shown that a minimum of 4 pad clusters (from the road) with at least 3 overimposed strip clusters can be required as a quality criteria of the tracks. With the remaining hits compatible with the road all the combinations are again generated as described above and eventually new remaining tracks are created. When the track candidates are found, the algorithm looks for class-3 hits (strip clusters) which are not yet associated to the tracks. For each plane where tracks have no hit, the most compatible strip cluster is associated, using again the condition reported in eq. 3.5 this time evaluated for the radial direction only. A ghost track suppression procedure has been implemented in order to identify and remove the non physical tracks. These can be generated when the strip clusters join two different roads having their pad clusters with the same row coordinates. To avoid double counting of tracks the pair of roads with the same pad row coordinates are selected; if more than one track per road is reconstructed, only the one with the highest number of hits or, in case of equality, with the best χ^2 is maintained.

The most important input parameters of the road and track finding algorithms, together with their default values, are summarised in table 3.1.

Table 3.1: The most important setting parameters for the road and track finding algorithms, with their default values.

1. Maximum seed cluster size (CLS$_{seed}$)	5
2. Implementation of concurrent branches	false
3. Road minimum number of cluster pads	4
4. Minimum number of class-1 hits	3
5. Maximum polar angle of the segment	$\pi/2$ rad
6. N_σ	2
7. $N_{Empty\,plane}$	2
8. Minimum $\chi^2 - P$ for outlier rejections ($\chi^2 - P_{min}$)	0.01
9. Ghost tracks suppression	true

3.6.3 Track fitting

The track can be fitted with a linear function in the coordinates X, Y, Z. Therefore a least squared method has been implemented, where the following χ^2 function has to be minimised:

$$\chi^2 = (\mathbf{m} - \mathbf{A}\hat{\theta})^T V_m^{-1} (\mathbf{m} - \mathbf{A}\hat{\theta}) \tag{3.6}$$

where $\mathbf{m}$ is the vector of the n hit measurements (x_1,y_1,...x_n,y_n) composing the track, $\mathbf{A}$ is the 2nx4 matrix describing the linear model, and $\hat{\theta}$ are the track parameters (b_x,tanθ_X,b_y,tanθ_Y) i.e. the intercept and the slope of the track in the XZ plane (b_x,tanθ_X) and in the YZ plane (b_y,tanθ_Y). V_m is the covariance matrix of the measurements which is a block diagonal matrix. Indeed, only the R and Φ coordinates of the hits composing the T2 tracks are independent. The X and Y coordinates are correlated, and the covariance matrix for the i^{th} hit is obtained as:

$$\mathbf{V_{m,i}} \;=\; \mathbf{S}\,\mathbf{D_{m,i}}\,\mathbf{S^T} \tag{3.7}$$

where S is the Jacobian matrix for the transformation from cylindrical (R, Φ, Z) coordinates to the Cartesian (X, Y, Z) coordinates and D is the diagonal covariance matrix of the hit position in the cylindrical coordinates. The track parameters $\hat{\theta}$ and the associated covariance matrix $\mathbf{V}_{\hat{\theta}}$ are obtained with the standard relations [81]:

$$\hat{\theta} \;=\; (\mathbf{A^T}\,\mathbf{V_y^{-1}}\,\mathbf{A})^{-1}\,\mathbf{A^T}\,\mathbf{V_y^{-1}}\,\mathbf{m} \qquad \mathbf{V}_{\hat{\theta}} = (\mathbf{A^T}\,\mathbf{V_y^{-1}}\,\mathbf{A})^{-1} \tag{3.8}$$

Apart from these basic parameters, additional parameters of the track which are useful for the physics analysis, have to be evaluated. The list of the parameters associated to a reconstructed track is:

- $\hat{\theta}$, $\mathbf{V}_{\hat{\theta}}$: the output of the fit described above.
- θ_X, θ_Y: atan(a_x), atan(a_y), where a_x, a_y are the slopes of the tracks in the XZ and YZ plane, found by the fitting procedure described in the text.
- θ_R: the polar angle of the track: $\theta_R = \sqrt{\theta_X^2 + \theta_Y^2}$.
- η: -ln (tan $\frac{\theta_R}{2}$).
- Φ: atan(a_y/a_x).
- η_{RZ}: the η parameter calculated with a polar angle obtained using a linear fit in the RZ plane.
- Φ_{RZ}: the weighted average of the ϕ coordinates of the hits composing the track.
- η_{IMP}: average pseudorapidity of the T2 track hits, calculated from the angle that each hit has with respect to the IP.
- Z_{min}: the Z value at the position of the minimum approach of the track to the Z axis.

- R_{min}: the distance between the track and the Z axis.

- R_0: the R coordinate of the intersection point between the track and the XY plane.

- ZImpact: the Z coordinate of the intersection point between the track and a plane ("π_2") containing the Z axis and orthogonal to the plane defined by the Z axis and the track entry point in T2 ("π_1"). An explanation of this parameter is also sketched in fig. 3.11. The ZImpact parameter has been found to be more stable with respect to the misalignment biases described in ch. 4. The construction of the plane π_1 and π_2 has been done in order to guarantee the same resolution of the ZImpact parameter as a function of Φ.

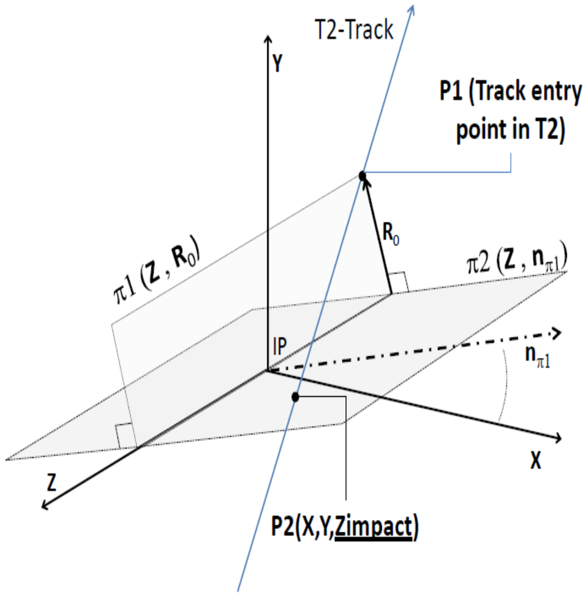

Figure 3.11: Definition of the track ZImpact parameter. The description is discussed in the text.

- The error on the geometrical parameters described above.

- χ^2 and $\chi^2 - p$: the value of the χ^2 function defined in eq. 3.6 when evaluated with the solution $\hat{\theta}$, and the corresponding P-value of the hypothesis test.

3.6.4 Tracking performance

This section reports the main results on the performance of the T2 tracker. The MC results reported here are intended for the simulation tuned with the 2011 data. This tuning also includes the misalignment configuration measured in the 2011 data, reported in ch. 4. The simulation of pp inelastic events is obtained with the Pythia 8.108 MC, at a CM energy of 7 TeV.

3.6.4.1 Tracking efficiency

The track reconstruction efficiency has been evaluated with a MC analysis. Only the results on the primary track efficiency will be reported, which is the relevant quantity to be estimated for the Physics analysis. Two types of primary tracking efficiency need to be defined: the "inclusive" tracking efficiency (ε_i) and the "analysis-oriented" tracking efficiency (ε_a). ε_i is the probability to reconstruct a primary GEANT track with $P_T > 40$ MeV/c, when the track crossing the T2 detector provides at least 4 points. The GEANT track is considered reconstructed if at least 3 GEANT hits of the simulated track are found to overlap the pad clusters of the reconstructed track. The cut in P_T is used since the efficiency measurement has to refer to particles in the nominal P_T acceptance of T2 (see sec. 3.7.2). ε_a is defined as ε_i, but requiring a reconstructed track with $|\text{ZImpact}| < 5$ m and a $|Z_{min}| < 13.5$ m. Indeed, a cut on these two variables has been used in the data analysis in order to separate the primary from the secondary tracks (see ch. 5). The values of the $|Z_{min}|$ and $|\text{ZImpact}|$ cuts reported above are therefore chosen in order to have a primary track selection which is compatible to the one used in the data[8]. In order to estimate the efficiency of selecting the primary tracks, ε_a is therefore the relevant quantity. For each arm of the T2 telescope, the measurements of ε_i and ε_a are reported in fig. 3.12 as a function of the GEANT primary track multiplicity in the T2 arm.

ε_i has been found to be $> 98\%$ in the whole range of the T2-primary multiplicity. ε_a has been found to decrease with the primary track multiplicity, from ~90% to ~80%. The lower value of ε_a with respect to ε_i can be explained because of the reduced probability that lower energy tracks (more subject to magnetic field deflections and multiple scattering effects) have to fulfil the requirement on the ZImpact and Z_{min} cuts (see sec. 3.7.1). Moreover, as suggested by the more marked dependence on the track multiplicity that fig. 3.12-right has with respect to fig. 3.12-left, the higher the multiplicity, the lower the capability of the

---

[8] Actually the cuts used in the data analysis are chosen according to the track η. The cuts shown above allow to select the same fraction of primaries as the one selected in the data analysis if the tracks are considered in the full pseudorapidity range $5.3 < |\eta| < 6.4$.

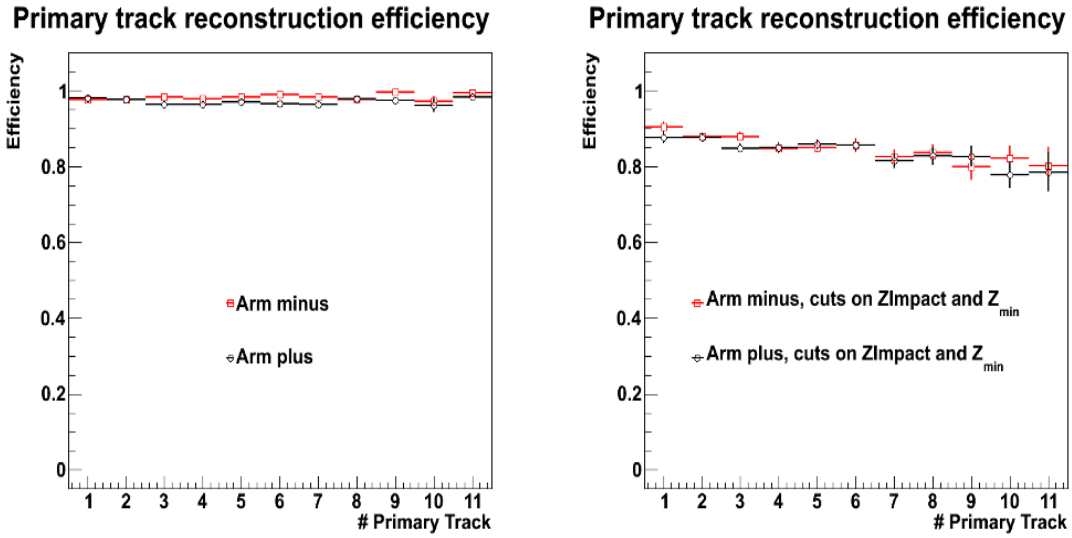

Figure 3.12: Primary track reconstruction efficiency as a function of the GEANT primary track multiplicity in the T2 arm. In the left (right) picture, the measurement of ε_i (ε_a) has been reported, separately for the minus arm (red circles) and the plus arm (black squares).

algorithm to properly reconstruct the primary tracks. A higher occupancy constributes to a worse track reconstruction because a lower number of primary clusters useful for the track reconstruction is available (some of the clusters can be covered by the signal of the secondaries so enlarging their size). Moreover a higher occupancy increases the probability to misidentify the pattern of a primary track.

The primary track efficiency ε_a has been also evaluated as a function of the average pad cluster multiplicity per quarter (hereafter APM). The following justifies the use of the APM as an independent variable for the ε_a measurement:

- As explained above, the primary track efficiency is expected to have a strong dependence on the APM.
- To correct more precisely the data for the primary track efficiency, a variable that can be measured on both MC and data is needed. APM is a good estimator for the number of particles traversing T2 for both MC and data. The data efficiency correction can therefore be implemented by measuring the event APM and looking to the MC for the corresponding primary efficiency. This strategy minimises the dependence on the data correction from the tuning of the MC multiplicity.

For the needs of the analysis presented in chapter 5, ε_a has been also studied as a function of the pseudorapidity. For each pseudorapidity interval of size 0.05 in the T2 acceptance, ε_a has been evaluated as a function of the APM for each quarter independently. As a reference, one of these curves is reported in fig. 3.13 for reconstructed tracks in the bin centred at $\eta = 6.175$ and width $\Delta\eta = 0.05$. Being the APM measured on data $\sim$22, the average ε_a is above $\sim$80% for 7 TeV pp inelastic events. A dependence of ε_a from η has also been found: as an example, for PN, $78\% < \int_{APM} \varepsilon_a < 84\%$ with larger efficiency at larger η.

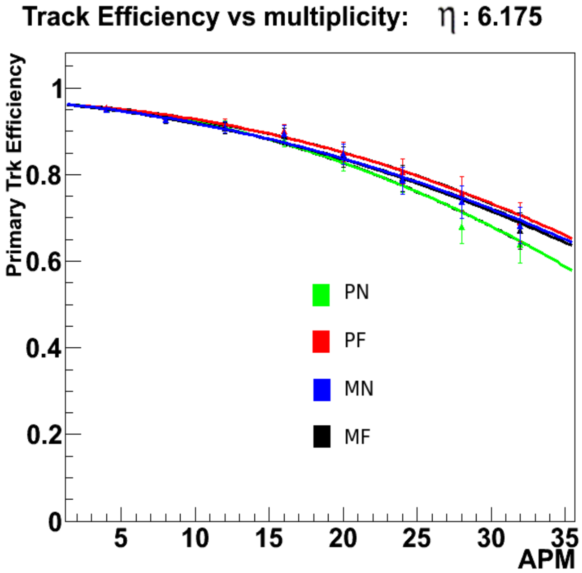

Figure 3.13: Primary track efficiency as a function of the APM of the quarter. The results are shown for the 4 quarters and refer to GEANT primary tracks with $6.15 < |\eta| < 6.2$.

3.6.4.2 Tracking pseudorapidity resolution

The pseudorapidity residual with respect to the generator ($\Delta\eta_{gen}$) is defined as the difference between the primary charged particle η at the IP (η_G) and the associated reconstructed track η (η_R). The particle pseudorapidity resolution (σ_{η_G}) is hereafter defined as the RMS of the $\Delta\eta_{gen}$ distribution. σ_{η_G} has been evaluated with a MC simulation performed with single pion events generated at an energy of 2 < E < 140 GeV. The average particle energy is close to the average energy of the primary particles generated in the pseudorapidity acceptance of T2 by Pythia8 (~70 GeV for 7 TeV inelastic events). A Gaussian vertex smearing with a 5 cm standard deviation along the Z axis[9], is also introduced. η_R is an opportune estimator of the generator particle pseudorapidity. In the following the two track parameters η_{IMP} and η_{RZ} will be used as estimators of η_R (see sec. 3.6.3 for their definition). As for the primary efficiency, it is useful to introduce two different definitions of the resolution.

---

[9] This is the typical value measured by the CMS detector for the data used in the analysis of this thesis.

The "inclusive pseudorapidity resolution" ($\sigma_{\eta,i}$) and the "analysis oriented pseudorapidity resolution" ($\sigma_{\eta,a}$). The former is σ_{η_G}, while the latter is defined as the $\sigma_{\eta,i}$ but for tracks with |ZImpact| < 5 m and a |Z$_{min}$| < 13.5 m. $\sigma_{\eta,a}$ is introduced since in the analysis, reported in ch. 5, it will be important to know the resolution of the reconstructed data tracks which satisfy a similar condition in the ZImpact and Z$_{min}$ parameters. Fig. 3.14 shows the distribution of $\sigma_{\eta,i}$ (red curves) and $\sigma_{\eta,a}$ (blue curves) for two different estimators of η_R. Left and right figures refer to the particle resolution obtained with $\eta_R = \eta_{IMP}$ and $\eta_R = \eta_{RZ}$ respectively. As the plots show, a by far better resolution is obtained with the η_{IMP} estimator. This can be understood since this parameter implicitly performs a vertex constraint on the track reducing the small track lever arm. Of course, in order η_{IMP} to be a meaningful estimator of the true particle η, a proper primary track selection has to be performed in advance[10]. Another interesting aspect is the η dependence of the resolution obtained with the η_{IMP} estimator. More detailed studies have shown that the better resolution at higher η is due to the smaller effect that magnetic field and vertex smearing have on the particle propagation and on the particle entry point in T2, respectively. The increasing value with

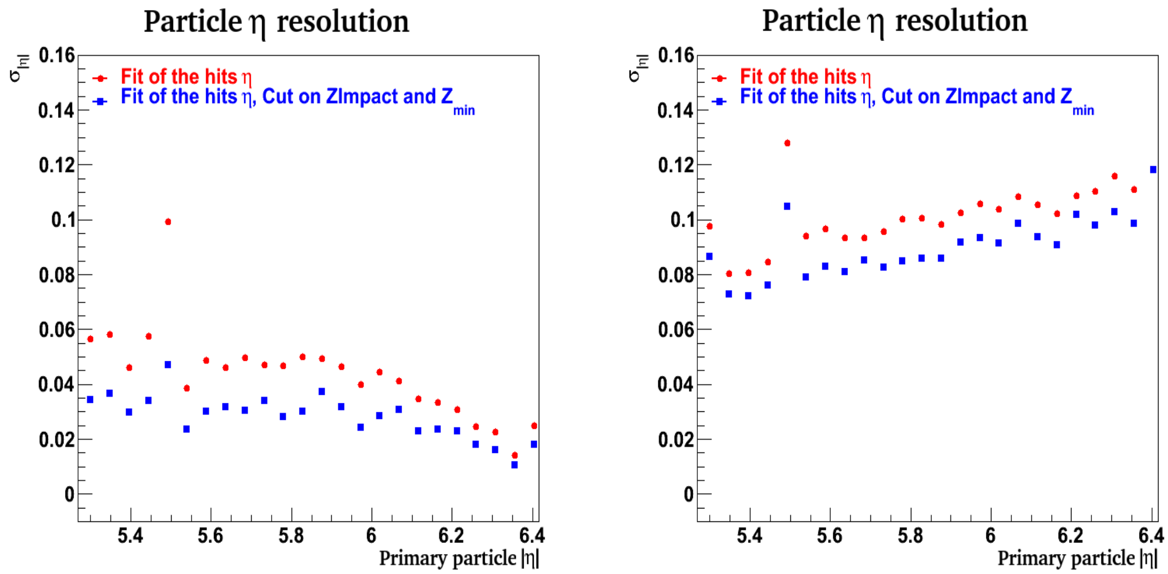

Figure 3.14: Particle pseudorapidity resolutions as a function of the generator particle η for single pion events uniformly generated in T2, with energy $2 < E < 140$ GeV. The red (blue) curve is for $\sigma_{\eta,i}$ and $\sigma_{\eta,a}$ respectively. Left and right curves are obtained with $\eta_R = \eta_{IMP}$ and $\eta_R = \eta_{RZ}$ respectively.

---

[10] the value of η_{IMP} is always in the range $5.3 < |\eta_{IMP}| < 6.5$ for each track reconstructed in T2 so it has not selecting power for the separation between primaries and secondaries

η of the resolution obtained with the η_{RZ} estimator is due to the relation which relates the track polar angle to the pseudorapidity: $\Delta\eta \sim \Delta\theta/\theta$

The pseudorapidity residual with respect to the GEANT track ($\Delta\eta_{GEANT}$) is defined as the difference between the η_{IMP} of the primary GEANT track crossing the detector and the associated reconstructed η_{IMP}. The track pseudorapidity resolution ($\sigma_{\eta_{GEANT}}$) is defined as the RMS of the $\Delta\eta_{GEANT}$ distribution. The same cuts on the reconstructed track parameters |ZImpact| and $|Z_{min}|$ already used for the $\sigma_{\eta,a}$ determination have been imposed. This quantity is important since it is insensitive to the changes that the particle pseudorapidity may have during the propagation from IP to T2.

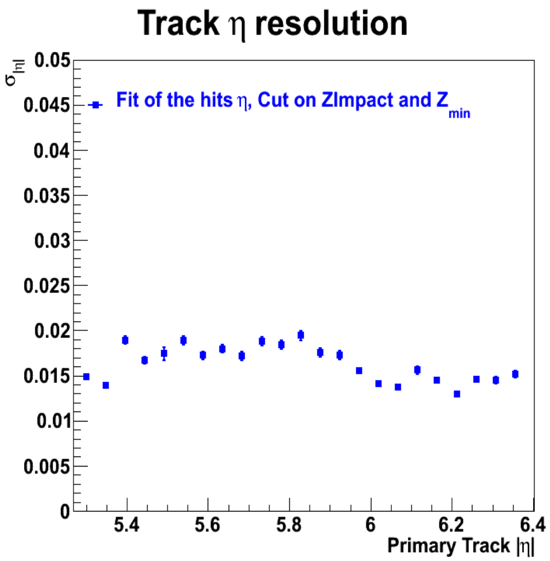

Figure 3.15: Track pseudorapidity resolution as a function of the primary GEANT track η for single pion events, with energy $2 < E < 140$ GeV, uniformly generated in T2.

The measurement of the track pseudorapidity resolutions, obtained with the same MC sample used for the σ_{η_G} determination, is shown in fig. 3.15.

3.7 Simulation of inelastic events

This section briefly reports the results on the particle multiplicity predicted by the simulation (see sec. 3.7.1) that is expected to be reconstructed in T2. The particle P_T acceptance in T2 is determined from a MC analysis (see sec. 3.7.2) which allows to take into account the effects that multiple scattering and magnetic field have on the primary particle propagation.

3.7.1 Multiplicity predicted by the simulation

The amount of particles produced by the interaction of the primaries with the material in front of and around T2 was found to be particularly challenging for both the detector performances and the physics analysis. The modelization of the forward region, simulated with GEANT, has been tuned with the data [64]. A large amount of secondary particles, which roughly constitute 90% of the signal in T2, is produced mainly in the vacuum chamber walls in front of the detector, in the beam pipe (BP) cone at $\eta = 5.53$ and in the lower edges of the CMS Hadron Forward (HF) calorimeter (see sec. 2.1.4 for a description of the forward region). Secondaries are also the main responsible of high-track multiplicity events, producing a strip occupancy larger than 40% for $\sim 10\%$ of the 7 TeV pp events.

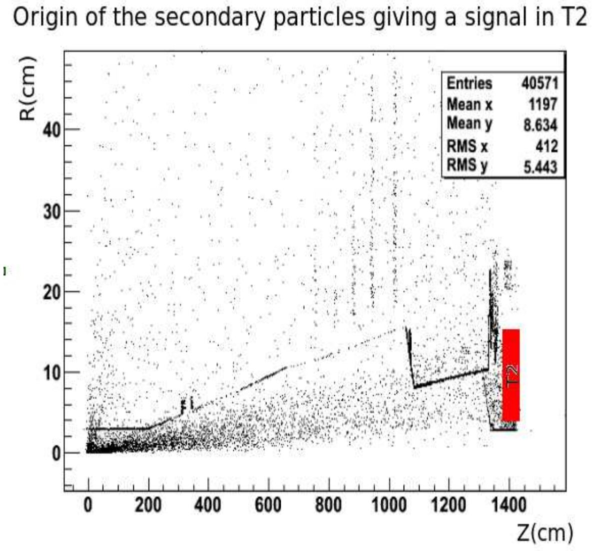

Figure 3.16: MC generated vertices of the secondary particles giving a signal in T2. The events have been obtained with Pythia MC simulation. The effect of the lower edge of the HF calorimeter is not included, as well as the contribution of showering particles. T2 is represented by the red square at Z∼14 m.

Fig. 3.16 shows the points where the secondary particles that are able to produce a signal in at least one of the T2 planes are generated. The results have been obtained with 7 TeV pp MB events simulated with Pythia8. The plot does not include the vertices of showering particles, as well as the interactions in the lower part of the HF calorimeter. Notice that in fig. 3.16 it is easy to recognise the structure of the BP, marked by the points where photon convertion happens.

A discrepancy of $\sim 30\%$ between data and the common tunes of Pythia8 inelastic simulation is found in the inclusive average pad cluster multiplicity per plane. The comparison is reported in fig. 3.17, for one of the T2 quarters. The observed discrepancy between data and simulation can be explained by the following:

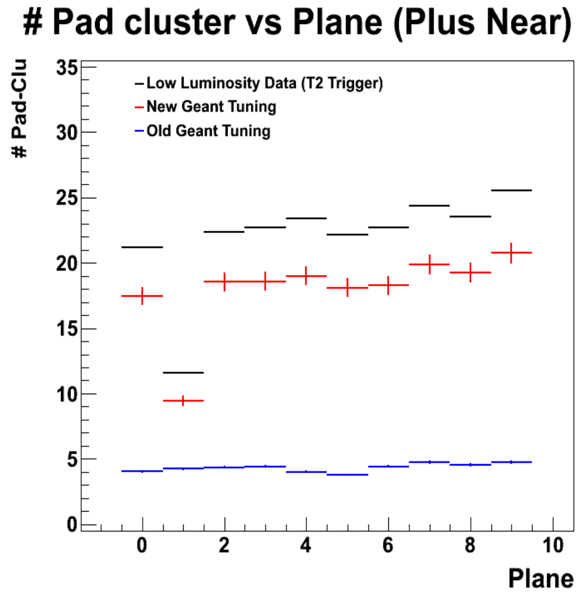

Figure 3.17: Average pad cluster multiplicity per plane, measured in the PN quarter. The black and red curves refer to data and to the latest tuning of the MC simulation, respectively. The blue curve represents the results obtained with the original GEANT tracking cut parameters.

- The lower primary $dN_{ch}/d\eta$ predicted by the Pythia MC with respect to the data (see ch. 5).

- The dependence of the secondary multiplicity on the forward energy, that T2 cannot measure. From simulation studies it is known that, for a given primary multiplicity, a higher average particle energy produces a higher pad cluster multiplicity in T2, due to the increased production of secondary particles. Moreover, CMS found an important discrepancy in the forward energy flow between the HF measurement and the Pythia simulation for 7 TeV MB events [82] (the latter underestimating the energy). Therefore it is possible that part of the discrepancy is due to a non perfect tuning of the MC energies in the forward region.

It is important to remark that a detailed work on the GEANT tracking range-cut parameter[11] and a thorough revision of the material simulation was needed in order to obtain a more realistic simulation of the event. In particular, the blue curve in fig. 3.17 shows the pad cluster multiplicity before the tuning: here a GEANT tracking range-cut of 11 m was used, with the consequence that a large part of secondary particles was not produced.

---

[11] The tracking range-cut parameters controls the generation of secondary particles in GEANT: if the simulation has a range-cut of X mm, a new secondary particle generated inside a volume is propagated only if it has the possibility to travel at least for X mm inside the same material where it was generated.

3.7.2 Primary particle P$_T$ acceptance

Multiple scattering (MS), magnetic field effects and inelastic interactions that particles may have with the material turn out to determine the primary charged particle P_T acceptance of T2. Due to the fact that the local magnetic field is weak and almost collinear with the track direction there is no selecting power for the lowest energy particles, which are still reconstructed as straight lines. The combined effects that MS and CMS central magnetic field have on the primary track ZImpact parameter have been investigated with MC simulation. Fig. 3.18 shows the primary track ZImpact parameter for a sample of tracks with energy 2 $<$ E $<$ 10 GeV (black curve) or 10 $<$ E $<$ 80 GeV (red curve).

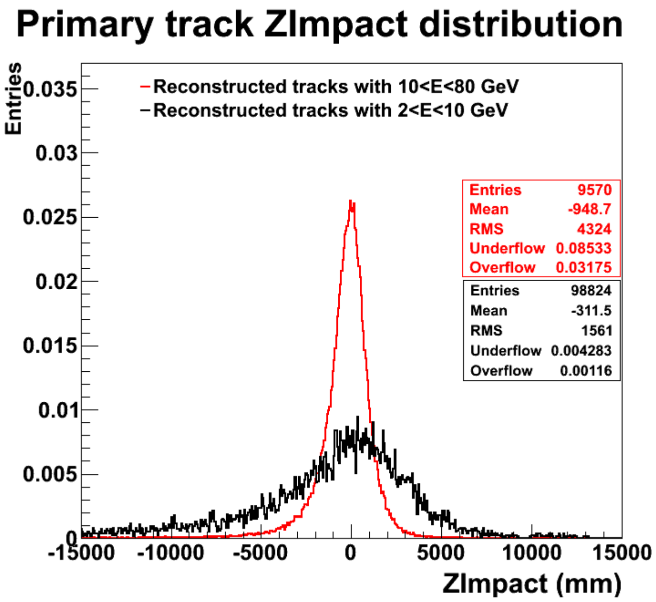

Figure 3.18: Distribution of the track ZImpact parameter for single pion events generated with energy 2 $<$ E $<$ 10 GeV (black curve) and 10 $<$ E $<$ 80 GeV (red curve).

The P_T acceptance is here defined as the probability to reconstruct the track from a particle with a given P_T. Because of the worsening of the ZImpact parameter resolution at lower energies, the low energy tracks are disentangled from the secondary tracks with a smaller efficiency. Therefore it is useful to define two P_T acceptances: the "inclusive" P_T acceptance where no analysis cut is imposed, and the "analysis-oriented" P_T acceptance, where a reference cut on the ZImpact parameter is imposed. Fig. 3.19 shows the single pion track reconstruction efficiency as a function of the particle P_T requiring or not a cut on the ZImpact parameter. The inclusive acceptance is close to 100% already at $P_T = 20$ MeV/c. Imposing a cut on the ZImpact ($|$ZImpact$| < 5$ m) an 80% acceptance is reached at $P_T = 40$ MeV/c.

The reference value of the particle P_T and energy acceptance (hereafter P$_{T\,Cut}$ and E$_{Cut}$),

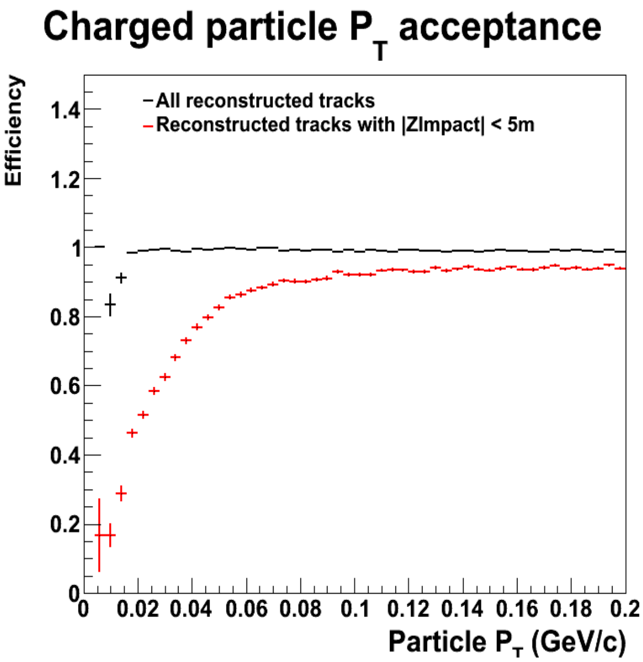

Figure 3.19: Efficiency of single pion reconstruction as a function of the particle P$_T$. The black (red) curve shows the "inclusive"("analysis oriented") P_T acceptance.

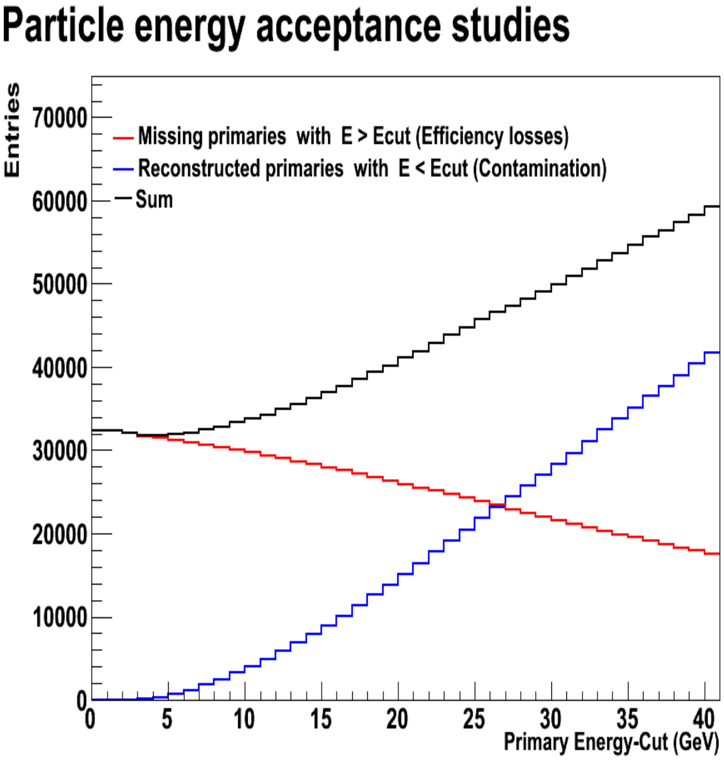

Figure 3.20: Number of primary tracks not reconstructed for E $>$ E$_{cut}$ (red curve) and number of primary tracks reconstructed with E $<$ E$_{cut}$ (blue curve) as a function of the primary energy cut (E$_{cut}$). The black curve shows the sum of the two. The results are obtained for simulated inelastic events.

have been decided with an analysis on pp MC events. The optimal E_{Cut} value has been defined as the one allowing the smallest correction on the counting of the primary track candidates with energy larger than E_{Cut} in a sample of 7 TeV inelastic pp events. These studies have been performed according to fig. 3.20, where only tracks satisfying the $|\text{ZImpact}| <$ 5 m condition have been considered. Here, for a given track sample, the inclusive number of primary charged particles with $E > E_{Cut}$ which are not reconstructed is reported as a function of the primary particle energy (red curve). The blue curve shows the number of primary tracks, having a smaller energy than E_{Cut}, which are reconstructed. This contribution represents the contamination of the sample by the low energy tracks. The black curve is the sum of the two curves previously defined and its minimum represents the value of the energy where the smallest correction is needed in order to obtain the true number of primary tracks with $E > E_{Cut}$. The optimal value has been found at 5 GeV, corresponding to an optimal P_T of 40 MeV/c.

Chapter 4

Detector alignment

In this chapter the algorithms developed in order to measure and to correct for the plane misalignments, i.e. the displacements that planes may have with respect to their nominal positions, are described. The alignment of the planes at the level of the nominal hit resolution is necessary in order to obtain the best precision on the track reconstruction. This level of precision cannot be obtained from survey measurements by which only an upper limit of $\sim$3 mm of misalignment per plane is guaranteed. Reconstructed tracks are therefore used in dedicated alignment algorithms which allow to find the systematic displacements of the planes with the needed precision. In the following, the detector misalignments are divided in two categories: internal and global misalignments. The internal one refers to the displacements of the planes in the same quarter with respect to each other, which can be resolved by looking at the systematic shift of the hit residuals with respect to the track. Two different methods (HIP and MILLIPEDE algorithm), described in sec. 4.1, have been developed in order to correct for such displacements. Global misalignments refer to the "collective" displacements that the planes in the same quarter can have with respect to their nominal positions, such as a common shift or a rotation of the T2-quarter. The measurement of the global misalignment, described in sec. 4.2, has been derived by studying the position on each T2 plane of the "beam pipe shadow" and by using dedicated algorithms allowing to measure the global misalignment parameter from the properties of the primary tracks. The relative misalignment between the two quarters of the same arm has been found by a procedure where the tracks reconstructed in the overlap regions are used (see sec. 4.3). The procedure adopted in order to correct the reconstructed hit position for such misalignments is reported in sec. 4.4. Before going into the details of the algorithms it is important to define the order by which the strategy that is applied to correct the event reconstruction for the misalignment biases is implemented:

1. The internal alignment corrections are found. Once these corrections have been applied, the tracks can be reconstructed with a better efficiency and $\chi^2 - p$ but in general with a poor parameter accuracy, due to the global misalignment biases.

2. The "beam pipe shadow" method is used for a first estimation of the global misalignments. The data are again reconstructed implementing the correction 1 and 2.

3. Then additional algorithms, described in 4.2.2, are used for a more precise estimation of the global misalignment parameters. The data are again reconstructed, implementing the new corrections.

4. The measurement of the relative quarter misalignments allows to cross check and eventually to refine the values of some of the global misalignment parameters previously found.

4.1 Internal alignment

The purpose of the internal misalignment analysis is to find the systematic displacements of the track hits in a particular detector, with respect to the expected propagation model of the particle. The most important internal alignment parameters which is possible to resolve within the T2 hit resolution are the shifts of the planes in the X and Y direction. Indeed, the pad pitch is too large to resolve an azimuthal rotation of the planes, while the X and Y displacements can be obtained by using tracks reconstructed close to the X or Y axis respectively. In fact, the hits associated to a track which is close to the X axis have their X-coordinate equal to the radial coordinate, which can be measured with a good precision by using the strip information only. A similar argument holds for the tracks close to the Y axis. Therefore, by making an appropriate selection of the tracks used in the internal alignment procedure, the transverse misalignment of each T2 plane can be resolved. Rotations of a given plane around the X and Y axis are expected to provide a negligible contribution to the coordinates of the hit associated to a primary particle, being its trajectory almost parallel to the beam direction. The same argument holds for small random displacements of the planes along the Z direction, which are expected to be at the mm level.

4.1.1 The HIP algorithm

In the "Hit and Impact Point" (HIP) alignment algorithm [83] the following "objective function" has to be minimised:

$$\chi^2 = \sum_k^{trk} \sum_i^{hits} \mathbf{r}^{\mathbf{T}}_{\mathbf{ik}}(\mathbf{p}, \mathbf{q_k}) \mathbf{V}^{-1}_{\mathbf{ik}} \mathbf{r}_{\mathbf{ik}}(\mathbf{p}, \mathbf{q_k}) \tag{4.1}$$

where the track residuals $\mathbf{r_{ik}}$ are defined as the difference between the measured hit position $\mathbf{m_{ik}}$ and the trajectory impact point $\mathbf{f_{ik}}$ obtained from the track extrapolation:

$$\mathbf{r_{ik}} = \mathbf{m_{ik}} - \mathbf{f_{ik}}(\mathbf{p}, \mathbf{q_k}) \tag{4.2}$$

In the above formula $\mathbf{q_k}$ are the parameters of the k-th track (called "local parameters"), $\mathbf{p}$ are the plane-dependent alignment parameters (called "global parameters") and $\mathbf{V}$ is the covariance matrix of the measurements.

The HIP algorithm iteratively minimises eq. 4.1 by assuming no dependence on the track parameters $\mathbf{q_k}$. Tracks are fitted excluding the hit in the plane where the misalignment correction is searched. The χ^2 is then iteratively minimised with a linear approximation with respect to the alignment parameters. In particular, a correction for the alignment parameters ($\mathbf{p_m}$) is found by using the Gauss-Newton method, where for each iteration of the algorithm an estimation of the alignment parameters is obtained as:

$$\mathbf{p_m} = [\sum_{\mathbf{i}}^{\mathbf{hits}} \mathbf{J_i}\, \mathbf{V_i^{-1}}\, \mathbf{J_i}]^{-1} [\sum_{\mathbf{i}}^{\mathbf{hits}} \mathbf{J_i}\, \mathbf{V_i^{-1}}\, \mathbf{r_i}] \tag{4.3}$$

where the Jacobian $\mathbf{J_i}$ is defined as the derivative of the residuals with respect to the plane position parameters only:

$$\mathbf{J_i} = \nabla_{\mathbf{p}} \mathbf{r_i}(\mathbf{p}) \tag{4.4}$$

The new alignment parameters are used to update the hit position in all the planes and the tracks are then refitted for the next iteration.

The HIP alignment algorithm implemented for T2 is greatly simplified thanks to the linear function $\mathbf{f_{ik}}$ which describes the particle propagation. In this case eq. 4.1 can be rewritten as two decoupled equations for the two misalignment parameter ΔX and ΔY. The equation to be minimised in order to find the misalignment of the plane i along the X direction (ΔX_i) is:

$$\chi^2 = \sum_k^{trk} \sum_i^{hits} \frac{(x_{ik} - a_k\, z_{ik} - b_k - \Delta\, X_i)^2}{\sigma_{ik}^2} \tag{4.5}$$

Where a_k and b_k are the slope and the intercept of the track in the XZ projection, x_{ik}, σ_{ik} are the x-position and the respective error of the hit in the plane i associated to the track k. The minimisation of eq. 4.5 with respect to ΔX_i leads to the following solution:

$$\Delta X_i = \frac{\sum_k^{trk} \frac{(x_{ik} - a_k\, z_{ik} - b_k)}{\sigma_{ik}^2}}{\sum_k^{trk} \frac{1}{\sigma_{ik}^2}} \tag{4.6}$$

Analogous equations hold for the ΔY_i misalignment parameters. The error on ΔX_i is estimated at the last iteration using the standard estimator $\sigma^2_{\Delta X_i} = \frac{1}{2}\frac{d^2\chi^2}{d\Delta X_i}^{-1}$. This error estimation is however not statistically rigorous[1], so the statistical error on the ΔX parameters is taken from the MILLEPEDE algorithm presented in sec. 4.1.2. The HIP algorithm is iterated (each time calculating the plane displacements and refitting the tracks) until all the displacements ΔX_i and ΔY_i are found below 20 μm[2]. Within this condition, the algorithm converges in less than 5 iterations. Despite the drawback that HIP procedure has on a direct estimation of the misalignment error, this algorithm is nevertheless important since it allows to cross check with an independent procedure the results obtained with the MILLEPEDE algorithm.

4.1.2 The MILLEPEDE algorithm

The MILLEPEDE algorithm allows to fit at the same time all the track and the misalignment parameters without inverting any large matrix. This method, proposed by Blobel [84, 85], offers as an additional advantage a statistically meaningful estimation of the error on the misalignment parameters. The measurement in the plane i-th is described by the following linear approximation (f is the same track extrapolation model of the previous section):

$$m_{i,k} \simeq f(\mathbf{q_k}, \mathbf{p})_i + \delta_{\mathbf{i}}{}^T\, \mathbf{\Delta}\, \mathbf{q}_k + \mathbf{d_i}{}^T\, \mathbf{\Delta}\, \mathbf{p} \tag{4.7}$$

where the local parameters $\mathbf{q}_k$ refer to the k-th track while the global parameters $\mathbf{p}$ represents the vector of the plane misalignments and are the same for all the tracks. $\delta_{\mathbf{i}}$ and $\mathbf{d_i}$

---

[1] Indeed the results are obtained after several iterations where the misalignment parameters and the track parameters are considered as independent

[2] This is a typical stopping condition. The algorithm is able to successfully converge with this condition if a sample of 1K or larger is used.

are the derivative vectors of the propagation model with respect to the local and the global parameters, respectively. The following χ^2 function:

$$\chi^2 = \sum_{k}^{tracks} \sum_{i}^{hits} w_{ik}\, r_{ik}^2 \tag{4.8}$$

has to be minimised with respect to both the local and the global parameters. r_{ik} is the residual function ($r_{ik} = m_{ik} - f(\mathbf{q_k}, \mathbf{p})_i$) and w_{ik} is the weight function (defined as the inverse of the variance of the measurement m_{ik}). Using the linear approximation (see eq. 4.7) the minimisation of eq. 4.8 with respect to the local and global parameters leads to the following system of equations:

$$\begin{pmatrix} \begin{array}{c|ccc} C & \cdots & G_k & \cdots \\ \hline \cdots & \cdots & \cdots & \cdots \\ G_k^T & 0 & \Gamma_k & 0 \\ \cdots\ \vdots & \cdots & \cdots & \cdots \end{array} \end{pmatrix} \cdot \begin{pmatrix} \Delta p \\ \cdots \\ \Delta q_k \\ \cdots \end{pmatrix} = \begin{pmatrix} b \\ \cdots \\ \beta_k \\ \cdots \end{pmatrix}$$

where $\mathbf{\Gamma_k}$ is the matrix used to fit the k-th track in the linear approximation, assuming the alignment parameter as fixed. Therefore $\mathbf{\Gamma_k \Delta q_k} = \beta_\mathbf{k}$, with:

$$\mathbf{\Gamma_k} = \sum_{hits\,\in\,Trk} w_i\, \delta_\mathbf{i} \delta_\mathbf{i}^\mathbf{T} \quad ; \quad \beta_\mathbf{k} = \sum_{hits\,\in\,Trk} w_i\, r_i\, \delta_\mathbf{i} \tag{4.9}$$

The nxn matrix $\mathbf{C}$ (where n is the number of alignment parameters) and the nx1 vector $\mathbf{b}$ can be calculated adding for each track the following contributions:

$$\mathbf{C} = \ \mathbf{C}\ + \sum_{hits\,\in\,Trk} w_i\, \mathbf{d_i}\, \mathbf{d_i^T} \qquad \mathbf{b} = \ \mathbf{b}\ + \sum_{hits\,\in\,Trk} w_i\, r_i\, \mathbf{d_i} \tag{4.10}$$

The nxm matrix $\mathbf{G_k}$ correlates the track parameters (m for each track) to the alignment parameters:

$$\mathbf{G_k} = \sum_i w_{ik}\, \mathbf{d_i}\, \delta_\mathbf{i}^\mathbf{T} \tag{4.11}$$

The matrix equation written above cannot be inverted directly because of its large size. Indeed the size of the system scales with the number of tracks used in the alignment, O(10K) in this case. The MILLEPEDE method uses the Shur complement[3] in order to efficiently extract the solution for the global parameters. The equation can be solved for the unknown $\mathbf{\Delta\, p}$ vector by using the following relation:

$$\mathbf{C}'\,\mathbf{\Delta\, p} = \mathbf{b}' \tag{4.12}$$

with the matrix $\mathbf{C}'$ and the vector $\mathbf{b}'$ being updated for each track with the following equations:

$$\mathbf{C}' = \mathbf{C}' + \sum_i w_i \mathbf{d_i} \mathbf{d_i^T} \mathbf{G_k} \mathbf{V_k} \mathbf{G_k^T} \tag{4.13}$$

$$\mathbf{b}' = \mathbf{b}' + \sum_i w_i r_i \mathbf{d_i} \mathbf{G_k}\, \mathbf{V_k}\, \beta_\mathbf{k} \quad \text{with} \quad (\mathbf{V_k} = \mathbf{\Gamma_k^{-1}}) \tag{4.14}$$

Eq. 4.12 allows to find the misalignment parameters by a matrix inversion of a (small) nxn matrix. This method provides an exact solution for the internal misalignment parameters and iterations are only needed in order to check the approximation introduced by the linearization of the propagation function. These general equations have been rewritten in a code of the CMSSW framework and adapted for the needs of the T2 misalignment issue. With the decoupling of the fit in the two independent projections, the following form for the local and global vectors have been found:

$$\begin{aligned} \delta_\mathbf{i} &= (1, z_i) \\ \mathbf{d_i} &= (\delta^K_{0i}, .., \delta^K_{9i}) \end{aligned} \tag{4.15}$$

$\mathbf{d_i}$ is therefore the i-vector of the ten-dimensional Cartesian base (δ^K_{ji} is the Kronecker-delta).

For each quarter and each projection **C′** is a 10x10 matrix to be inverted. The problem of finding the misalignment parameters with the MILLEPEDE algorithm is not completely solved until proper constraints on the χ^2 function are applied. Indeed, as long as tracks are well fitted by a straight line, the χ^2 value in eq. 4.8, is invariant with respect to any linear

---

[3] For a matrix equation with the following structure (each element can be a matrix):

$$\begin{pmatrix} C_{11} & C_{12} \\ C_{21} & C_{22} \end{pmatrix} \cdot \begin{pmatrix} a_1 \\ a_2 \end{pmatrix} = \begin{pmatrix} b_1 \\ b_2 \end{pmatrix}$$

having defined $B = (C_{11} - C_{12} C_{22}^{-1} C_{12}^T)^{-1}$, the solution can be written as:

$$\begin{pmatrix} a_1 \\ a_2 \end{pmatrix} = \begin{pmatrix} B & -B C_{12} C_{22}^{-1} \\ -C_{22}^{-1} C_{12}^T B & C_{22}^{-1} - C_{22}^{-1} C_{12}^T B C_{12} C_{22}^{-1} \end{pmatrix} \cdot \begin{pmatrix} b_1 \\ b_2 \end{pmatrix}$$

coordinate transformation [86].

Global shift and tilts of the whole quarter are examples of displacements for which the χ^2 is invariant. If no constraints is imposed, the solution provided by the MILLEPEDE algorithm will be one among the infinite others having the same minimum χ^2. Two of the transformations that cannot be seen by the algorithm are shown in fig. 4.1. It is important to remind that, if the solution is not constrained, all these transformations can be randomly introduced in the solution by the MILLEPEDE algorithm. Linear constraints on the misalignment parameters solution are therefore introduced using the Lagrange multiplier method: if the previously mentioned χ^2 is subjected to the constraint $f^T\,\Delta p = f_0$, the following function $\tilde{\chi}^2$ should be minimised:

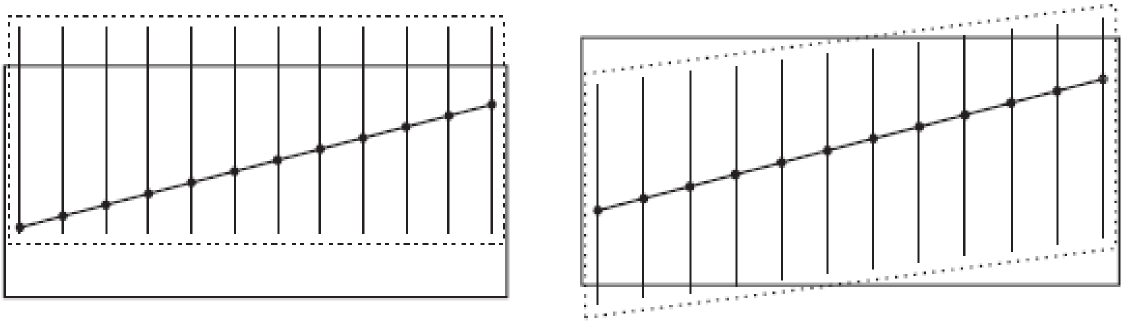

Figure 4.1: Example of unconstrained degrees of freedom: a shift (left) and a tilt (right) in one of the projections.

$$\tilde{\chi}^2 = \chi^2 + \lambda(f^T\,\Delta p - f_0) \tag{4.16}$$

where λ is an additional unknown parameter. The system of equations to be solved which satisfied the constraint condition is:

$$\left(\begin{array}{c|c} C' & f \\ \hline f^T & 0 \end{array}\right) \cdot \left(\begin{array}{c} \Delta p \\ \hline \lambda \end{array}\right) = \left(\begin{array}{c} b' \\ \hline f_0 \end{array}\right)$$

The constraint condition adopted in the MILLEPEDE algorithm is to have for each quarter two of the planes (called reference planes) with the same misalignment parameter found by the HIP algorithm. In particular, the planes that are found to have a small displacement both in the X and Y direction are selected[4]. f_0 and λ are therefore vectors of size 2. This criteria allows to compare the solutions of the two algorithms when applied on the same sample of data. With this procedure, the problem of finding the internal misalignment parameters has been reduced to the invertion of a 12x12 matrix for each of the misalignment projection. An additional advantage of this method is that all variances and covariances are available from the matrix C'^{-1} which is the covariance matrix for the misalignment parameters.

4.1.3 Event and track selection

To make a precise estimation of the internal alignment parameters, cuts on the event properties and on the track parameters have to be applied. The cuts utilized by both the HIP and MILLEPEDE algorithms, presented in sections 4.1.1 and 4.1.2, are reported in table 4.1. There, the horizontal line separates the conditions on the event properties from those on the track ones. The cuts 1, 2, 3 are used in order to select events where there is no ambiguity in the track reconstruction due to particles traversing the detector at close distance. Indeed cut 1 insures a low multiplicity and therefore a low probability of showers, where tracks are more clusterized. Cuts 2, 3 refer to the separation of the tracks entry point in the T2 detector. The large separation values were used to guarantee a low intersection probability even for the planes after the entry points. Since the internal alignment is studied for each quarter independently, these cuts refer to the selected quarter only. The parenthesis in cut 5 means that the condition applies for X-shift (Y-shift) misalignment study respectively. This cut is used to select tracks close to the X or Y axis, in order to fully exploit the strip precision. The conditions 6 and 7 on the hit cluster size refer both to hits forming

Table 4.1: Event selection and track selection cuts utilized by the internal alignment algorithms

1. Max number of tracks per quarter	5
2. Min ΔR separation between tracks in the same quarter	30mm
3. Min $\Delta\Phi$ separation between tracks in the same quarter	15 °
4. Min number of class-1 Hit forming the track	6
5. Entry point minimum X/R or (Y/R)	0.7
6. Hit Max number of strips	4
7. Hit Max number of pads	4

---

[4] Indeed, no reliable independent measurement to be used as a constraint is available.

the tracks and to hits used in the residual determination. The track sample used for the internal alignment analysis is obtained with a modification of the standard parameters of the track fitting and road finding algorithm: the maximum separation distance between the projected hit and the propagated point is enlarged from 2 to 4 σ_{hit} (see sec. 3.6). The analysis on the outliers reduction made by the tracking algorithm is not activated. In order to make a more efficient collection of hits from displaced planes, another step has been added to the standard tracking algorithm. After a first collection of tracks has been found, the algorithm looks in a cylinder around each track having a radius of 2.5 mm. The hits not already considered in the track but contained in the cylinder are added as new hits before next track fitting step. The inclusion of the displaced hits with a high efficiency is a key point for the success of the alignment algorithms: a low efficiency inclusion of the hits from the displaced plane means that mainly the hits having the smaller residual are included. A bias on the reconstructed displacements could be therefore introduced, with a consequent underestimate of the plane displacements.

4.1.4 Results

In this section the main results on the performance of the HIP and MILLEPEDE algorithms are reported. Fig.4.2 shows the output of the HIP algorithm for the ΔX (left) and ΔY (right) shifts of the planes in one quarter. The blue circles refer to the misalignment measured on collision data. For each plane the misalignment measured on the data is introduced in the simulation (see sec. 4.4) by changing, in each plane, the position of the GEANT hit. As a control check, the algorithm is therefore applied also to a sample of MC inelastic events simulated with the planes in the misaligned position. The misalignment found for MC events is shown in fig. 4.2 with the green triangles.

Once the constraints on the MILLEPEDE algorithm have been applied, as explained in sec. 4.1.2, the two algorithms show a good agreement between their results. The comparison of the alignment parameters found by the two algorithms on the same data sample is shown in fig. 4.3.

The improvement of the track $\chi^2 - p$ distribution due to the internal misalignment correction is shown in fig. 4.4 (right) for a data sample of pp collision events. The effect of the misalignment correction has also been studied on a MC sample (see fig. 4.4, left) where the same plane misalignments found in the data are introduced and then corrected during the reconstruction. In both histograms only events with an average pad cluster multiplicity per plane between 1 and 6 have been selected[5]. The misalignment configuration loaded in

---

[5] This event selection has been applied to have a similar sample of track multiplicities both in data and

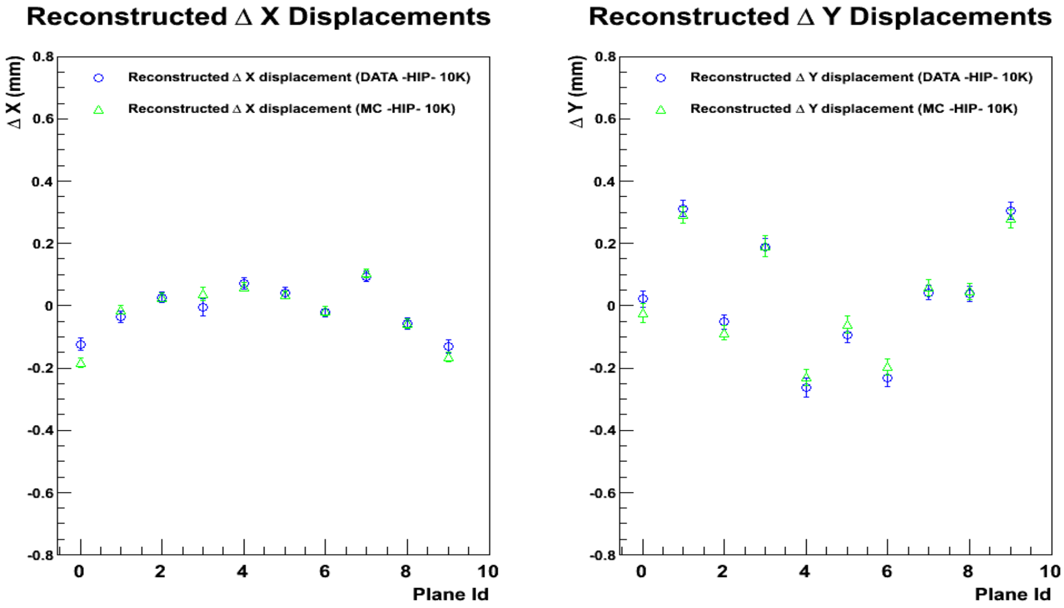

Figure 4.2: ΔX (left) and ΔY (right) internal misalignment reconstructed by the HIP algorithm, as a function of the plane in one of the T2 quarters. The results found on the data (blue circles) are compared to the results obtained in MC events including the misalignment simulation (green triangles). The results have been obtained with a sample of ~5K tracks.

the simulation is the one measured on 2011 pp data.

A measurement of the resolution by which the algorithms can determine the misalignment has been obtained from a MC simulation study. Indeed, the statistical error only cannot be taken as the whole uncertainty affecting the misalignment values found by the algorithms. For example it is known that the algorithm results can have some dependence on the initial track parameter distributions. Therefore, a MC analysis is necessary, where the reconstructed misalignment parameters are compared with the misalignment values introduced in the simulation. For this purpose, a sample of different internal misalignment configuration has been generated where each plane is randomly shifted by using an uniform distribution of width 1.2 mm centred around 0. It is worthy to notice that 0.6 mm is the maximum value of the plane internal misalignment measured so far on the data. The difference between the shift introduced at the GEANT level and the reconstructed shift given by the alignment algorithms is computed and shown in fig. 4.5 (left) for both the ΔX and ΔY plane misalignments.

The RMS of the distributions, obtained with a sample of ~10K tracks, is $< 10\mu m$ for

---

MC, with a similar performance of the tracking algorithm.

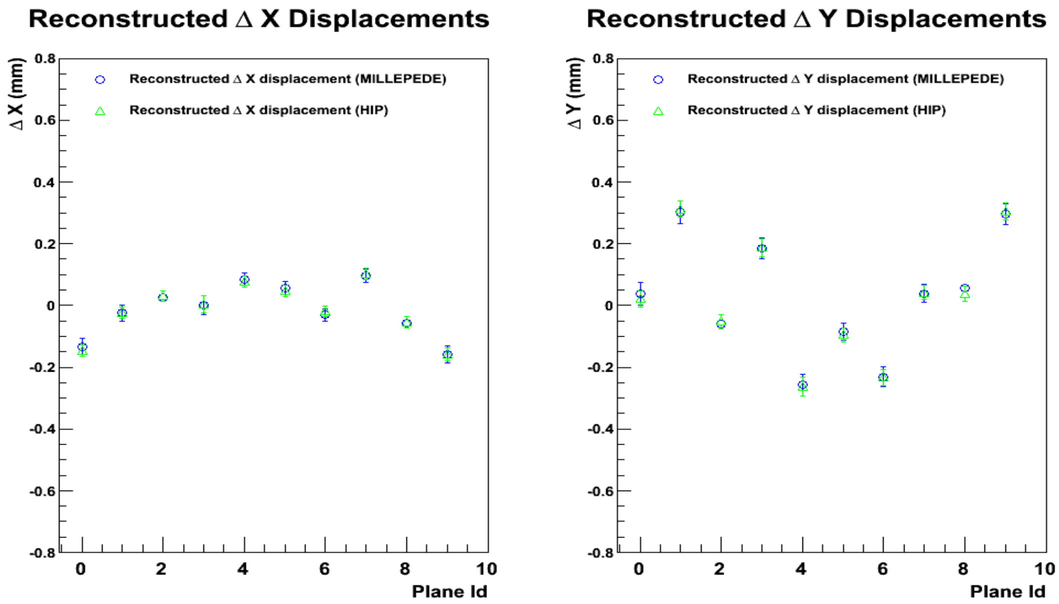

Figure 4.3: ΔX (left) and ΔY (right) internal misalignment as a function of the plane ID in one of the T2 quarters. The MILLEPEDE results (blue circles) are compared to the HIP results (green triangles).

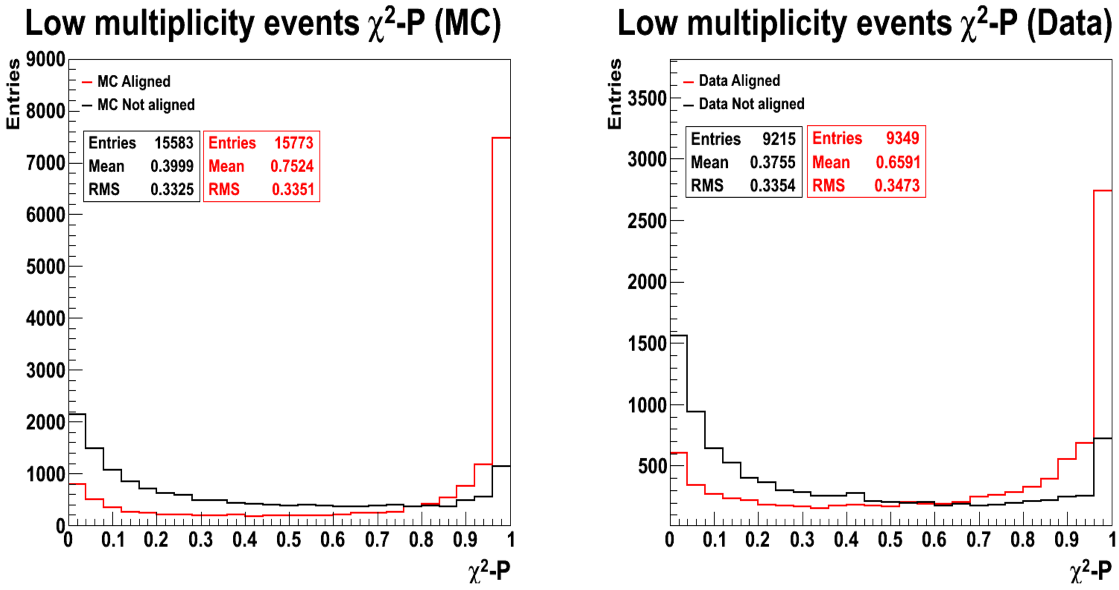

Figure 4.4: Track χ^2-p for MC events (left) and data (right). The black curves refer to reconstruction where the misalignment correction is not introduced, while the red curve is obtained applying the misalignment correction.

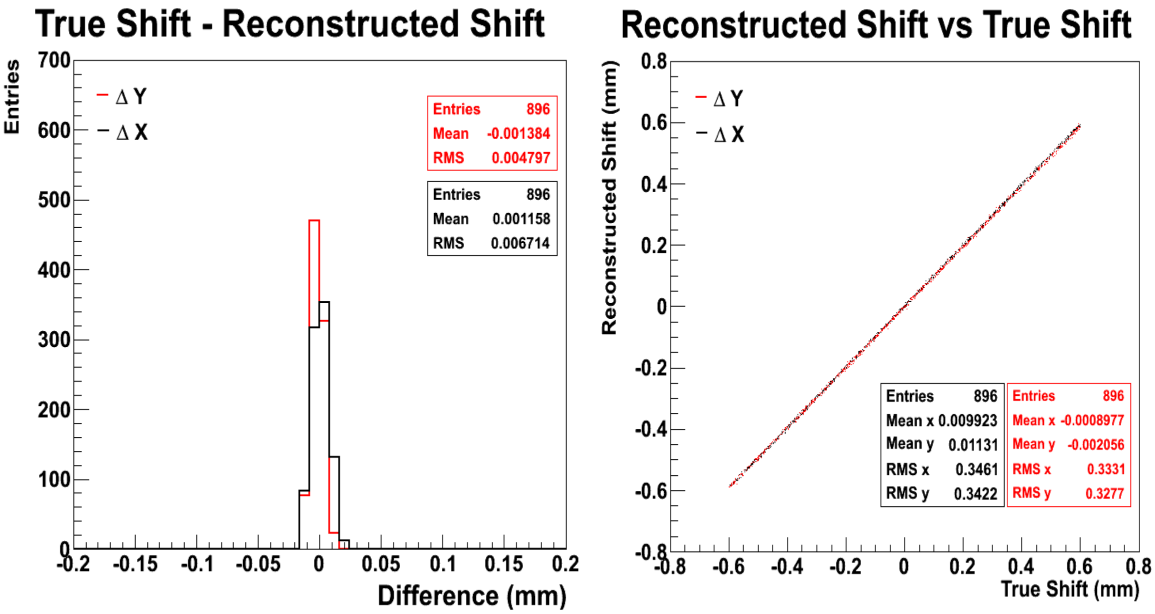

Figure 4.5: Left: difference between the simulated and reconstructed displacement. Right: reconstructed displacement vs simulated displacement. Results in red (black) are for the ΔY (ΔX) misalignment.

both the X and Y displacements. To validate the robustness of the algorithm results, the distribution of the measured values of the shifts versus the corresponding values simulated in the MC is reported in fig. 4.5 (right), which shows a full correlation.

In fig. 4.6 the convergence of the algorithm to the true misalignment value as a function of the number of track N used in the analysis is shown. For samples larger than 2K tracks the precision of the algorithm is better than $7\mu m$, enough to be considered as a negligible contribution to the hit position uncertainty (see sec. 3.5).

Table 4.2 reports the internal misalignment values of the 40 T2 planes as measured by the MILLEPEDE algorithm for the 2011 pp runs. The reported error is the statistical one. Planes marked with a star are considered as reference planes. The analysis has been performed with ~100K events, with a track sample size useful for the analysis between 1K and 4K, depending on the quarter.

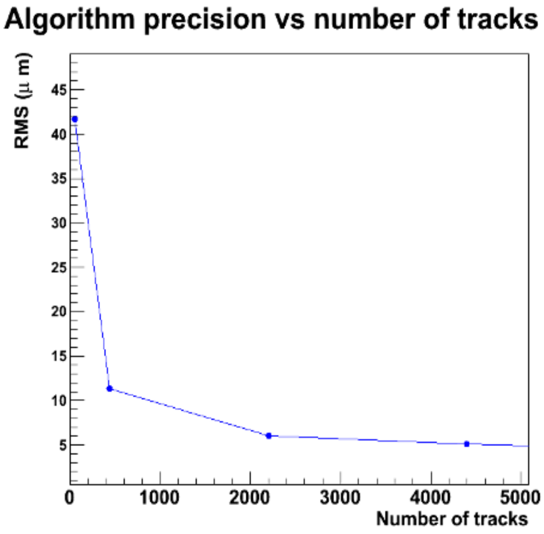

Figure 4.6: RMS of the distributions shown in fig. 4.5 as a function of the number of tracks used in the analysis. The results shown have been obtained for the ΔY shift, using the MILLEPEDE algorithm.

Table 4.2: Values of the internal misalignment parameters measured on 2011 data

Plane	ΔX (mm)	ΔY (mm)	$\sigma_{\Delta X}$ (mm)	$\sigma_{\Delta Y}$ (mm)
0*	-0.099	-0.001	0.005	0.004
1	0.0422	0.138	0.006	0.004
2	0.196	-0.057	0.005	0.004
3	-0.190	0.096	0.005	0.004
4	0.060	-0.108	0.005	0.004
5	0.008	0.032	0.005	0.004
6*	0.102	-0.214	0.005	0.004
7	-0.147	0.037	0.005	0.004
8	0.131	-0.035	0.005	0.004
9	-0.096	0.429	0.005	0.005
10	-0.149	0.011	0.007	0.006
11	-0.034	0.258	0.007	0.006
12*	0.050	-0.064	0.007	0.006
13	0.035	0.196	0.007	0.006
14	0.065	-0.267	0.005	0.006
15	0.024	-0.071	0.005	0.005
16	-0.002	-0.223	0.005	0.005
17	0.105	0.048	0.005	0.005
18*	-0.045	0.066	0.006	0.005
19	-0.142	0.272	0.006	0.006
20	0.235	0.082	0.020	0.010
21	0.315	0.226	0.017	0.010
22	-0.003	-0.224	0.013	0.008
23*	-0.082	-0.037	0.012	0.008
24	-0.218	0.118	0.011	0.008
25	-0.143	-0.115	0.011	0.008
26	0.104	-0.215	0.010	0.008
27	-0.061	0.149	0.011	0.008
28*	0.044	0.058	0.011	0.008
29	0.281	0.185	0.011	0.010
30	0.266	0.220	0.009	0.012
31	-0.013	-0.117	0.009	0.012
32*	-0.168	-0.094	0.009	0.012
33	-0.051	0.046	0.008	0.011
34	-0.012	0.176	0.008	0.011
35	0.041	0.006	0.008	0.011
36	-0.006	-0.150	0.008	0.011
37*	-0.010	-0.286	0.008	0.011
38	0.050	0.347	0.008	0.011
39	0.045	0.103	0.008	0.011

4.2 Global alignment

The global misalignment corrections have been derived by studying the properties and the expected symmetries of the primary track parameter distributions. The most important global misalignment that affects the reconstructed track parameters is the tilt of the quarters in the XZ and YZ projections. The global shift of the quarter on the X and Y direction is found to play a secondary role. Indeed, with the same reasons mentioned for the internal alignment case, we are not considering global rotations around the Z axis. Moreover, since rotations of the planes around the X and the Y directions cannot be seen, the term "tilt in the XZ and YZ projection" is here associated to a progressive movement of the planes in these projections, with the detector plane still parallel to the XY plane. It is therefore assumed that these movements are also describing possible rotations of the quarter around the X or Y axis.

It is expected that quarters can coherently move whenever the magnetic field is switched ON or OFF. It has also been found that the position of the quarters is stable during the time, i.e. the position taken by the quarters when the CMS magnetic field is ON is always the same. The global misalignment of the T2 quarters are instead found to change every time that the detector is removed from the CMS region for maintenance and then reinstalled. To give an idea of how much important the understanding of the quarter misalignment is, some consideration on how the quarter tilt can affect the reconstruction of the ZImpact parameter (widely used during the analysis, see ch. 5) is hereafter reported. T2 is about 14 m away from the IP and in the best case the reconstructed track has a length of 40 cm in Z (10 hit tracks). Plane inefficiencies and large clusters (not useful for the fit) can make the Z-length of the track even smaller. Consequently, T2 has a very short lever arm toward the IP for track reconstruction. Therefore, calling R$_{IN}$ the radial entry point of a track in the T2 detector and θ the reconstructed track angle, the Z position of the vertex at the IP will be reconstructed (assuming that the track lies in the RZ plane) as $Z = R_{IN}/tan(\theta)$. The main contribution to the error on the Z-parameter is given by the error propagation on the angle θ, $\sigma_Z \sim$14m*$\sigma_\theta/tan^2(\theta)$. For instance, at $\eta = 5.4$ a σ_θ =1 mrad gives an uncertainty in Z of about 1.5 m. Given the θ dependence, the Z resolution is expected to be furthermore degraded for particles with a smaller angle. Other effects are known to degrade the Z resolution, like magnetic field and multiple scattering (see sec. 3.7.2). From these simple considerations it is evident that the global misalignments of the quarters, which introduce a bias in the reconstruction of the track angles, should be corrected at the sub-mrad level. After a description of the methods utilized to measure the quarter global misalignment (sec. 4.2.1 and 4.2.2), the performance of the algorithms and the estimated correction uncertainties will be reported in sec. 4.2.3.

4.2.1 Alignment correction using the beam pipe shadow

Primary particles generated at a η close to 5.53 have a large probability to interact with the material of the beam pipe cone placed at $10.7 < z < 13.3$ m (see sec. 3.7). As an effect of this interaction a lack of hits in the radial region of each of the T2 planes corresponding to $\eta \sim 5.53$ is found. In other words, it is possible to see “the shadow” of the BP on the T2 planes. This feature has been used for the purpose of the T2 quarter alignment. Indeed, assuming that the BP is perfectly placed on its nominal position, the observed shadow in each T2 plane is sensitive to its local and global misalignment. The Y-profile of the hits measured on data in a particular plane and associated to the selected tracks is shown in fig.

4.7. The nominal position of the beam pipe shadow (the one which should be measured in a perfectly aligned quarter) is known from MC simulation. Therefore, by comparing the MC beam pipe shadow with the one obtained in data, the displacements of the planes with respect to their nominal positions can be measured.

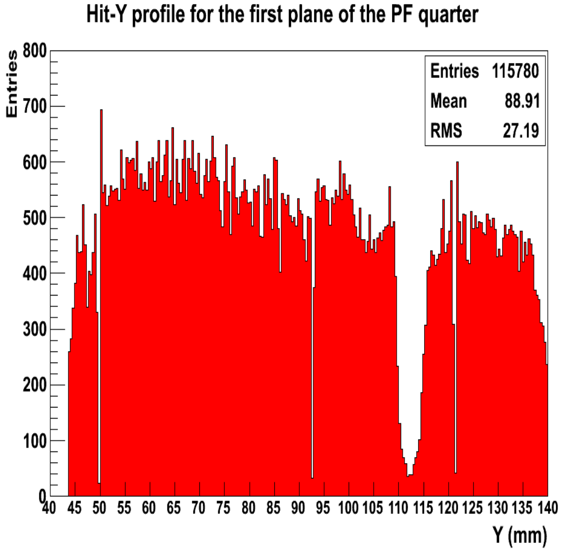

Figure 4.7: Hit Y distribution for track hits in the PF quarter. The dip around 112 mm is due to the shadow of the beam pipe. The other 3 narrow dips at around 50, 93, 122 mm are due to the separation of the GEM foil.

The position of the beam pipe shadow is measured in the data only for hits close to the Y axis or to the X axis. This allows to determine with the maximum precision the absolute displacement of the plane in the X and Y direction respectively. Once the quarter is internally aligned, the shadow seen in the XZ or YZ projection of each plane is a straight line as a function of the Z-position of the plane. Therefore by fitting the shadow position and comparing it with its nominal position, a direct estimation of the tilt and shift of the quarters can be found both in the XZ or YZ projection. An example of this method is shown in fig. 4.8, where the position of the beam pipe shadow, defined as the minimum of the hit profile (hereafter X_{min} or Y_{min}) of the corresponding T2 plane, is measured in the planes of one quarter (the PN), both for MC (red lines) and data (blue lines). In particular the shadows close to the X axis are reported in the top picture of fig. 4.8, while the bottom pictures show the shadows close to the Y axis for both $Y<0$ (left) and $Y>0$ (right). One of the problems of the hit profile fit is that the shape can be modified by a non-homogeneous hit reconstruction efficiency of the plane. This fact prevents the use of an unique analytical function to perform the fit of the minimum position for all the planes. Consequently, the position of the beam pipe shadow and its associated error are estimated by a measurement of the width of the dip at a height which safely includes the minimum. Since many of the distributions have a flat shape close to the minimum, the measured interval is considered

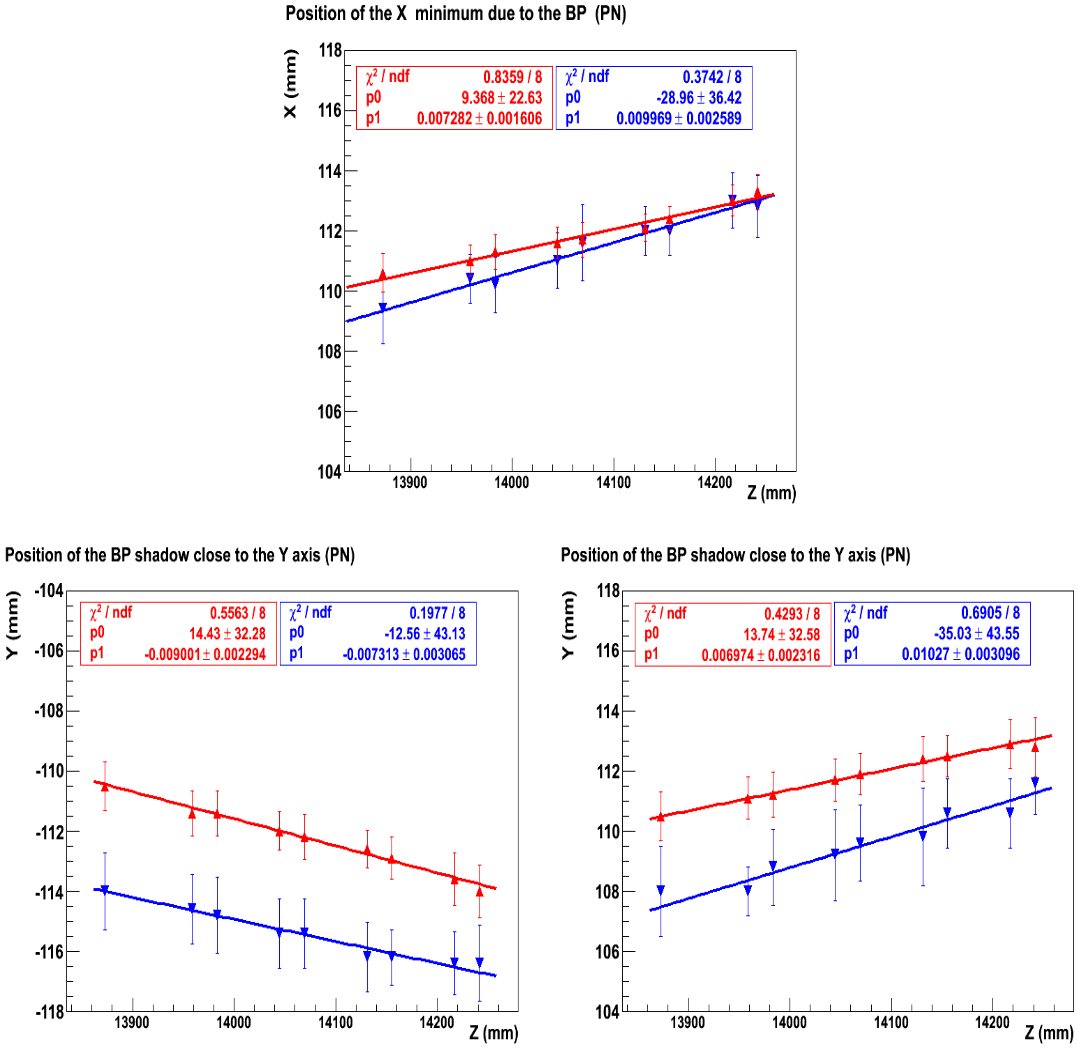

Figure 4.8: Fits of the beam pipe shadow position for hits close to the X axis (top) and for hits close to the Y axis with Y<0 (bottom-left) and Y>0 (bottom-right). Blue and red lines have been obtained from data analysis and MC analysis respectively. The second plane, having a low efficiency has not been included in the fit.

as the width of an uniform distribution having the estimated minimum position at its centre. To obtain the global misalignment parameters of each quarter, the X_{min} (Y_{min}) value of each plane measured on the data, has been subtracted from the respective X_{min} (Y_{min}) value obtained in the simulation. A linear fit is then performed on these differences and the values of the quarter tilts and of the shifts are directly extracted. For the measurement of the misalignment parameters in the YZ projection, where two measurements per plane of the BP shadow position are available, the results are combined.

4.2.1.1 Event and track selection

The event and track selection cuts used by the method presented in sec. 4.2.1 are reported in tab 4.3.

Table 4.3: Event selection and track selection cuts utilized by the BP shadow algorithm

1. Maximum number of pads per plane	60
2. Entry point minimum X/R or (Y/R)	0.9
3. Min number of class-1 Hit forming the track	7
4. Min track $(\chi^2\!-\!\mathrm{p})_{XZ}$ and $(\chi^2\!-\!\mathrm{p})_{YZ}$	0.05
5. Max track |ZImpact|	6 m

In order to have a good performance of the tracking algorithm the analysis is performed selecting events where all planes have a pad occupancy less than 60 on the quarter studied (cut 1) and selecting hits with $\mathrm{X}_{IN}/\mathrm{R}_{IN}$ ($\mathrm{Y}_{IN}/\mathrm{R}_{IN}$) > 0.9 for the alignment in the XZ (YZ) projection respectively (cut 2). Only good quality tracks (cuts 3, 4) and only hits associated to tracks with a |ZImpact| <6 m (cut 5) are considered.

4.2.2 Alignment correction using the primary track parameters

Some of the track parameters associated to the primary particles are expected to have a symmetric distribution in case of a perfectly aligned quarter. This idea is at the basis of the global misalignment correction methods reported in this section. More in general these algorithms use tracks which are supposed to arrive from the IP with a straight line propagation. This information is used to estimate the shifts and the tilts characterizing each quarter. Two methods (named M1 and M2) have been developed, allowing the estimation of the value of these misalignment parameters.

4.2.2.1 The M1 method

The M1 method uses the following formula in order to estimate the values of the tilt parameter in the XZ projection ($\Delta\beta$):

$$\Delta\beta = \langle \frac{x_i - x_0}{z_i - z_0} - \frac{x_0}{z_0} \rangle \Big|_{i \neq 0} \tag{4.17}$$

where the symbol $\langle\,\rangle$ indicate an average over a wide sample of selected tracks, and x_i (z_i) are the X (Z) coordinate of an hit associated to the track and reconstructed in the $i-th$ plane. The purpose of eq. 4.17 is to measure the difference between the track angle locally reconstructed (which is subjected to the misalignment bias) and the angle deduced from the entry point of the track, assuming that the particle is coming from the IP. This difference is mainly due to the quarter tilt, which can be therefore estimated. An analogous expression is used for the tilt parameter in the YZ projection ($\Delta\alpha$). The above formula is biased by the effect of the shift on the X direction (Δ X). For an unbiased formula the term $\frac{x_0}{z_0}$ in eq. 4.17 should be replaced by $\frac{x_0-\Delta_x}{z_0}$. However this correction is expected of the order of $\frac{\Delta_x}{z_0} \sim 0.1$ mrad and it is therefore neglected.

4.2.2.2 The M2 method

The M2 method is an iterative algorithm for the reconstruction of the quarter tilt and shift parameters. Each vertex, for a perfectly aligned detector, is the origin of a certain number of tracks which satisfy:

$$\begin{cases} v_x^G &= v_x^Q &= a\,v_z^G + b \\ v_y^G &= v_y^Q &= c\,v_z^G + d \end{cases} \tag{4.18}$$

where v indicate the vertex, G and Q are the symbols which denotes the global reference frame and a reference frame fixed to the quarter. The latter is supposed to have the XY^Q plane of the first detector of the quarter and the Z axis crossing the centre of each semicircular plane. The parameters a (c) and b (d) are the slope and the intercept of the projection of the track in the XZ (YZ) plane, fitted in the quarter reference frame. It should be noted that the first equality holds only in a case of perfect alignment, when the XY planes of the two reference systems differ only by a translation along Z. In the case of a quarter misalignment the vertex position coordinates measured by the quarter change. By denoting with $\tilde{Q}$ the misaligned quarter frame the following relations hold:

$$\begin{cases} v_x^{\tilde{Q}} &= a\,v_z^{\tilde{Q}} + b \\ v_y^{\tilde{Q}} &= c\,v_z^{\tilde{Q}} + d \end{cases} \tag{4.19}$$

The transformation allowing to relate the vertex coordinates measured in the misaligned quarter frame to the coordinates measured in a perfectly aligned quarter frame is:

$$\begin{cases} v_x^{\tilde{Q}} &= v_x^Q - \Delta_x^Q - v_y^Q \Delta_\gamma^Q + v_z^Q \Delta_\beta^Q \\ v_y^{\tilde{Q}} &= v_y^Q - \Delta_y^Q + v_x^Q \Delta_\gamma^Q + v_z^Q \Delta_\alpha^Q \\ v_z^{\tilde{Q}} &= v_z^Q - \Delta_z^Q - v_y^Q \Delta_\alpha^Q - v_x^Q \Delta_\beta^Q \end{cases} \tag{4.20}$$

where the rotation matrix $M_{\alpha\beta\gamma}$ and the translation vector Δr, which relates the two frames, have been expressed as:

$$M_{\alpha\beta\gamma} = \begin{pmatrix} 1 & \Delta_\gamma^Q & \Delta_\beta^Q \\ -\Delta_\gamma^Q & 1 & \Delta_\alpha^Q \\ -\Delta_\beta^Q & \Delta_\alpha^Q & 1 \end{pmatrix} \quad ; \quad \Delta r = \begin{pmatrix} \Delta x^Q \\ \Delta y^Q \\ \Delta z^Q \end{pmatrix}$$

with the $\Delta_\alpha^Q, \Delta_\beta^Q$ and Δ_γ^Q being the (small) rotations around the X,Y and Z axis and the translations along these axes. By substituting eq. 4.20 in eq. 4.19 it is possible to find a relation between the local track parameter and the position of the vertex in the aligned frame. After that proper approximations are performed during the calculation of the products, eq. 4.19 can be rewritten as:

$$\begin{cases} b \;=\; v_x^Q - a\, v_z^Q - \Delta x^Q + v_z^Q \Delta_\beta^Q \\ d \;=\; v_y^Q - c\, v_z^Q - \Delta y^Q + v_z^Q \Delta_\alpha^Q \end{cases} \tag{4.21}$$

Since it is assumed that only tracks from IP are selected, the transverse vertex position in the perfectly aligned quarter frame ($v_{x,y}^Q$) is put to 0. Therefore the two relations in eq. 4.21 can be utilized independently to extract the parameters of the transformation which generates the misalignment. In particular the quantity $\chi^2_{PV,XZ}$:

$$\chi^2_{PV,XZ} \equiv \sum_i^{trk \in PV} \left(\frac{b_i - (-a_i\, v_z^Q - \Delta x^Q + +v_z^Q \Delta_\beta^Q)}{\sigma_{b_i}} \right)^2 \tag{4.22}$$

has been minimised considering tracks coming from the primary vertex (PV), selected in the XZ projection with the condition of tab. 4.4. To minimise the value of $\chi^2_{PV,XZ}$, the function has been evaluated on a grid of the $\Delta x^Q \Delta_\beta^Q$ plane, with pitch 0.3 mm in Δx^Q and 0.05 mrad in Δ_β^Q. The grid is a square of 6 mm x 10 mrad, centred in (Δx^Q,Δ_β^Q)=(0,0). After the minimum has been found, the hits are corrected for the misalignment parameters and the track are refitted. The iterations stop when the alignment correction on Δ_{β}^{Q} is below 0.1 mrad. A similar analysis has been performed for the YZ projection, starting from the second expression of eq. 4.21.

4.2.2.3 Event and track selection

The event and track selection criteria adopted in order to apply the M1 and M2 methods are reported in 4.4. The results are expected to be biased by the track sample choice much more than the internal alignment case. This is easy to understand since the methods rely on a high-purity sample of primary tracks.

Table 4.4: Event selection and track selection cuts utilized by the global alignment algorithms

1. Max number of tracks per quarter	5
2. Min ΔR separation between tracks in the same quarter	30mm
3. Min $\Delta\Phi$ separation between tracks in the same quarter	15 $^\circ$
4. Min number of class-1 Hit forming the track	7
5. Entry point minimum X/R or (Y/R)	0.7
6. Min track $(\chi^2\text{−p})_{XZ}$ and $(\chi^2\text{−p})_{YZ}$	0.05
7. Max track slope error	1 mrad
8. Max track |ZImpact|	5-6.5 m
9. Track tanθ_X (tanθ_Y) - (X$_{IN}$ (Y$_{IN}$)/ Z$_{IN}$)	<15 mrad
10. Sign of the slopes compatible with the primary condition	

Here the requirement of low multiplicity events (point 1) is not only imposed for a better track reconstruction, but also because it is known that high multiplicity events are dominated by secondary particles, which must be removed from the track sample used by the algorithms. Cuts 2, 3 are imposed to avoid bad track reconstruction in events with close tracks. Cuts 4, 5 have been already discussed for the internal misalignment case. Moreover, since the internal alignment is already performed, the track is required to have a good $\chi^2 - p$ and a small error on the slope projections (cuts 6, 7). A minimal compatibility of the tracks with the primary vertex is imposed by the cuts 8, 9, 10. For cut 8 two values have been reported. As it will been shown in sec. 4.2.3, a 6.5 m cut is necessary for tilts approaching 6 mrad. For such big misalignments, the use of a more tight cut was found to make a bias on the track sample with a consequent underestimate of the reconstructed misalignment parameter. The cuts can be reduced at a level of 5 m for global tilts below 4 mrad. Cut 9 imposes that the reconstructed slope in the quarter frame cannot be too different from the one expected according to the entry point of a primary track. Cut 10 means that the sign of the two slope projections should be compatible with the hypothesis that the track is coming from the vertex: in this case the hit |X| and |Y| should increase with |Z| and the sign of the slopes have to be compatible with this condition.

4.2.3 Results

The uncertainty on the fit parameters obtained with the beam pipe shadow method (see sec. 4.2.1), have been estimated to be ∼2-3 mrad and ∼1 mm for the tilt and the shift parameters respectively. Especially for the tilt measurement, this resolution is not enough, and the M1 and M2 methods (presented in sec. 4.2.2) have to be used in addition. The BP shadow method is nevertheless important since it allows to put a first bound on the global misalignment parameters and, concerning the quarter shift, it is competitive with the other methods presented in this chapter. After the corrections predicted by this method are applied to the data, the M1 or M2 methods are applied for a more precise determination of the misalignment tilt parameters. The resolution of the M1 and M2 algorithms has been first evaluated with a MC simulation, by generating single muon events. This allows to understand the performance of the algorithms independently from the purity of the analysis cuts used to select the primary tracks. Random misalignment configurations have been generated with the tilt parameters uniformly distributed in the [-6 mrad, +6 mrad] range and the shift parameters in the [-3 mm, 3 mm] range. These intervals have been chosen according to the maximum size of the tilts that have been measured so far on the data (for example using only the beam pipe shadow method) and from the mechanical constraints that are expected to bound the shift parameters. The results obtained with the M2 algorithm are shown in fig. 4.9: the left picture reports the difference between the generated tilt value and the reconstructed misalignment angle for both the XZ (black) and the YZ (red) projections. In the right picture the reconstructed versus the simulated misalignment values are shown. A cut on the |ZImpact| of 6.5 m was used (see point 8 in tab. 4.4). From the RMS of fig. 4.9 (left) we see that an average resolution better than 0.2 mrad has been found for the reconstruction of the tilt parameters. Similar plots have also been studied for the M1 algorithm, which showed a slightly worse resolution (∼0.3 mrad). Therefore, hereafter only the performances of the M2 algorithm will be further investigated in more detail.

Fig. 4.10 shows the convergence of the M2 algorithm to the true misalignment $\Delta\alpha$ value as a function of the number N of track used in the analysis. For samples larger than 1K tracks the precision of the algorithm is already better than 0.2 mrad. Similar results have

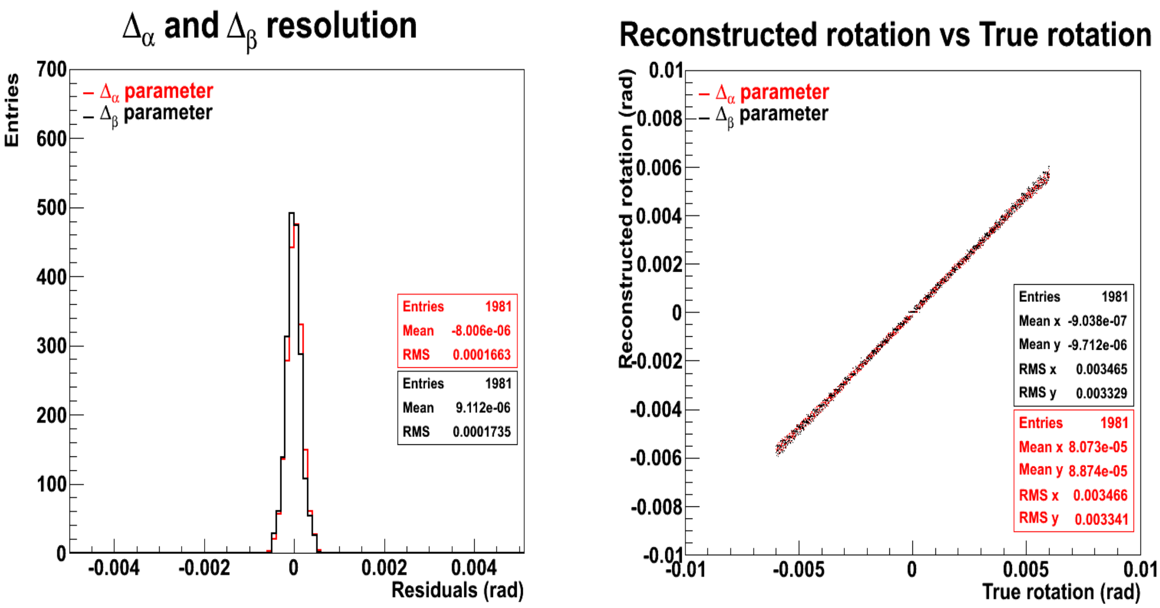

Figure 4.9: Left: difference between the simulated and reconstructed tilt parameters. Right: Reconstructed vs simulated tilt parameter. Results in red (black) are for the $\Delta\alpha$ ($\Delta\beta$) parameter.

been found for the $\Delta\beta$ parameter.

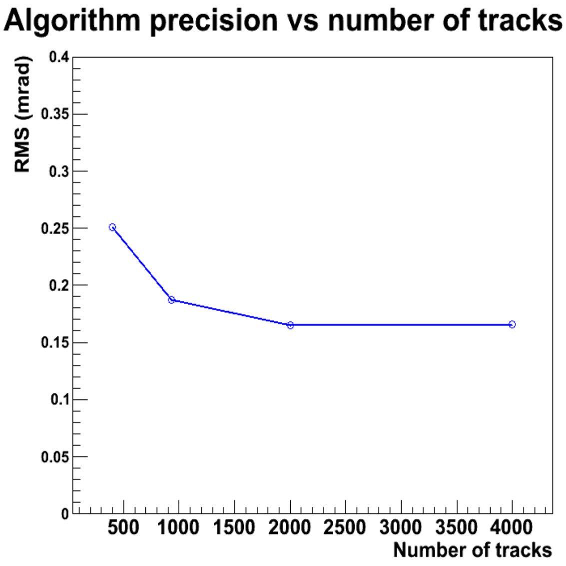

Figure 4.10: RMS of the distribution (simulated $\Delta\alpha$-reconstructed $\Delta\alpha$) as a function of the number of tracks used in the analysis. The results have been obtained with the M2 algorithm.

The resolution on the shift parameter obtained with the M2 algorithm is instead poor. This is due to the high correlation that each shift parameter has with the corresponding tilt parameter. A resolution of about 2 mm has been found for the two shifts. The beam pipe shadow method is therefore preferred for the estimation of the shift parameters. It is important to remark that both the M1 and the M2 algorithms has been found to be quite sensitive on the ZImpact cut utilized during the primary track selection. As an example, if a |ZImpact| cut of 5 m is used, the average resolution of the Δ_β parameter is about 0.4 mrad. In this case, the misalignment scenarios which are badly reconstructed were found to be the ones affected by a larger misalignment, where the ZImpact cut is responsible for the exclusion from the analyzed sample of the larger angle tracks. It is therefore important to repeat the resolution studies on pp MC events where the |ZImpact| cut also controls the amount of secondary particles included in the sample. About 20K MB events are generated where the configuration of the global misalignment parameter has been varied in the same range as for the single particle studies. The simulated internal misalignment configuration was measured on the 2011 data. To take into account the uncertainty on the internal misalignment parameters, a gaussian distributed smearing with a standard deviation of $10\mu m$ was introduced in the procedure of the hit position correction. The measured resolution shows similar behaviour as the one already reported for the single track studies: the cut on the |ZImpact| parameter is found to bias the results for large misalignments if chosen to be smaller than $\sim$5 m, while a $|\text{ZImpact}| = 6.5$ m cut is found to give a better resolution. The plot for the tilt parameters resolution and the comparison with the simulated misalignment parameters are reported in fig. 4.11.

The resolution of the two angular parameter $\Delta\alpha$ and $\Delta\beta$ is found to be $\sim$0.3 mrad, a bit worse than in the single track case. The resolution obtained with the M1 algorithm is found to be 0.4-0.5 mrad.

Table 4.5: Values of the global misalignment measured on 2011 data

Quarter	Δ_β (mrad)	Δ_α (mrad)	Δ X (mm)	Δ Y (mm)
PN	3.3 ± 0.3	-2.0 ± 0.3	-2 ± 1	-2 ± 1
PF	1.0 ± 0.3	-6.4 ± 0.3	2 ± 1	0 ± 1
MN	-5.2 ± 0.3	-0.5 ± 0.3	0 ± 1	1 ± 1
MF	-1.5 ± 0.3	-0.5 ± 0.3	-1 ± 1	-1 ± 1

Table 4.5 reports the values of the global misalignment measured for each quarter on the 2011 data. As already mentioned, a good global alignment of the T2 detector is fundamental for the $dN_{ch}/d\eta$ analysis that will be presented in the next chapter. In order to have a feeling of how sensitive are the track parameters on the global misalignment, we report in fig. 4.12 the distribution of the track ZImpact parameter for both MC (left) and data (right) events, with (blue curve) and without (red curve) any global alignment correction.

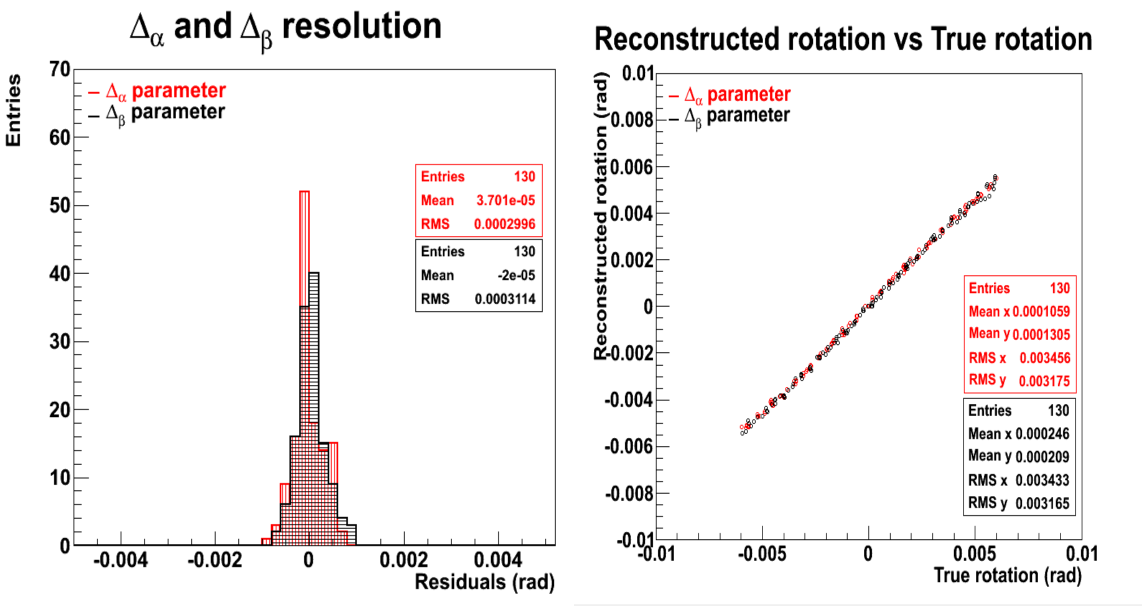

Figure 4.11: Left: difference between the simulated and reconstructed tilt parameters. Right: reconstructed vs simulated tilt parameter. Results in red (black) are for the $\Delta\alpha$ ($\Delta\beta$) parameter.

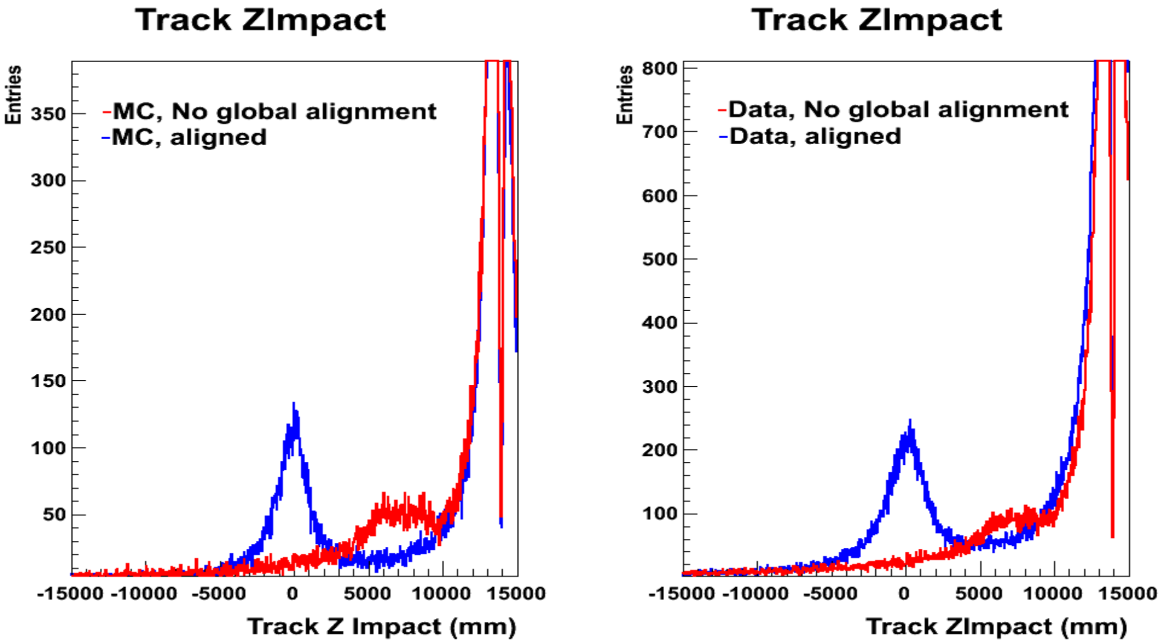

Figure 4.12: Track ZImpact parameter reconstructed in the PF quarter in pp MC simulation (left) and data (right). The blue (red) curve is obtained with (without) the inclusion of the global alignment corrections.

This parameter is fundamental for the selection of the primary tracks, and its distribution measured in an aligned quarter should have a symmetric peak around ZImpact=0. As shown by the figure the primary track signature would be completely lost without a proper global alignment correction.

4.3 Relative quarter alignment

The alignment of two quarters with respect to each other is performed by exploiting the overlap region that the two quarters of the same arm have around the Y axis. This is obtained by searching the tracks going through this region in low multiplicity events. The tracks are reconstructed independently for each quarter. If each quarter of the same arm has a reconstructed track in the overlap region and the two tracks have a Y entry-point which differ by less than 3 mm, than the track pair is selected as a single particle candidate. An estimation of the relative tilt parameters is found by making a weighted average of the track slope difference of each pair. The relative quarter shifts are obtained from a weighted average of the differences between the tracks coordinate of each pair evaluated on the plane XY^{Q}.

This "relative quarter alignment" has been found to be useful to cross check the results found by the previous global alignment procedures, at least for the Y-shift and for the YZ tilt of the quarters. The reasons why it cannot be efficiently used for the other misalignment parameters are the following:

- Lack of resolution in the overlap region along the X direction: indeed this region is characterized by strips almost parallel to the X direction. The more precise measurements that can be performed in the overlap region on the X position are obtained at small R, where the smaller pad area is already 2x2 mm^2.

- Lack of acceptance at small R: for relative misalignments where the two quarters move away from the small R regions, here the two quarters don't overlap anymore. So the part of the detector which is more effective for the investigation of the relative misalignment in the X direction cannot be used.

- Inefficiency at the detector edges: the GEM plane is inefficient at its edges where the gain rapidly drops. Therefore, since at small R the inefficiency is found to be relevant for the first and the second column of pads closer to the detector edge, the corresponding overlapping region (which have size of 12° i.e. $\sim$4 pads) cannot be used for tracking purposes.

The overlapping region is instead used to make a very precise test on the consistency of the ΔY shift and the Δ_α tilt parameter of the two quarters, found by the procedures previously described. The track and event selection cuts used in the analysis are reported in table 4.6. The results have been obtained only using single track simulation, since disentangling primary from secondary tracks is not crucial for this analysis, so the full pp MC simulation is not necessary. Fig. 4.13 shows the difference between the reconstructed and the simulated relative Δ_α misalignment (left) and relative ΔY misalignment (right). The resolution on the ΔY and Δ_α parameter, is better than 0.2 mm and 0.2 mrad respectively.

Table 4.6: Event and track selection cuts utilized for the relative alignment of the quarters. The tracks are selected in the overlapping region.

1. Max number of tracks per quarter	5
2. Min ΔR separation between tracks in the same quarter	30mm
3. Min $\Delta\Phi$ separation between tracks in the same quarter	15 °
4. Min number of class-1 Hit forming the track	7
6. Min track χ^2–P$_{XZ}$ and χ^2–P$_{YZ}$	0.05
7. Max relative error of track tanθ_Y	$< 5\%$

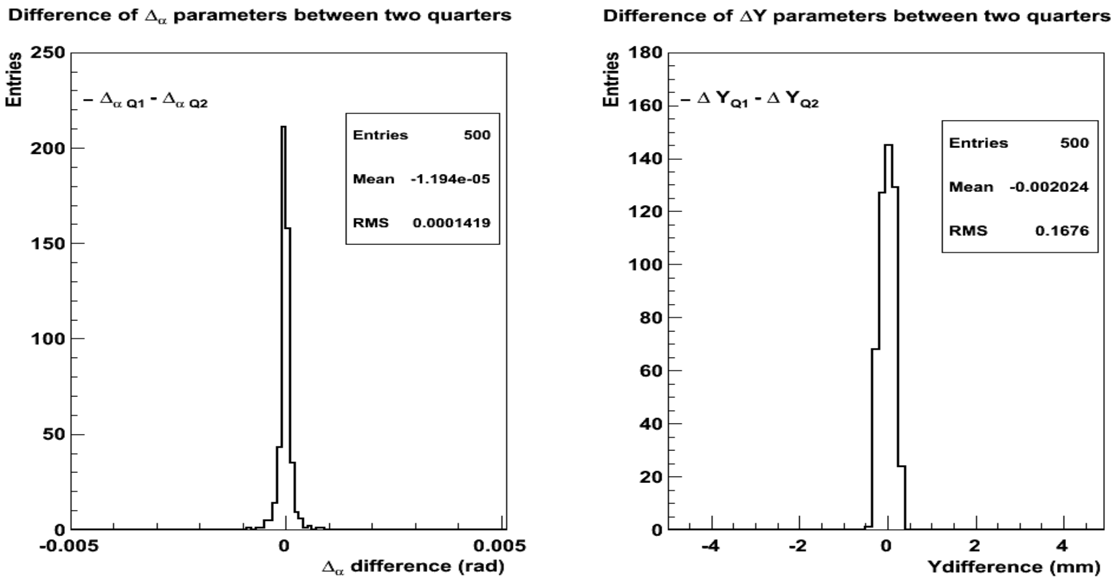

Figure 4.13: Difference between the simulated and the reconstructed relative Δ_α parameter (left) and relative ΔY (right).

4.4 Position correction procedure

Once the alignment corrections have been found, the hit positions measured on data have to be corrected. The correction procedure is complicated by the fact that the hit resolution in X and Y is not constant over the plane area. This means that the effect of the misalignment is not the same for all the reconstructed hits. This is not intuitive if one imagines the T2 quarter as a "rigid body" with all the reconstructed hits solidly moving with it when a misalignment transformation is applied to the quarter. This "rigid body" condition would happen only in the case of hits with an infinite resolution. To illustrate better the issue for the T2 case, suppose that only a tilt in the XZ plane takes place. In this case only the tracks reconstructed close to the X axis would "feel" completely this misalignment, while the tracks close to the Y axis would be only slightly affected by the quarter movement. Indeed, for reasonable values of this rotation, a particle which crosses the detector close to the Y axis would be still detected by the same pad that would be fired in a condition of perfectly aligned detector. This means that, if a standard correction of all the hit positions is performed, by inverting the transformation applied in eq. 4.20, the hits would be properly corrected only in part. Therefore, even if the misalignment parameters are exactly found, the alignment correction process does not guarantee that the obtained reconstructed tracks are identical to the ones reconstructed in a perfectly aligned geometry. This effect is clearly shown in fig. 4.14, where the distribution of the tracks slopes projected in the XZ plane ($\tan\theta_X$), obtained for a single muon MC simulation, are reported. In this simulation a tilt of 2.5 mrad in the XZ plane has been introduced. The left plot shows this distribution for tracks selected at $\pm 20^\circ$ around the X axis. In this case, the standard ("rigid body") correction procedure (red curve) is able to correct very well the distribution, which well matches the one obtained with a simulation where no misalignment is implemented (black curve). The right picture of fig. 4.14 shows that a standard correction procedure works quite bad if the tracks are instead selected around the Y axis, where a lower resolution in the $\tan\theta_X$ parameter is expected. In this case the larger part of tracks do not feel the misalignments, while their $\tan\theta_X$ have been shifted by the correction procedure.

A good correction algorithm should be able to take into account the effects that digitization has on the hit resolution and the misalignment corrections should be implemented accordingly.

Since the correction badly acts only for low resolution hits (and therefore tracks), it is clear that, without taking into account this effect, the error introduced by the misalignment corrections on the hit position and on the track parameter is smaller than the error that the track parameter and hit position have by themself, due to the reduced resolution.

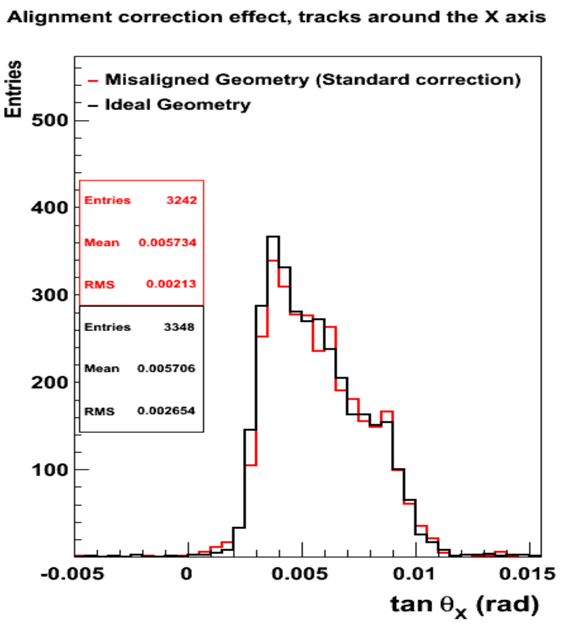

Figure 4.14: Distribution of the tanθ_X track parameter from single muon MC simulation. The left (right) plot is obtained selecting tracks close to the X (Y) axis. The black curve shows a simulation without misalignment, while the red one shows a simulation where misaligned is corrected without taking care of the hit resolution.

Nevertheless, the bias introduced by a standard correction algorithm has been found not negligible, since it can give an important contribution to the inefficiency on the primary track selection. As a first solution to this problem it has been found that a more realistic alignment correction is obtained if the predicted movement of the hits is corrected only in the radial direction. In particular, once the misalignment parameters are computed, the position that each hit would have if it would be an infinite resolution hit is computed ("rigid body" correction). This is done simply by inverting the transformation which moves the hit from the real misaligned frame to the ideal frame. The predicted (X,Y) correction vector is then projected in the radial direction, and only the hit radial position is corrected, while the azimuthal coordinate is maintained fixed. The reconstructed (X,Y) hit position is finally updated accordingly to this strategy. This approximation reflects the facts that the misalignment is fully felt by the strips, while the pads, having a much lower resolution, are supposed to collect the same signal as for a perfectly aligned detector. Fig. 4.15 shows the track ZImpact (left), Z_{min} (centre) and R_0 (right) distributions reconstructed in MC events with the PN quarter. The events are reconstructed with the proposed strategy of misalignment correction (red curve) and with the standard-"rigid body" misalignment correction (black curve). The reconstruction is also compared with the case where no misalignment

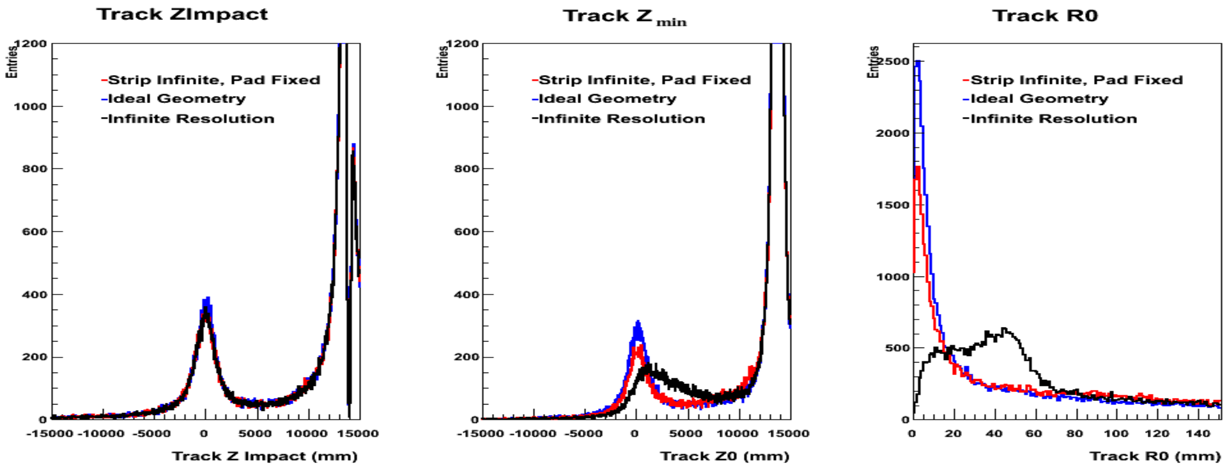

Figure 4.15: Track ZImpact (left), Z_{min} (centre) and R0 (right) distributions reconstructed in the PN quarter for simulated MB events. The parameters are shown for a geometry where no misalignment is introduced (blue curve) and for a misaligned geometry corrected without taking into account the finite resolution of the hits (black curve) or with the correction strategy described in the text (red curve).

is simulated (blue curve).

As shown in fig. 4.15, the proposed strategy for the hit correction allows to better reproduce the track parameter shapes reconstructed with the non misaligned geometry. It is very important to notice that the ZImpact parameter has been found to be the most robust track parameter with respect to the biases introduced by the global misalignments. This is one of the reasons why it has been chosen as the most important parameter for the primary to secondary track separation, as explained in sec. 5.

Chapter 5

Charged particle pseudorapidity density measurement

The pseudorapidity density of charged particles produced in high energy pp collisions reflects the strong interaction dynamics, which is only partly described by perturbative QCD. Non perturbative models and parametrisation are used in the Monte Carlo (MC) event generators to describe the hadronisation of the partonic final states and to model the diffractive processes [87, 88]. In the forward region, where peripheral diffractive processes are important, the uncertainties are pronounced. A better understanding of these effects is also important for the interpretation of high energy showers recorded by cosmic ray experiments [89, 90, 91]. A direct measurement of the forward particle density is therefore extremely valuable in constraining the theoretical models for particle production in pp interactions. In this chapter the measurement of the charged particle pseudorapidity density ($\mathrm{dN_{ch}/d}\eta$) in the range $5.3 < |\eta| < 6.4$ is presented. This measurement has never been performed so far at such forward pseudorapidities by any experiment at a collider. This makes TOTEM an unique experiment for the study of the forward charged particles produced in inelastic interactions. At the same time, it is worthy to remind that this study is particularly challenging due to the long distance between T2 and the IP and the large amount of secondary particles. In sections 5.1 and 5.2 the definition of the measurement is given and the description of the data and of the MC sample used for the analysis is reported. In section 5.3 the analysis procedures needed for the $\mathrm{dN_{ch}/d}\eta$ evaluation are reported. For each correction, the analysis method for its determination and for the estimation of the associated systematic uncertainty is reported. In sec. 5.4 the analysis strategy which combines these corrections in order to obtain the $\mathrm{dN_{ch}/d}\eta$ measurement is presented. A resume of the statistical and systematic uncertainties and the method used for their combination is reported in section 5.5. The $\mathrm{dN_{ch}}/\mathrm{d}\eta$ measurement, compared with several MC generators, is shown in sec. 5.6. An overview of the charged particle multiplicity analyses which are planned to be performed with the T2 detector in the near future is given in section 5.7.

5.1 Analysis definitions

The charged particle pseudorapidity density is defined as the mean number of charged particles per single pp collision and unit of pseudorapidity η. The measurement refers to primary charged particles with $5.3 < |\eta| < 6.4$, for inelastic pp collisions at $\sqrt{s} = 7$ TeV, where at least a primary particle is generated in this pseudorapidity range. Primary charged particles are defined as charged particles with a mean lifetime $\tau > 0.3 \times 10^{-10}$ s, directly produced in pp interactions or in subsequent decays of particles having a shorter lifetime. This is consistent with the ATLAS [92], ALICE [93] and CMS [50] definition of a primary charged particle. With this definition the decay products of the K_s^0 and Λ hadrons are considered secondary particles, together with all of the charged particles generated by interactions with the material in front and around T2. According to the studies on the primary particle P_T acceptance, reported in sec. 3.7.2, only primary particles with $P_T \geq 40$ MeV/c have been considered. The fraction of charged particles with $P_T < 40$ MeV/c produced in the T2 acceptance is nevertheless predicted to be very small ($\sim 1\%$).

5.2 Data and MC samples

The data sample used for the present analysis consists of 150,000 pp collisions at $\sqrt{s} = 7$ TeV recorded in May 2011 during a low pile-up run at standard optics (β^* = 1.5 m). Each beam was composed of six bunches with an average luminosity per colliding bunch pair of about $8 \times 10^{27}\,\mathrm{cm^{-2}\,s^{-1}}$, corresponding to an inelastic pile-up probability of $\sim 3\%$. More details about the pile-up probability measurement are given in section 5.3.1. The rate of beam gas interactions for such beam conditions is negligible. Indeed a measurement of beam gas interaction probability has been done in runs with similar bunch population and vacuum conditions by using a data sample where the trigger is generated on a non-colliding bunch. The fraction of beam gas events with respect to the real pp events was found to be of the order of 1/1000, therefore no correction due to beam gas interaction is needed.

The T2 plane, from the trigger point of view, is divided in 8(radial direction)x13(azimuthal direction) trigger sectors, each one being associated to a "superpad". A superpad is composed by 15 neighbouring pads, disposed on an area covering 3(radial direction)x5(azimuthal direction) pads of the T2 plane. The trigger required at least one “trigger-road”, defined as a group of at least 4 superpad ON in different planes of the same quarter and in the same r-ϕ trigger sector, to be active. This condition is expected to be satisfied if at least one primary charged particle traverses the T2 detector. A sketch of the trigger roads available in each quarter of the T2 detector is reported in fig. 5.1.

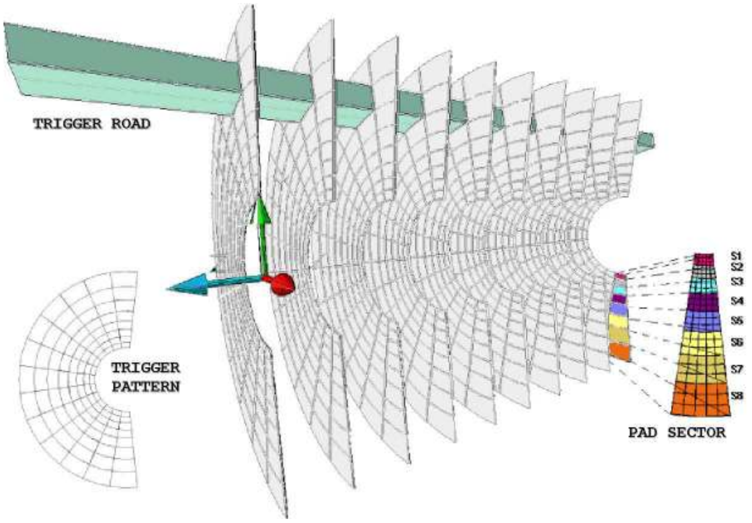

Figure 5.1: Trigger patterns used by the T2 detector. The 1560 pads of the readout plane are grouped in 104 superpads (left side). A logical combination of a minimum number of collinear superpads (trigger road) can be chosen in order to trigger the event. The grouping in 8 superpads (S1...S8) of a sector of 120 pads (read by a single VFAT) is shown on the right side. Each readout plane has 13 sectors like this one [60].

The plane efficiency and the noise level for this run have already been reported in sec. 3.4 and 3.3.2, while more details on the effect that trigger inefficiency has on the measurement will be given in sec. 5.3.2. Only the triggered events where at least one track has been reconstructed have been included in the analysis sample. With these conditions, the visible cross section seen by T2 has been estimated to be about 95% of the total inelastic cross section. This is based on the comparison of the direct measurement of the T2 visible inelastic cross section (to be published) to the TOTEM inelastic cross section measurement deduced from the difference between the total and elastic cross sections [4]. The fraction of the total inelastic cross section detected by T2 obtained from Pythia 6.42 [17] and Pythia 8.108 [94] MCs are in agreement with the above estimate. According to these generators the T2-triggered sample contains more than 99% of all non-diffractive events and single and double diffractive events having at least one diffractive mass larger than ~ 3.4 GeV/c^2

[64]. It is worthy to remark the larger acceptance, for the detection of the inelastic events, that the TOTEM detectors have with respect to the other LHC experiments. As an example, CMS, ATLAS and ALICE have their diffractive mass range starting at $\sim 7\,\mathrm{GeV/c^2}$. Because of the TOTEM larger visible cross section, the difference in the normalisation between the TOTEM $\mathrm{dN_{ch}/d}\eta$ and the one obtained with a full acceptance detector is expected to be small.

5.3 Analysis procedures

5.3.1 Pile-up probability

The incidence of the event pile-up on the sample used for the analysis has been estimated by using the luminosity measured by CMS. For each of the six bunches composing the fill of the analysed run the following relation holds:

$$\mu = L_{bb} * \sigma_{inel}/f_{LHC} \tag{5.1}$$

where μ is the average number of inelastic events which occur during the crossing of the selected bunch pair. L_{bb} is the bunch pair luminosity measured by CMS, σ_{inel} is the inelastic cross section and f_{LHC} is the frequency of the bunches. The measurement of L_{bb} as a function of time is reported in fig. 5.2, for the six bunches[1].

For each bunch, the number of events is described by a Poissonian distribution $P(n)$ with mean μ. The pile-up probability $P_{pile-up}$ of a given bunch pair, defined as the probability to have an extra event when at least an inelastic interaction occurs, is therefore given by:

$$P_{pile-up} = \frac{(1 - P(0) - P(1))}{1 - P(0)} \tag{5.2}$$

By making an average of the six $P_{pile-up}$ values of the different bunch pairs, a ~3% of pile-up probability was estimated, which means an overall correction factor on the $\mathrm{dN_{ch}/d}\eta$ measurement of about 0.97. The validation of this method has been done by using a different fill where, for the same bunch, both a bunch crossing trigger and the luminosity determination by CMS were provided[2]. This allows to compare the pile-up probability estimation obtained with an analysis based on the CMS luminosity with the one which

---

[1] We thank Jiri Procházka for providing us the CMS measurements.

[2] Apart for this check, these bunches have not been used for the $\mathrm{dN_{ch}/d}\eta$ measurement because of the higher bunch-bunch luminosity ($P_{pile-up}$ ~5%) with respect to the average $P_{pile-up}$ of the six bunches reported in the text.

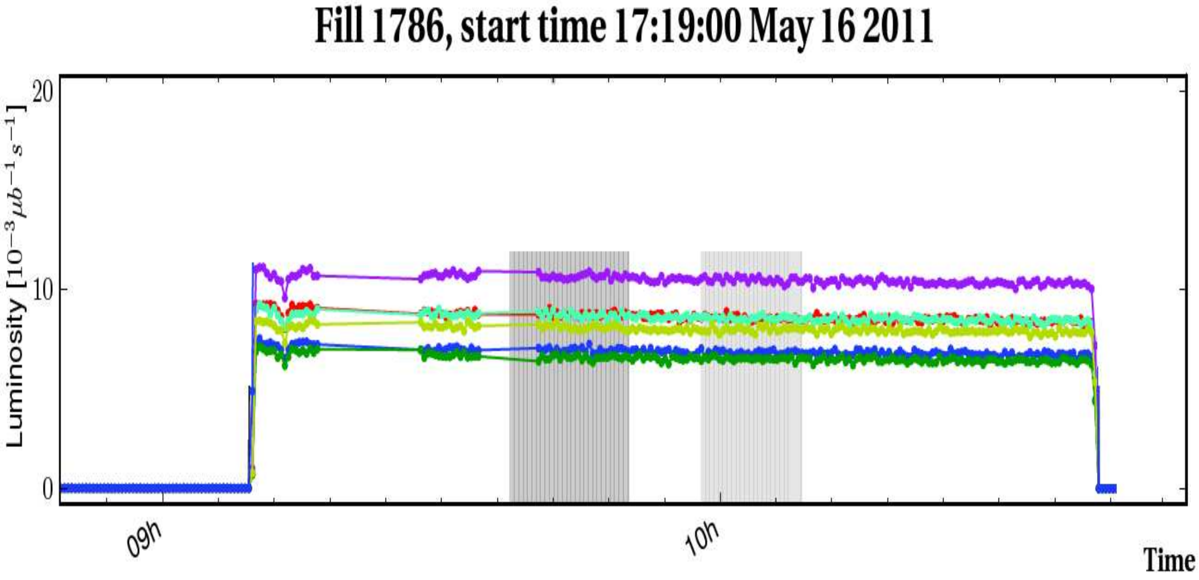

Figure 5.2: Luminosity of the bunch pairs as a function of time, measured by CMS.

can be derived from the data. The pile-up estimation can be obtained from the data by measuring the probability to have 0 tracks in the bunch crossing triggered event. This measurement, $P(0)$, allows to extract μ from the Poissonian formula thanks to the relation $P(0) = e^{-\mu}$. The value of $P_{pile-up}$ can be therefore obtained from eq. 5.2. The discrepancy between the two results on the pile-up probability was found to be 0.4%. Conservatively, the systematic uncertainty assigned to the pile-up effect was taken as 1%.

5.3.2 Trigger inefficiency

The effect of the trigger bias on the $\mathrm{dN_{ch}}/\mathrm{d}\eta$ measurement has been evaluated by comparing the $\mathrm{dN_{ch}}/\mathrm{d}\eta$ measured with a pure bunch crossing trigger with the one obtained when the T2 standard trigger is used for recording the events of the same bunch. For both samples at least a reconstructed track (see sec. 5.2) is required. More detailed studies have shown that the inefficiency of the T2 trigger is mainly due to low multiplicity events, where the tracks have a large angle so that the trigger condition is not satisfied. These tracks are nevertheless reconstructed by the offline algorithms. The bias introduced by the trigger inefficiency on the $\mathrm{dN_{ch}}/\mathrm{d}\eta$ is related to have a low selection efficiency for low multiplicity events. Therefore the $\mathrm{dN_{ch}}/\mathrm{d}\eta$ measurement obtained with the triggered sample is expected to be higher, on average, with respect to the one obtained with the bunch crossing trigger. This effect is shown in fig. 5.3, where the $\mathrm{dN_{ch}}/\mathrm{d}\eta$ measurement is obtained for one quarter (without including many of the analysis corrections) with the same analysis procedure for the two samples. The bias introduced by the trigger was found to be around 1% and it is included as a systematic uncertainty.

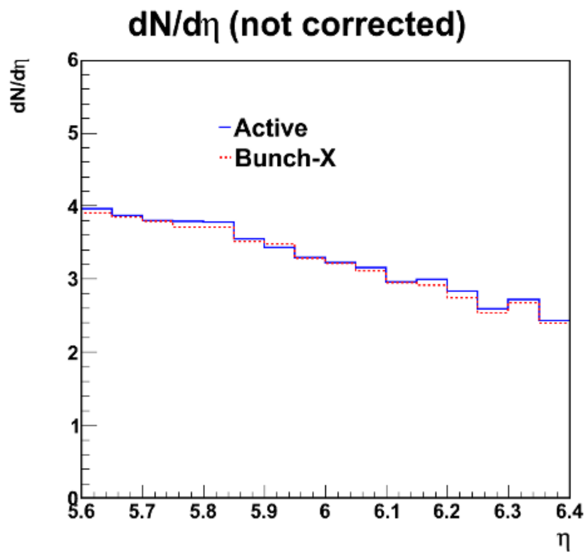

Figure 5.3: Effect of the trigger bias on the $dN_{ch}/d\eta$ measurement. The dashed curve obtained with a data sample triggered on bunch crossing is compared to the solid one, where data are selected with the standard T2 trigger.

5.3.3 Separation of primary and secondary tracks

Since about 80% of the T2 reconstructed tracks are due to secondaries[3], it is important to have a procedure for the discrimination between them and the ones related to primary charged particles. Primary track candidates are required to have a χ^2-probability greater than 1%. The ZImpact track parameter, proven to be the most stable against misalignment errors, it is extensively used for the primary to secondary tracks separation. A loose condition on the Z_{min} parameter, $Z_{min} \cdot \mathrm{sign}(\eta) < 13.5\,\mathrm{m}$ is also required to select the primary tracks. This condition was included to reduce the contribution of secondary tracks in the ZImpact range where the primaries are selected. Indeed, from Phojet MC simulation it has been found that such a condition allows to remove ∼7% of the secondary tracks at $|\mathrm{ZImpact}| < 5$ m, with a negligible effect on the primary track efficiency[4]. The plot of Z_{min}

---

[3] This approximate fraction has been obtained from the data sample used in the analysis, as the ratio between the number of tracks having a ZImpact not included in the range where the primaries are selected and the total number of tracks. In this estimation, the contribution of the secondary tracks expected in the forementioned ZImpact range has been also taken into account.

[4] The net effect that the condition $Z_{min} \cdot \mathrm{sign}(\eta) < 13.5\,\mathrm{m}$ has on the full track sample is the reduction of the amount of secondary tracks by about 60%

vs ZImpact track parameters is shown in fig.5.4 for both primary and secondary tracks reconstructed in simulated pp inelastic events.

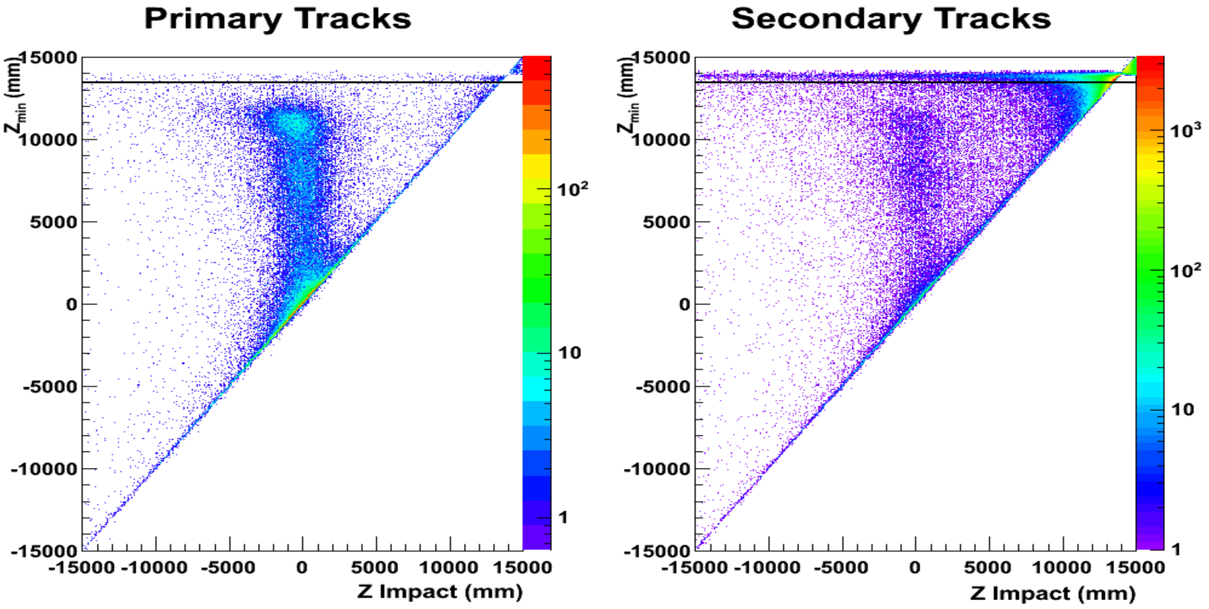

Figure 5.4: Z_{min} vs ZImpact for tracks reconstructed in the PN quarter for primary tracks (left) and secondary tracks (right), according to the Phojet MC. The black line is drawn at $Z_{min} = 13.5$ m.

From MC studies it has been found that the ZImpact distribution associated to the primary tracks is symmetric around ZImpact $= 0$, with a shape that can be described by a double-Gaussian. The distribution of the tracks associated to the secondaries increases as ZImpact gets closer to the Z-value of the detector position, with a maximum reached at a ZImpact corresponding to the detector position. The ZImpact distributions for primary and secondary tracks are shown in fig. 5.5.

More detailed studies have shown that the ZImpact distribution of the secondary tracks reconstructed in high multiplicity events (for which the average pad cluster multiplicity per quarter is larger than 50) can be described by an exponential distribution in the range ZImpact $<$ 9 m[5], while for lower multiplicity events an increase of this distribution around $|$ZImpact$| = 0$ is found. This is due to the decay products of strange particles like K0s and Λ and to single photon conversions in the material close to the detector. Since most of the decay or convertion products have only one reconstructed track, it is not possible to reconstruct the associated secondary vertex where the particle decays (strange hadrons) or

---

[5] This range is valid for a quarter of the plus arm. In the minus side secondary tracks are described by an exponential for ZImpact $>$ -9 m.

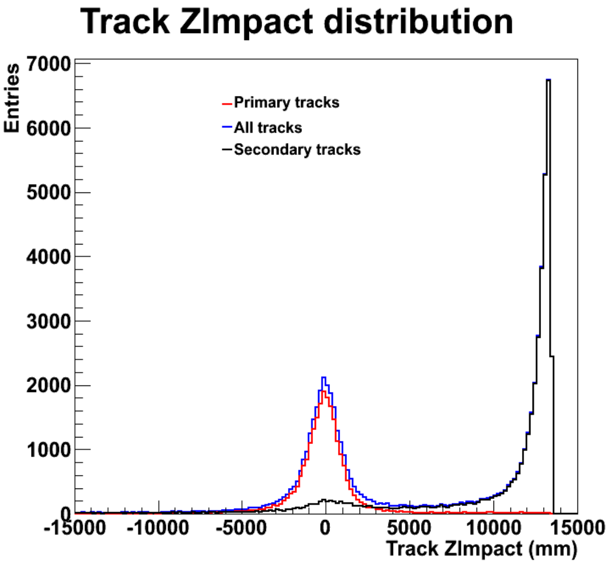

Figure 5.5: Track ZImpact distribution for Phojet inelastic pp events. The contribution of the primary tracks (red line) and of the secondary tracks (black line) is shown. The blue curve is the cumulative distribution. The cut on the track Z_{min} has been already applied.

produces an e^+-e^-pair (photons). Therefore this contribution cannot be separated from the primary one by means of more refined selection cuts to be applied on the data. In order to estimate this contribution, an opportune MC-based analysis has been developed (see sec. 5.3.4). The secondary track ZImpact distribution for low and high multiplicity events, obtained for all tracks of the PN quarter with $\eta > 5.6$, is shown in fig. 5.6.

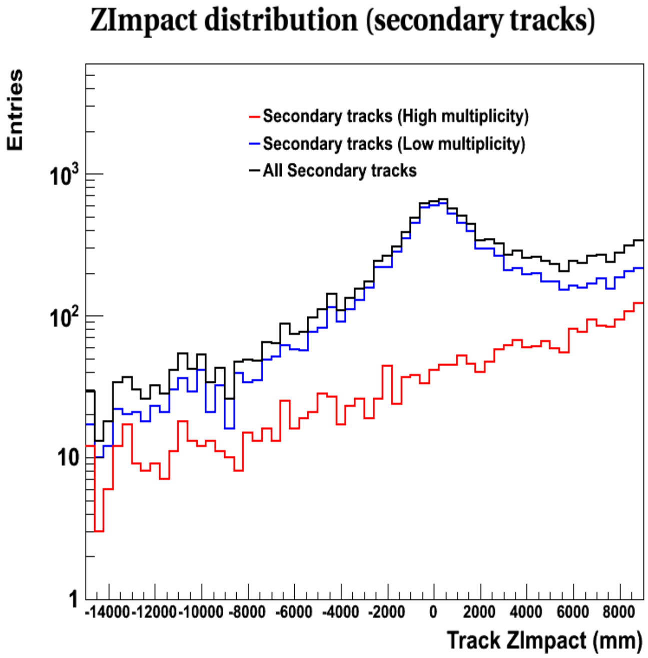

Figure 5.6: Secondary track ZImpact distribution reconstructed in the PN quarter for low multiplicity events (blue curve) and high multiplicity events (red curve).

The track ZImpact distribution measured on data is therefore fitted with a double Gaussian, allowing to describe most of the primary particles, and with an exponential distribution for the secondaries. Since the fit results have been found to be η-dependent, the fit has been repeated for each η-bin that is used for the pseudorapidity distribution evaluation (see sec. 5.4). In the fit procedure the mean is required to be the same for both Gaussians and it is left as a free parameter of the fit. The standard deviation and the amplitude of the two Gaussians as well as the mean and the amplitude of the exponential function have also been considered as free parameters. The standard deviations of both Gaussians have been found to increase with η, while the Gaussian amplitudes decrease with η. The relative abundance of secondary particles is defined, for each η-bin, as B/(S+B) where S is the integral of the Gaussian in a range which includes 96% of its area and B is the integral of the exponential function in the same range. This quantity has been found to decrease with $|\eta|$.

The track ZImpact distribution, with the exponential and double Gaussian fit, is shown in fig. 5.7 where the tracks are reconstructed in one T2 quarter in the $5.8 < \eta < 5.85$ range. The left picture refers to a MC simulation, the right one is obtained from data. The ZImpact range defining the 96% coverage of the double Gaussian area is different for data and simulation: data have been found to cover larger ranges depending on the bin pseudorapidity. The typical 96% range found in the data is between 4.2m and 7m, while in simulation it is between 3.4m and 4.5m. As an example, in fig. 5.7 the ZImpact ranges are [-3.8 m,3.8 m] and [-4.4 m,4.4 m] for simulation and data respectively. Such a discrepancy, more marked at higher η, can be due to residual misalignment effects and to a worsening of the resolution because of the higher event multiplicity that data have with respect to the MC.

The primary tracks are selected in the data by requiring the reconstructed ZImpact to be in the range for which the area covered by the double Gaussian is 96% of the total, while Z_{min} has to fulfil the condition $Z_{min} \cdot \text{sign}(\eta) < 13.5\,\text{m}$. These two conditions will be hereafter referred to as "primary selection cuts". From this sample, the contamination of the secondary tracks has to be evaluated and subtracted. The fraction of pure primary tracks, among the ones passing the above selection criteria, was calculated for each η-bin as a function of the ZImpact value using the double Gaussian function ($G(\eta$,ZImpact)) and the exponential ($E(\eta$,ZImpact)) fits. Indeed, the probability that a reconstructed track with a particular value of ZImpact and η is associated to a primary particle is given by

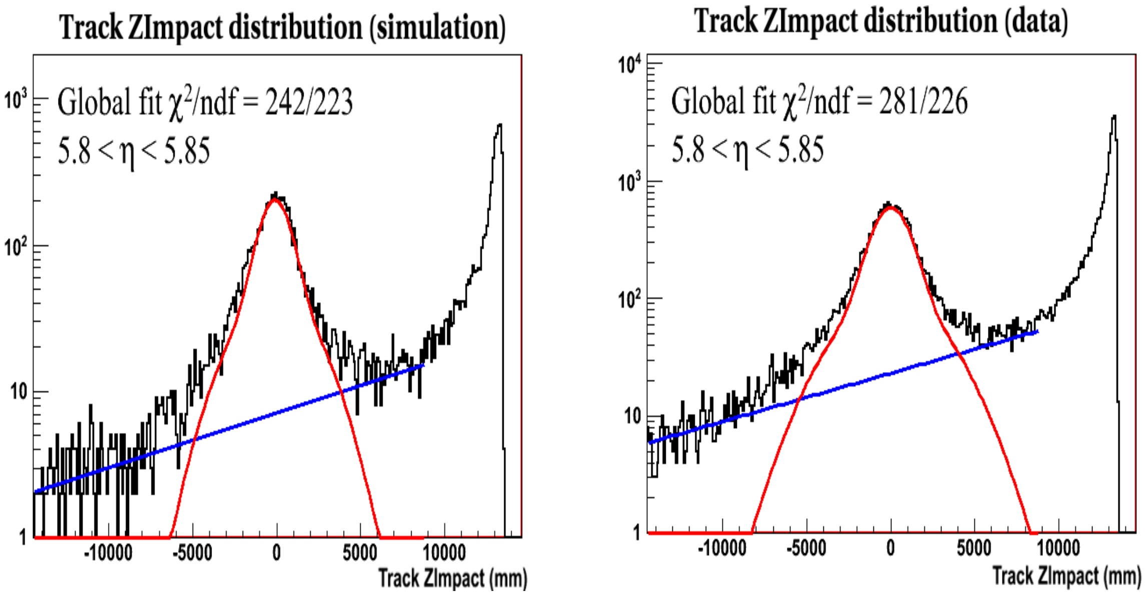

Figure 5.7: ZImpact parameter distribution for tracks reconstructed in one T2 quarter with $5.8 < \eta < 5.85$. The reported χ^2/ndf refers to the global (double Gaussian + exponential) fit, performed in the range from -15 m up to 9 m. The blue curve represents the exponential component due to secondaries, while the red curve is the double Gaussian component mainly related to primary tracks. The left and the right pictures are obtained from tuned Pythia 8 MC and data, respectively.

$W(\eta$,ZImpact), which is defined as:

$$W(\eta, ZImpact) = \frac{G(\eta, ZImpact)}{G(\eta, ZImpact) + E(\eta, ZImpact)} \tag{5.3}$$

The average value of W has been found to range from about 75% (lower $|\eta|$ bins) to about 90% (higher $|\eta|$ bins). The systematic error on the S/(S+B) ratio, which is the quantity of interest for the dN$_{\mathrm{ch}}$/dη measurement, is calculated by repeating the fit where the values of the normalisation constants and of the variances of the double Gaussian are imposed to be 1σ[6] larger (or smaller) with respect to their nominal values. The variation of the corresponding S/(S+B) was found to be 2-3%.

The uncertainty on the χ^2-probability requirement ($\chi^2 - p > 1\%$), previously introduced as one of the requirement in the primary track selection, has been estimated to be around 1% by evaluating the data/MC discrepancy observed with and without using this requirement.

---

[6] σ indicates the statistical error on the fitted parameter.

5.3.4 Contamination of the primary tracks sample

The overall contribution of the secondary tracks to the double Gaussian peak has been determined by using different MC generators. It was found to range between 6% and 13% according to Phojet 1.12 [95], Sherpa 1.3.0 [96] and Pythia 8.108 [94]. The larger contribution is predicted by the Pythia MC, while Phojet predicts the smaller one. The following steps were implemented in order to correct the $dN_{\mathrm{ch}}/d\eta$ measured on data for the non exponential secondary contribution:

- Secondary tracks were selected from the MC samples and their ZImpact distribution was fitted with a function which is the sum of an exponential and a double Gaussian, as explained in the previous section. The secondary peak fraction "P_F" was defined by:

  $$P_F = \frac{N_{SecPeak}}{N_{Tot}}\Big|_{ZImpact@96\%} \tag{5.4}$$

  where $N_{SecPeak}$ is the area of the secondary peak above the exponential function and N_{tot} is the integral of the secondary track distribution. Both quantities were evaluated using only tracks having a ZImpact in the range where the primary particles are selected, as explained in the previous section.

- Then for each bin centred at η_0 the function $S_p(\eta_0)$ is defined:

  $$S_{p_0}(\eta) = \frac{dN_{\mathrm{ch}}/d\eta(\eta_0)|_{prim}}{dN_{\mathrm{ch}}/d\eta(\eta_0)|_{prim} + dN_{\mathrm{ch}}/d\eta(\eta_0)|_{sec} \cdot P_F \cdot C} \tag{5.5}$$

  where $dN_{\mathrm{ch}}/d\eta|_{prim}$ and $dN_{\mathrm{ch}}/d\eta|_{sec}$ are the primary and secondary tracks $dN_{\mathrm{ch}}/d\eta$ predicted by the MC (obtained from tracks where the primary track selection cuts have been applied) and C is a correction factor that is introduced in order to tune the normalisation of the $dN_{\mathrm{ch}}/d\eta|_{sec}$ with the measurements published by other LHC experiments.

- For each bin centred at η_0 the $dN_{\mathrm{ch}}/d\eta$ measurement, as obtained from data with the method reported in sec. 5.3.3, is multiplied by the factor $S_p(\eta_0)$.

In order to have a better estimation of $dN_{\mathrm{ch}}/d\eta|_{sec}$, the MC generated K^0_S dN/dη and γ dN/dE were normalised to reproduce, in their acceptance region, the measurements reported by CMS [97] and LHCf [98]. The factor C of eq. 5.5 is therefore different from 1 only for the contributions to the $dN_{\mathrm{ch}}/d\eta|_{sec}$ given by K^0_S and γ. To calculate C for the K^0_S contribution, the quantity $dN/d\eta|_{K0}/dN_{\mathrm{ch}}/d\eta|_{prim}$ measured by CMS has been linearly extrapolated to the T2 pseudorapidity region. This was found to be $\sim$2% smaller with respect to prediction obtained from Phojet and Pythia MC. The ratio between the predicted γ dN/dE with respect to the one measured by LHCf is 1.6 and 1.2 for Pythia and Phojet MC generator[7], respectively. This ratio is assumed to have the same value also in the T2 acceptance region. The systematic error on the S_p correction factor was taken half of the size of the variation obtained when the different generator predictions on S_p are compared. This has been found to contribute between 1% to 3% to the final $dN_{ch}/d\eta$ measurement, being larger for smaller η.

5.3.5 Primary track efficiency

The primary track efficiency has been obtained from MC studies, as reported in sec. 3.6.4.1. It has been evaluated as a function of the average pad cluster multiplicity (APM), for each pseudorapidity bin with size 0.05. The reconstructed track was required to have at least 3 pads shared with the GEANT primary track and to satisfy the primary selection cuts. Moreover, a $\chi^2 - p$ greater than 0.01 was required. This quantity, $\epsilon(\eta,\text{APM})$, was calculated for each quarter and was found to be above 80% at the APM found in the data ($\sim$24).

The systematic uncertainty associated to the primary track efficiency has been evaluated for each quarter separately in studies where tracks were reconstructed using a set of n detector planes ($n < 10$). Here, for each event two sets of tracks were reconstructed, one set had tracks reconstructed only from these n planes (the reference sample), while in the other (the tested sample) the track reconstruction was obtained from the complementary $10 - n$ planes. A condition on the track pseudorapidity, $|\eta| > 4.5$, was required for tracks in the reference sample, in order to mainly select the primary candidates. For each track of the reference sample, a compatible track in the tested sample was searched. The i-th track T_{Ri} of the reference sample is considered successfully reconstructed if exists a track T_{Tj} in the tested sample such that the following condition holds:

$$D_X < 3\sigma_{DX} \qquad \text{and} \qquad D_Y < 3\sigma_{DY} \tag{5.6}$$

where D_X and D_Y are the X and Y distances between a hit of T_{Tj} and the point extrapolated from T_{Ri}. σ_{DX} and σ_{DY} are the uncertainties on these distances. The above condition needs to be valid for at least two hits of T_{Tj}.

The tested sample efficiency ϵ_{TS} is defined as the probability that a track of the reference

---

[7] Since Sherpa predicts an intermediate value of the non exponential secondary fraction, this MC has not been considered anymore for the correction of the non exponential background.

sample can be associated to one of the tested sample, according to the condition defined in eq. 5.6. Fig. 5.8 shows the comparison between ϵ_{TS} measured on data and on pp MC simu-

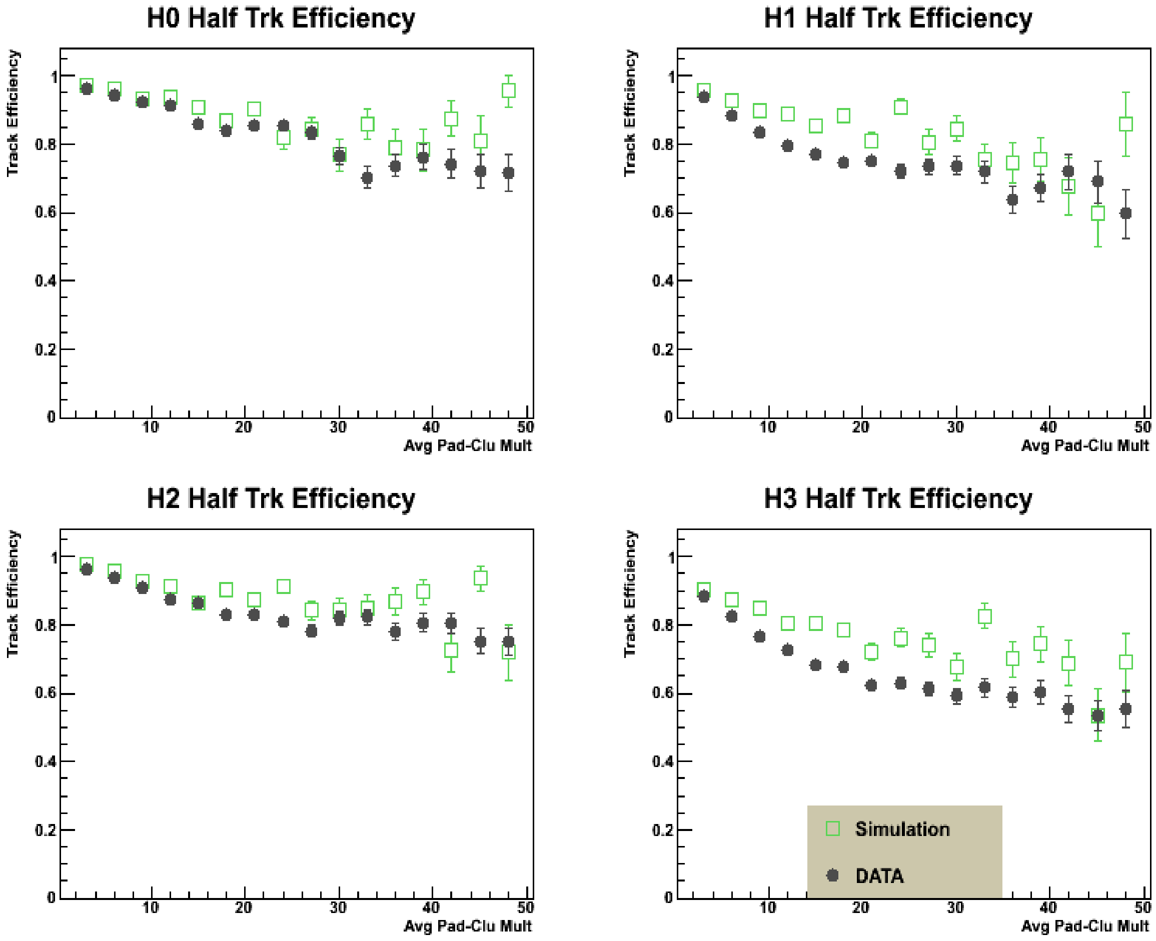

Figure 5.8: Half sample track efficiency (ϵ_{TS}) obtained from data (grey circles) and simulation (green squares) as a function of the average pad cluster multiplicity, for the four quarters of the T2 detector.

lation, using five detector planes in the reference sample (n =5) and five in the tested one. The systematic uncertainty on ϵ(η,APM) has been estimated with the procedure previously described as the difference between the ϵ_{TS} obtained on data and the one from MC. This uncertainty, computed as a function of the data pad-cluster multiplicity and of the track η measured in the data, has been found to give a relative contribution from 1 to 7 %.

The primary track efficiency variation due to magnetic field effects and to the uncertainty on the energy spectrum have been evaluated by means of MC studies. The effect of the magnetic field has been tested by switching it ON and OFF, while the energy spectrum of all the simulated particles has been varied by 50%[8]. The primary track efficiency has been again evaluated and the resulting uncertainty on the $\mathrm{dN_{ch}}/\mathrm{d}\eta$ measurement given by these contributions was found to be about 2%.

5.3.6 Events with showers

Events characterised by a high hit multiplicity, typically due to showers generated in interactions with the material, were not included in the analysis. The events were selected looking at the average pad cluster multiplicity per plane (APM) of the quarter under study. If it is larger than 70, the primary track efficiency described in sec. 5.3.5 is measured to be lower than $\sim$15% in at least a pseudorapdity bin. In this case the event is discarded from the analysis sample. The fraction of discarded events, where track reconstruction capability is limited, constitutes about 11% of the data sample available for the analysis of the single quarter. The effect of not considering these events has been evaluated with a MC study. Since (see sec. 5.6) Sherpa and Pythia8 MC generators are able to contain the measured $\mathrm{dN_{ch}}/\mathrm{d}\eta$, they are used for the estimation of this correction. The correction is estimated by measuring the generator primary charged particle $\mathrm{dN_{ch}}/\mathrm{d}\eta$ both for the MC sample that would be discarded due to its high APM value ($\mathrm{dN_{ch}}/\mathrm{d}\eta_D$) and for the complementary MC sample ($\mathrm{dN_{ch}}/\mathrm{d}\eta_A$) at lower multiplicity. The same event selection used in the data has been applied. The comparison of the two generator curves, obtained with the Sherpa MC, is shown in fig. 5.9.

The correction factor "H", to be applied on the measured $\mathrm{dN_{ch}}/\mathrm{d}\eta$, is given by:

$$H = 1 + \alpha \left(\frac{dN_{\mathrm{ch}}/d\eta_D}{dN_{\mathrm{ch}}/d\eta_A} - 1 \right) \tag{5.7}$$

where α is the fraction of events discarded in the analysis, as measured in the data. By combining the Sherpa and Pythia8 MC predictions, an average value of H of 1.02 has been found. The uncertainty on this correction factor has been estimated to be about 1% from the difference between the two MC predictions.

---

[8] The CMS experiment reported a discrepancy, that increases with $|\eta|$, between data and Pythia inelastic event simulation [82]. Pythia underestimates the energy flow in the CMS HF calorimeter, measured in the pseudorapidity range $3.15 < |\eta| < 4.9$. The effect of this discrepancy on the reported analysis has been taken into account using a dedicated simulation, where the input energy spectrum of the particles has been increased according to the extrapolated energy flow discrepancy expected in the $5.3 < |\eta| < 6.5$ region. Conservatively, in the evaluation of this contribution to the systematic uncertainties, all particles in the T2 region have been set with a 50% higher energy.

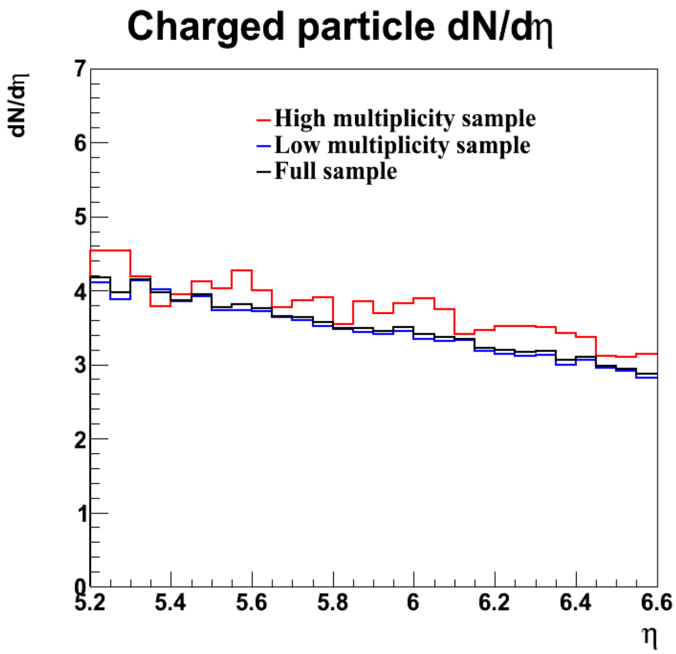

Figure 5.9: MC charged particle dN$_{\mathrm{ch}}$/dη obtained with Sherpa. The black curve is related to all generated events. The red and blue ones give, respectively, the $dN_{\mathrm{ch}}/d\eta_D$ and $dN_{\mathrm{ch}}/d\eta_A$ distributions.

5.3.7 Bin migration and acceptance effects

To take into account the effect that a finite track pseudorapidity resolution has on the measured dN$_{\mathrm{ch}}$/dη, a "bin migration correction" procedure was derived. This was obtained by a MC pp simulation where the η of the reconstructed primary tracks in a particular pseudorapidity bin (η_{j-REC}) is expressed as a sum of the pseudorapidities of the corresponding GEANT track sample (η_{i-GEN}):

$$\eta_{j-REC} = \sum_i B_{ji}\, \eta_{i-GEN} \tag{5.8}$$

where B_{ji} is the probability that a track reconstructed in the j-th pseudorapidity bin was originated from a GEANT tracks with its η in the i-th pseudorapidity bin. The values of the B_{ji} function are reported in fig. 5.10. As shown here, the correction to apply on each bin is small, so the choice of a bin size of 0.05, used for the pseudorapidity density measurement, is appropriate.

MC studies also provided the fraction of primary charged particles which do not arrive in the T2 detector. The associated correction factor, in average $\sim$1.04, has been calculated for each η bin in events with at least one charged particle in the $5.3 < |\eta| < 6.4$ range, by considering the number of primary GEANT tracks crossing the detector and the corresponding number of primary charged particles generated at the IP with P$_T >$ 40 MeV/c.

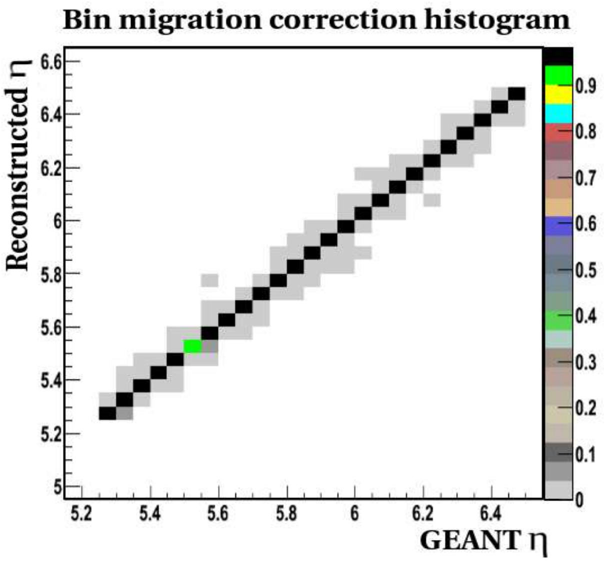

Figure 5.10: Reconstructed tracks pseudorapidity of each η-bin (Y-axis) vs pseudorapidities of the corresponding sample of GEANT tracks (X-axis). The bin migration correction function is extracted from here.

This correction factor, $G(\eta)$, allows to correct for geometrical acceptance effects and for inelastic interactions of primary particles during their propagation and to make the $\mathrm{dN_{ch}}/\mathrm{d}\eta$ measurement representative for events with at least a primary charged particle in the the pseudorapidity acceptance $5.3 < |\eta| < 6.4$. The variation of the $G(\eta)$ function with the MC generators has been found to be around 2%, which is taken as the systematic error on $G(\eta)$. The bin migration functions (B_j) have instead shown a negligible dependence on the generator.

5.3.8 Misalignment effects

The analysis has been performed using the best estimates of the internal and global misalignment parameters, already reported in ch. 4. Eventual biases related to the internal alignment parameters are expected to be taken into account by including the tracking efficiency uncertainty (see sec. 5.3.5). In order to evaluate the systematic uncertainty due to the global alignment corrections, the Δ_α and Δ_β alignment parameters have been varied around the optimal values within their resolution (0.3 mrad). The effect of the uncertainty on the ΔX and ΔY shift parameters has been found to be less relevant for this analysis. The data have been again reconstructed and analysed for the different misalignment configurations. The corresponding variation in the $\mathrm{dN_{ch}}/\mathrm{d}\eta$ results defined the systematic uncertainty due to the misalignment corrections. In particular, the full variation of the pseudorapidity distribution due to the global misalignment has been found to be $\sim$ 2%, 6%, 5% and 3% for the PN, PF, MN and MF quarters respectively. These values are obtained as the average variation of the $dN_{ch}/d\eta$ distribution over the pseudorapidity range $5.3 < \eta < 6.4$. The effect of the misalignment uncertainty on the ZImpact and on the $dN_{ch}/d\eta$ distributions is reported in fig. 5.11, for the MF quarter. The black line shows the configuration found by the alignment algorithm. The green bands are the results obtained by varying the tilt parameters according to their uncertainties. The misalignment configurations giving a clearly distorted ZImpact distribution were omitted from the plot. For the raw $dN_{ch}/d\eta$ distribution of fig. 5.11 a unique ZImpact cut at 6 m was used and no analysis correction was applied. As expected, a more marked dependence of the $dN_{ch}/d\eta$ on the misalignment corrections is found at high $|\eta|$.

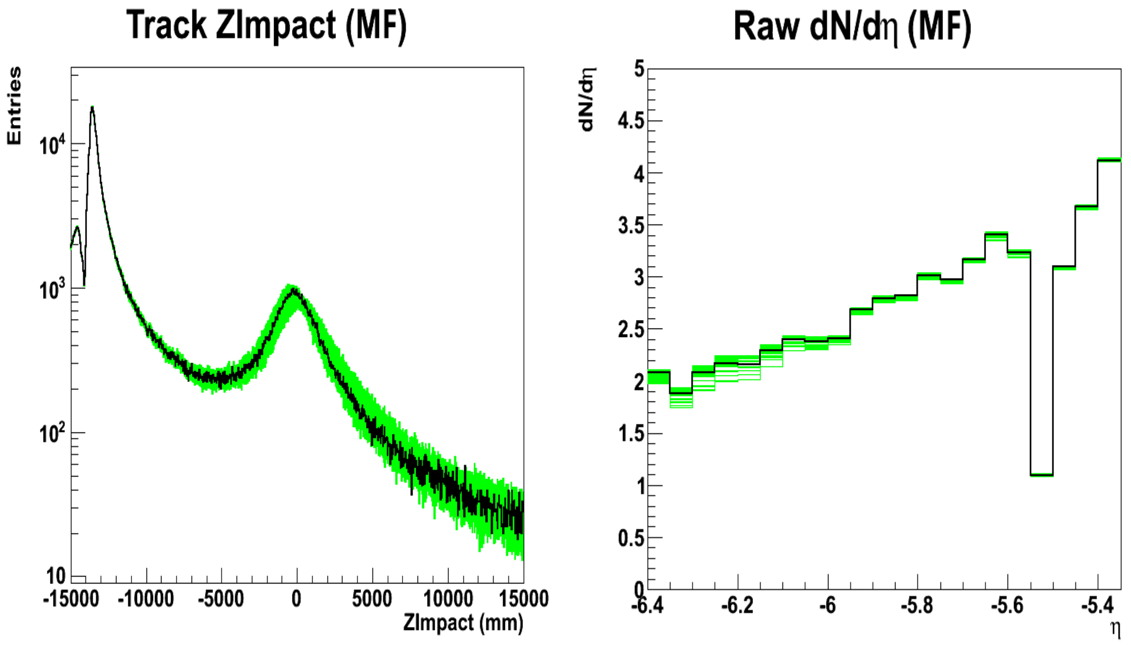

Figure 5.11: The effect of the misalignment uncertainty on the track ZImpact distribution (left) and on the raw $dN_{ch}/d\eta$ distribution (right). The black curve is the preferred configuration, the green band represents the distributions obtained by varying the misalignment parameters within their uncertainty.

5.4 Correction procedure

The pseudorapidity density has been measured for each quarter independently, allowing an important consistency check among the four analysis results, as each quarter differs in its alignment and track reconstruction efficiency. The track η_{IMP} will be used as the best estimator of the particle pseudorapidity, thanks to its smaller variance (see sec. 3.6.4.2) with respect to the track η defined from the track polar angle. For events where large showers didn't occur (see sec. 5.3.6), the primary tracks are selected by requiring a χ^2-p $> 1\%$ and a ZImpact and Z$_{min}$ parameter compatible with the primary selection criteria reported in sec. 5.3.3. The $W(\eta$,ZImpact) function introduced in in sec. 5.3.3 allows each data track to be weighted by the probability for the track to be primary, according to its η and ZImpact-value. Each track has then been weighted for the primary track efficiency $\epsilon(\eta$,$m)$ according to its η and to the pad-cluster multiplicity m in the corresponding quarter (see sec. 5.3.5). The pseudorapidity distribution of the primary candidates is then corrected for the contribution of the non-exponential background, estimated as a function of η with the $S_p(\eta)$ function (see sec. 5.3.4). The procedure for the bin migration correction is then applied in order to correct the distribution for biases due to the finite track resolution. This is obtained by expressing the pseudorapidity of the tracks of the i-th bin with a sum of the originating GEANT pseudorapidity $\sum_j B_j(\eta)$ (see sec. 5.3.7). The acceptance correction and the normalisation of the measurement to the events with at least a primary charged particle in the $5.3 < |\eta| < 6.4$ is taken into account with the introduction of the $G(\eta)$ function (see sec. 5.3.7).

The distribution is then corrected with a factor P which allows to take into account for the pile-up probability (see sec.5.3.1) and with a factor H to take into account the effect that the exclusion of the events with high secondary multiplicity has on the measurement (see sec. 5.3.6). Finally the measurement is normalized to the full azimuthal acceptance, by correcting the measurement with a factor $2\pi/\Phi$.

Eq. 5.9 was used for the dN$_{\rm ch}$/dη determination:

$$\left.\frac{dN_{\rm ch}}{d\eta}\right|_{\eta=\eta_0} = \sum_{{\rm Trk}\in S} \frac{W(\eta_0, ZImpact)\ \sum_j B_j(\eta_0)}{\epsilon\,(\eta_0, m)\ \Delta\eta\ N_{\rm Ev}}\ G(\eta_0)\ S_p(\eta_0)\ \frac{2\pi}{\Phi}\ H\ P \tag{5.9}$$

where η_0 is the η-value of the bin centre, S is the sample of tracks with $\eta_0 - \Delta\eta/2 < \eta < \eta_0 + \Delta\eta/2$ satisfying the selection criteria described above, $\Delta\eta = 0.05$ is the bin width, $N_{\rm Ev}$ is the number of events in the data sample.

5.5 Summary of the systematic uncertainties

Table 5.1 shows as an example the uncertainties of the bin centred at $\eta_0 = 6.025$, for the PF quarters. The double dashed line separates the uncertainties which are quarter dependent (top) from the ones in common for all the quarters (bottom). The total systematic uncertainty reported in tab. 5.1 has been computed by first linearly adding the global alignment and track efficiency systematics, to take into account possible effects that misalignment can have on the primary track efficiency estimation. Then this result has been added in quadrature to the uncertainty contributions from 4) to 10) of tab. 5.1 and finally the uncertainty associated with the non-primary contribution to the central peak has been added linearly. This last uncertainty is indeed evaluated from MC simulations (even if the two main sources of secondaries was tuned with the available data), from which a preferred model cannot be selected. Therefore a conservative strategy has been adopted in order to combine the resulting uncertainty. To obtain the total uncertainty of the single quarter measurement, the statistical error[9] is then added in quadrature.

Table 5.1: Summary of the relative uncertainties in the bin centred at $\eta_0 = 6.025$ in one of the T2 quarters. The first two contributions are quarter dependent.

$\eta_0 = 6.025$ dN$_{\text{ch}}$/dη error summary (one quarter)	
1. Primary track efficiency	4%
2. Global alignment	3%
3. Non-primaries in the central peak	2%
4. Primary to secondary separation	2%
5. B-field and energy spectrum	2%
6. Primaries not arriving in T2	2%
7. Track quality criterion	1%
8. Trigger bias	1%
9. Pile-up probability	1%
10. Events with high secondary multiplicity	1%
11. Statistical	0.7%
Total (single quarter measurement)	10%

5.6 Results

The dN$_{\text{ch}}$/dη measurements obtained for the different T2 quarters are compatible within the quarter-dependent systematic uncertainties. Fig. 5.12 shows the four pseudorapidity distributions obtained from the independent analysis of each quarter.

---

[9] The positive correlation (close to 1) between the number of selected tracks in the numerator of eq. 5.9 and the number of events in the denominator is taken into account for the statistical error evaluation.

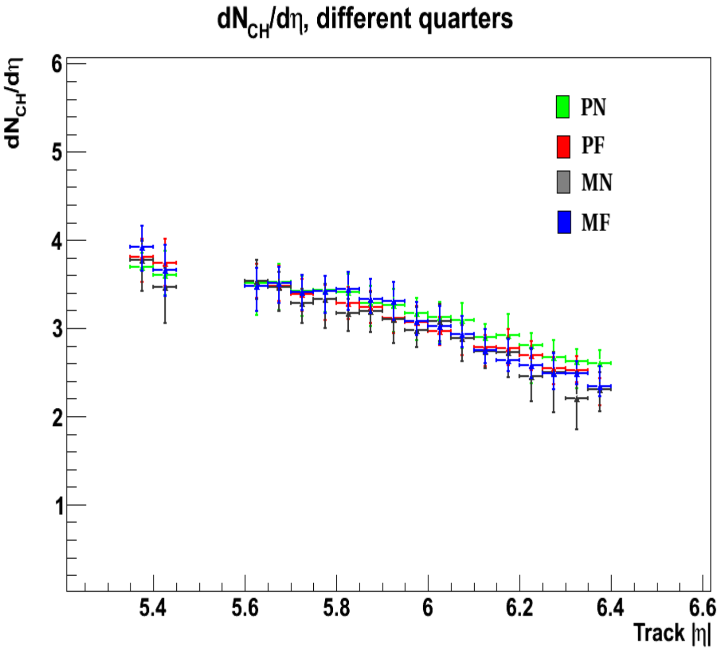

Figure 5.12: $\mathrm{dN_{ch}}/\mathrm{d}\eta$ distribution obtained independently for each quarter.

To obtain a single estimation of the $\mathrm{dN_{ch}}/\mathrm{d}\eta$, for each η-bin the measurements of the four quarters are combined with a weighted average, which is evaluated considering only the quarter dependent contributions to the quarter $\mathrm{dN_{ch}}/\mathrm{d}\eta$ uncertainty. A conservative approach has been adopted for the combination of the quarter-dependent systematic uncertainties: an error propagation on the weighted averages has been applied, considering the measurements completely and positively correlated. The resulting error has then been combined with the systematic contributions that are common to all quarters and with the statistical one, as in the case of the single quarter measurement. The pseudorapidity bins at the edges of the T2 detector, where large corrections due to the reduced geometrical acceptance are needed, are not reported here, nor are the three bins in the $5.425 \leq |\eta| \leq 5.625$ range, where large corrections should be applied because of the interaction of the primary particles with the beam pipe. The pseudorapidity density measurement is shown as red squares in fig. 5.13 where the error bars represent the total uncertainty including the statistical error. The comparison of the data with some MC expectations is also shown. Phojet 1.12 (red triangles) estimates a ∼30% (∼20%) lower $\mathrm{dN_{ch}}/\mathrm{d}\eta$ than measured at $|\eta| = 5.3$ (6.4). Both Pythia 8.108 with default tune (blue circles) and Pythia 6.42 D6T (green circles) estimate a ∼20% (∼12%) lower $\mathrm{dN_{ch}}/\mathrm{d}\eta$ than measured at $|\eta| = 5.3$ (6.4). Sherpa 1.3.0 with default tune (orange diamonds) is in agreement with the data for $|\eta| < 5.9$, while it estimates a higher $\mathrm{dN_{ch}}/\mathrm{d}\eta$ by ∼25% at $|\eta| = 6.4$.

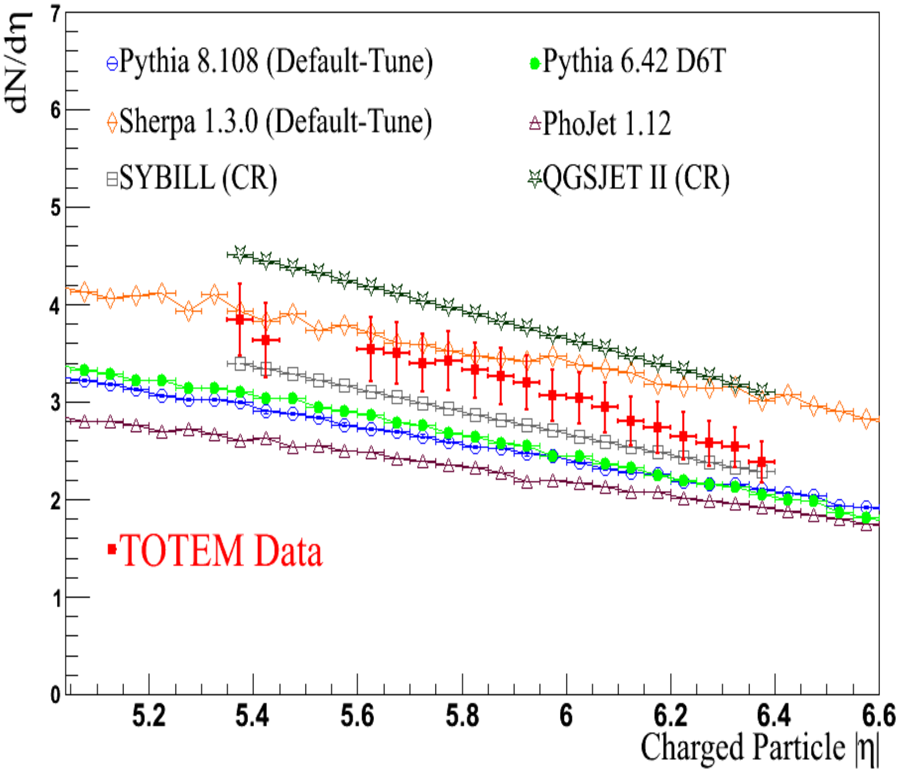

Figure 5.13: Charged particle pseudorapidity density distribution. The experimental points (red squares) represent the average of the four T2 quarters, with the error bars including both the statistical and the systematic error. Violet triangles, blue circles and orange diamonds show, respectively, the Phojet, Pythia8 and Sherpa predictions for charged particles with $P_T >$ 40 MeV/c in events where at least one charged particle is generated in the $5.3 < |\eta| < 6.5$ range. The QGSJET II (green stars) and the SYBILL (gray squares) predictions, obtained within the same requirements, are also superimposed.

When these generators are used to predict the $\mathrm{dN_{ch}}/\mathrm{d}\eta$ of the ATLAS [92], ALICE [93], CMS [50] and LHCb [99] experiments in their own η acceptance, a similar relation between the data and the MC $\mathrm{dN_{ch}}/\mathrm{d}\eta$ normalisations is obtained[10]. Cosmic ray MC generators have also been compared to the data[11]: these are found to better describe the slope of the measured $\mathrm{dN_{ch}}/\mathrm{d}\eta$. SYBILL [100] predicts a 4-16% lower $\mathrm{dN_{ch}}/\mathrm{d}\eta$, while QGSJET-I [101], QGSJET-II [102] and EPOS [103] predict a 18-30% higher $\mathrm{dN_{ch}}/\mathrm{d}\eta$.

---

[10] The data-MC comparison can be obtained by using the CERN website: http://mcplots.cern.ch/

[11] We thank R. ULRICH and C. BAUS for providing us the cosmic ray MC curves.

The $dN_{ch}/d\eta$ measurement is also reported in table 5.2 for each η-bin with the corresponding systematic and statistical error.

Table 5.2: TOTEM $dN_{ch}/d\eta$ measurement for inelastic pp events at $\sqrt{s}$ =7 TeV. The reported values represent the average for the four T2 quarters, with the corresponding systematic (syst) and statistical (stat) error. η_0 represents the central pseudorapidity value in each η bin.

η_0	$dN_{ch}/d\eta$	syst	stat
5.375	3.84	0.37	0.01
5.425	3.64	0.38	0.01
5.625	3.54	0.33	0.01
5.675	3.50	0.32	0.01
5.725	3.40	0.30	0.01
5.775	3.42	0.31	0.01
5.825	3.32	0.29	0.01
5.875	3.27	0.29	0.01
5.925	3.20	0.28	0.01
5.975	3.07	0.27	0.01
6.025	3.04	0.26	0.01
6.075	2.94	0.26	0.01
6.125	2.80	0.25	0.01
6.175	2.74	0.26	0.01
6.225	2.65	0.24	0.01
6.275	2.58	0.23	0.01
6.325	2.53	0.21	0.01
6.375	2.38	0.21	0.01

5.7 Outlook

The TOTEM experiment has measured the charged particle pseudorapidity distribution in pp collisions at $\sqrt{s} = 7$ TeV for $5.3 < |\eta| < 6.4$ in events with at least one reconstructed track in this range. This extends the measurements performed by the other LHC experiments to this previously unexplored forward η range. A collection of 7 TeV pp inelastic pseudorapidity density measurements, performed from the LHC experiments is reported on fig.5.14. The comparison between these measurements is not straightforward since they differ in the experimental P_T acceptance, visible cross section and requirements on the used track sample. The measurement refers to charged particles with $P_T >$ 40 MeV/c and

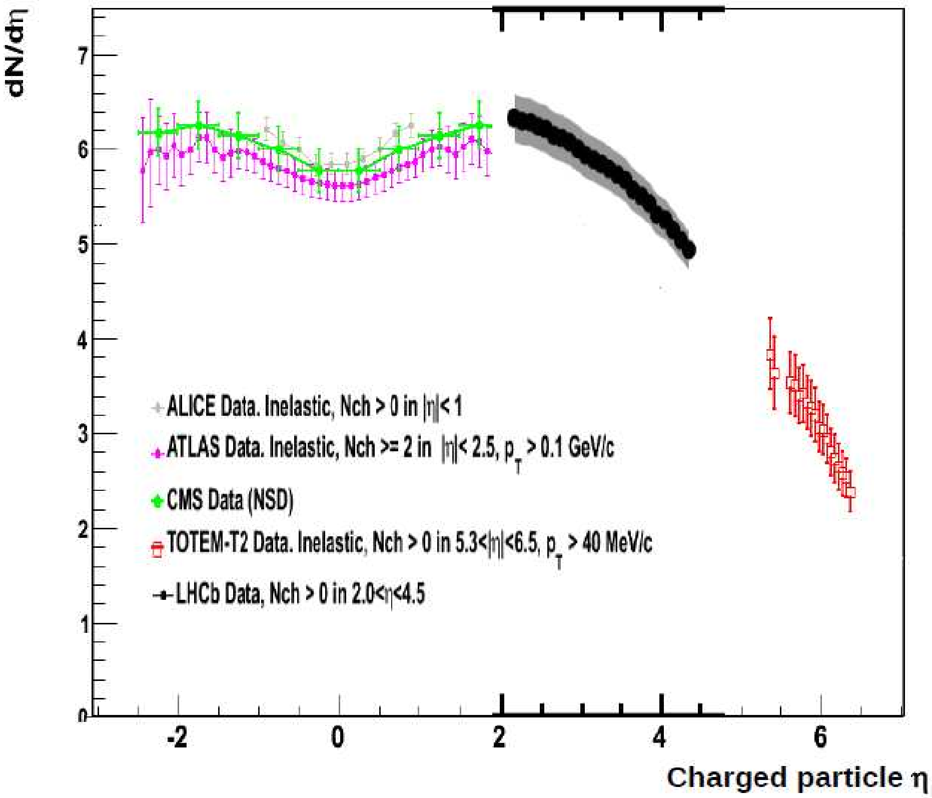

Figure 5.14: ALICE, ATLAS, CMS, LHCb and TOTEM pseudorapidity density measurements for pp inelastic events at 7 TeV.

with a mean lifetime $\tau > 0.3 \times 10^{-10}$ s, directly produced in pp interactions or in subsequent decays of particles having a shorter lifetime. A preliminary measurement of the T2 visible inelastic cross section confirms that about 95% of the inelastic pp events have been considered in the present study. This comprises more than 99% of non-diffractive processes and the single and double diffractive processes with diffractive masses above $\sim$3.4 GeV/c^2. The pseudorapidity density has been found to decrease with increasing $|\eta|$, from 3.84 ± 0.01(stat) ± 0.37(syst) at $|\eta| = 5.375$ to 2.38 ± 0.01(stat) ± 0.21(syst) at $|\eta| = 6.375$. Several MC generators have been compared to data; none of them has been found to fully describe the measurement.

The same analysis is planned to be repeated also for the 8 TeV pp data and for different classes of soft inelastic events (single diffraction, double diffraction, non diffractive and central diffractive events). Moreover, thanks to the implementation of a common CMS-TOTEM trigger system, there is the possibility to extend these studies to events where jets are produced in the CMS acceptance and more in general, to start detailed studies of the underlying event properties in the forward region.

The possibility to extend this measurement for Pb-Pb and p-Pb events is under investigation; the analysis is expected to be more challenging due to the high density of tracks expected in these events [104]. Data from a special run with a collision vertex z position $\sim$ 11.25 m far away from the nominal IP are also available, allowing to measure the forward $dN_{ch}/d\eta$ in the range $6 < |\eta| < 7.3$ and $3.5 < |\eta| < 4.7$, at least on one side of the T2 detector. The investigation on the feasibility of this study is ongoing. There is also interest in the measurement of the track multiplicity, for the different classes of soft inelastic events. To do that, a proper unfolding procedure should be implemented and this will require a better tuning of the MC used for the analysis. There is also room for reducing the systematical uncertainty. The use of several iterations of the track finding procedure can help to reduce the primary track inefficiency and to improve the track ZImpact resolution. A more granular estimation of the plane efficiency will also help in this sense. The systematic error due to the contamination of the primary sample from secondary tracks is expected to be reduced from the new available tuning of the MC generators which include the most up to date measurements from other LHC experiments as LHCf, LHCb, and the forward region of CMS.

Conclusions

When I started my Ph.D. program, the installation of the first quarter of the TOTEM T2 telescope in the LHC tunnel was ongoing. The following months of data taking and commissioning constituted a very interesting period during which we started to understand the detector performance and the LHC background. After this period of detector commissioning on the LHC data, an extensive work on algorithm development and optimisation was performed which finally led the T2 detector to be ready for physics analyses.

The simulation was reviewed and a more realistic representation of the background level seen in the T2 data was obtained, while the detector response was tuned in order to reproduce the measured efficiency and cluster size. In order to cope with the large amount of secondary particles seen in the T2 telescope, which constitute 90% of the whole signal, more performant hit and track reconstruction algorithms were developed. The tracking algorithm is based on a Kalman filter procedure, in a simplified implementation due to the small amount of material traversed by the particle when crossing the 10 GEM planes of a quarter and to the low local magnetic field in the T2 region. An event detection efficiency larger than 99% was obtained for inelastic processes having at least a charged particle in the T2 acceptance. The primary track selection efficiency, which also depends on the quarter occupancy and on the particle energy, was found to be larger than 80% at the average data occupancy. When releasing the primary selection cuts, the primary track efficiency was found between 95 and 99%, as estimated by using a simulation tuned with the data. A primary particle η resolution better than 0.04 was achieved by using a track η definition based on the average of the pseudorapidities of the segments joining the IP to the transverse position of the track hits in each T2 plane. This η definition was found to provide a better resolution with respect to the one obtained when the reconstructed polar angle is used.

The determination of the detector misalignment was another fundamental task which needed to be accomplished in order to perform the analysis reported in this thesis. For instance, due to the short lever arm of the T2 detector (~ 40 cm) compared to its distance from the IP ($\sim$ 14 m), the reconstructed Z position of the vertex can be shifted by meters if a quarter is affected by a rotation of the order of 1 mrad. Without the implementation of these alignment corrections the primary selection capability would be extremely reduced and the pseudorapidity density analysis would not be possible. Two different algorithms were developed, allowing to resolve the relative transverse positions of the planes in a quarter with an uncertainty of $\sim 10\mu m$; the quarter alignment with respect to the IP was achieved by using the "shadow" of the beam pipe and two iterative algorithms which exploit the properties that the primary tracks parameters, should have. The systematic uncertainty of the quarters shifts and tilts were estimated to be 1 mm and 0.3 mrad respectively. An optimised hit position correction procedure was introduced in order to minimise the biases that the misalignment corrections can introduce due to the finite and inhomogeneous spatial resolution of the reconstructed hits.

Today the four quarters of the telescope are fully operative and T2 has been used to carry out the first analysis on the inelastic interactions published by the TOTEM Collaboration and presented in this thesis: the *measurement of the forward charged particle pseudorapidity density in* pp *collisions at* $\sqrt{s} = 7$ *TeV*. Furthermore, by using also the T2 detector, the collaboration has already completed the analyses of the inelastic cross section measurement and the measurement of the total cross section with the luminosity-independent method.

The measurement of the very forward pp $dN_{ch}/d\eta$ reported in this thesis represents the most forward pseudorapidity density measurement ever obtained at a collider.

Since a complete description of the soft hadron interactions based on solid theoretical ground is still missing, experimental measurements like the $dN_{ch}/d\eta$ are highly valuable being a guide for the phenomenological models which try to describe these processes. Especially in the forward region the uncertainties are more pronounced since a large amount of measurements, obtained in the past experiments and used for the tuning of the models, is available only for the central pseudorapidity range. In addition, precise measurements of the forward particle multiplicity are expected to improve the analyses on very high energy cosmic rays (CR), which heavily rely on the MC description of the showers generated when a CR interacts in the atmosphere.

The $dN_{ch}/d\eta$ analysis reported in this thesis has been performed on a low luminosity run triggered with T2. It has been found that the visible cross section seen by T2 is about 95% of the total inelastic cross section. In particular, more than 99% of non diffractive events and diffractive ones with mass larger than 3.4 GeV/c^2 are included in the analysis sample. Since the misalignment and efficiency corrections are quarter dependent, the analysis was performed independently for each quarter and the results were then combined. The main systematic uncertainty was due to the track efficiency and to the detector misalignment corrections. The contamination of the sample of the primary tracks due to the secondary particles also introduced an important systematic uncertainty. The final measurement has been obtained with a systematic uncertainty of about 10%. The pseudorapidity density has been found to decrease with increasing $|\eta|$, from 3.84 ± 0.01(stat) ± 0.37(syst) at $|\eta| = 5.375$ to 2.38 ± 0.01(stat) ± 0.21(syst) at $|\eta| = 6.375$. Several MC generators have been compared to data: Pythia and Phojet were found to underestimate the data, which are between the predictions obtained with the MC generators commonly used in CR analyses. CR generators predict a slope of the $dN_{ch}/d\eta$ distribution which is more compatible with the measured one. In particular, while QGSJET II overestimates the measurement, the SYBILL prediction, which is systematically below the data, is compatible within the experimental error.

In the near future, the same analysis will be repeated also for the 8 TeV pp data sample and for different classes of soft inelastic events (single diffraction, double diffraction, non diffractive and central diffractive events). Moreover, thanks to the possibility of a common CMS-TOTEM trigger system, there is the possibility to extend these studies to events where jets are produced in the CMS acceptance, and more in general, to start a detailed investigation of the underlying event properties in the forward region. The possibility to extend this measurement to p-Pb events is under investigation. Here this analysis is expected to be more challenging due to the higher density of tracks with respect to the pp case. Data from a special run with a collision vertex position at z $\sim$ 11.25 m from the nominal IP are also available. This data sample will allow to measure the forward $dN_{ch}/d\eta$ in the ranges $6 < |\eta| < 7.3$ and $3.5 < |\eta| < 4.7$, in one side of the T2 detector. This measurement can be compared with the one that will be obtained by T1 in the range $3.1 < |\eta| < 4.7$.

There is also room for reducing the systematical uncertainties: the use of several iterations of the track finding procedure can help to reduce the primary track inefficiency and to improve the ZImpact resolution; a more granular estimation of the plane efficiency is also expected to reduce the systematic uncertainty on the tracking efficiency; the systematic error due to the contamination of the primary sample by secondary tracks can be reduced by using the most recent tuning of the MC generators which will include the most up to date measurements from experiments like LHCf, LHCb, and the forward region of CMS.

Acknowledgements

At the end of my Ph.D. experience it is a great pleasure to thank everyone who helped me during these years.

I would like to thank my advisors and tutor: thanks to Dr. G. Latino and Dr. S. Lami for the time they have spent in the correction of this thesis and for the fruitful discussions we had on my work during these years. Without their help this document would not be in the shape it is today. I'm indebted to Prof. A. Scribano who introduced me in the TOTEM experiment at CERN and who is the founder member of our "Pisa-Siena" TOTEM group.

I want also to thank Dr. E. Oliveri for his contagious enthusiasm in approaching the problems, it was very nice to work with you. Let me also thank Dr. N. Turini for the many hints he gave me on the "mysterious T2 detector". To all the group, thank you again for your guidance and for this opportunity.

I would like to express my gratitude to the colleagues at CERN. In particular to Dr. S. Giani, for his precious help during this analysis and in the offline algorithms design. Thanks also to Prof. K. Österberg for the continuous feedback on the analysis results, always greatly appreciated during these four years in TOTEM.

Thanks also to Prof. K. Eggert for all the questions asked and for the instructive observations on my results. Thanks to Dr. V. Avati, for the valuable discussions we had during the software meetings.

My sincere thanks go also to the younger colleagues, in particular Dr. F. Ferro, Dr. J. Kašpar, Dr. H. Niewiadomsky and Dr. L. Grzanka, always willing to help in any technical aspect of the work. Thanks also to Dr. S. Bonechi and Dr. P. Brogi for having created a friendly work environment in the department.

Finally I want to thank Elena and my mother for their love, patience and support during these years.

Thanks to all of you.

Appendix

.1 Rapidity and pseudorapidity

For a particle of energy E and momentum component along z p_z, the rapidity y is defined as:

$$y = \frac{1}{2} ln \frac{E + p_z}{E - p_z} \Rightarrow \frac{p_z}{E} = tanh(y) \tag{10}$$

This quantity, which in the non relativistic limit reduces to the particle velocity along z, is frequently used as one of the kinematical variable of the collision process. This is because it transforms additively under a Lorentz boost along the z direction. Indeed for a boost of β along the z direction:

$$(E, p_T, p_z) \to (\gamma(E + \beta p_z), p_T, \gamma(p_z + \beta E)) \quad \text{and} \quad y \to y + \frac{1}{2} ln \frac{1 + \beta}{1 - \beta} \tag{11}$$

By defining $m_T = \sqrt{m^2 + p_T^2}$ and being $E = \sqrt{m_T^2 + p_z^2}$, the following relations hold:

$$p_z = m_T \, sinh(y) \quad \text{and} \quad E = m_T \, cosh(y) \tag{12}$$

For $m = 0$, eq. 10 reduces to:

$$y = \frac{1}{2} ln \frac{1 + \cos\theta}{1 - \cos\theta} = -ln tan \frac{\theta}{2} \equiv \eta \tag{13}$$

Therefore the pseudorapidity η is a good approximation of the rapidity for high relativistic particles. However, especially in the very forward region, the difference between the two variables can be pronounced. This is shown in fig. 15, where y is compared to η for simulated pions at energy of 10 and 100 GeV. Indeed, using $p_Z = p \, \cos\theta$ and $p = \beta \, E$:

$$y = \frac{1}{2} ln \frac{1 + \beta \cos\theta}{1 - \beta \cos\theta} \tag{14}$$

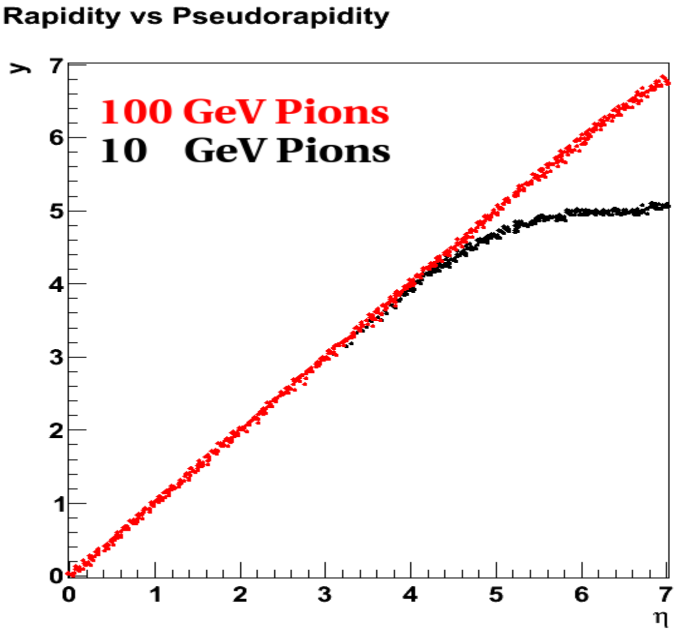

Figure 15: Rapidity vs pseudorapidity for pions generated at E=10 (black curve) and E=100 (red curve) GeV.

Therefore the relation tanhη=tanhy/β can be used in order to express y as a function of η, for different energies of the particle. Rapidity is also useful for the description of the kinematics in the parton-parton scattering. Supposing that hadron A and B have, in the hadron center of mass frame (laboratory frame) the four-momentum $P_A = (E_a, 0, 0, p_a)$ and $P_B = (E_b, 0, 0, -p_a)$ respectively, the center of mass frame of the interacting partons with four-momenta $p_1 = x_1 P_B$ and $p_2 = x_2 P_B$ (x_1 and x_2 are the longitudinal fraction of momentum of hadron A and B carried by the partons) moves respect to the laboratory frame with β_{cm}:

$$\beta_{cm} = \frac{(x_1 - x_2)}{x_1 + x_2} \Rightarrow y_{cm} = \frac{1}{2} ln \frac{x_1}{x_2} \tag{15}$$

Therefore, when in a parton scattering the system is projected at high rapidity, the small-x part of the parton distribution function can be probed. In particular:

$$\begin{aligned} x_1 &= \frac{1}{2} x_t \left(e^{y_3} + e^{y_4}\right) \\ x_2 &= \frac{1}{2} x_t \left(e^{-y_3} + e^{-y_4}\right) \end{aligned} \tag{16}$$

where $x_T = 2k_T/\sqrt{s}$, k_T being the outgoing parton transverse momentum and y_3, y_4 denote the final rapidities of the scattered partons in the center of mass frame. From this equation, it follows that Di-jet measurements in the same hemisphere of T2/CASTOR acceptance ($5.2 < |\eta| < 6.5$) would probe a x value down to 10^{-6}.

Bibliography

[1] G. Antchev *et al.* (TOTEM Collaboration). *EPL*, vol. 98, p. 31002, 2012.

[2] V. Barone, E. Predazzi. High-energy particle diffraction, Springer, 2002.

[3] R. Castaldi, G. Sanguinetti *ANNUAL REVIEW OF NUCLEAR AND PARTICLE SCIENCE*, vol. 35, pp. 351 – 395, 1985.

[4] G. Antchev *et al.* (TOTEM Collaboration) *EPL*, vol. 96, p. 21002, 2011.

[5] J.R. Cudell *et al.* (COMPETE Collaboration) *Phys. Rev. Lett.*, vol. 89, p. 201801, 2002.

[6] R.J. Eden *Rep. Prog. Phys.*, vol. 34, p. 995, 1971.

[7] M.G. Ryskin, A.D. Martin, V.A. Khoze *Eur. Phys. J. C*, vol. 72, p. 1937, 2012.

[8] A. Donnachie, P.V. Landshoff *Phys. Lett. B*, vol. 296, pp. 227–232, 1992.

[9] M.L. Mangano *PHYS-USP*, vol. 53, pp. 109–132, 2010.

[10] F. Gelis *J. Phys. G*, vol. 34, p. S421, 2007.

[11] V. Fadin *ACTA PHYSICA POLONICA B*, vol. 39, p. 2193, 2008.

[12] J. Breitweg *et al. Eur. Phys. J.* , vol. 67, p. 609, 1999.

[13] L.V. Gribov, E.M. Levin, M.G. Ryskin *PHYSICS REPORTS*, vol. 100, pp. 1–150, 1983.

[14] E. Iancu, A. Leonidov, L. McLerran. hep-ph/0202270, 2002.

[15] A. Dumitru, J. Jalilian-Marian *Physics Letters B*, vol. 547, no. 1-2, pp. 15–20, 2002.

[16] A. Moraes, C. Buttar, I. Dawson *EPJ C*, vol. 50, pp. 435–466, 2007.

[17] T. Sjöstrand, S. Mrenna and P. Skands *JHEP*, vol. 05, p. 026, 2006.

[18] J. Guillaud *CMS-NOTE-2000-070*, 2000.

[19] T. Sjöstrand. Introduction to Monte Carlo Techniques in High Energy Physics, CERN Summer student lectures, July 2012.

[20] B. Andersson, G. Gustafson, G. Ingelman, T. Sjöstrand *Phys. Rep.*, vol. 97, pp. 31–145, 1983.

[21] E. Fermi *Progress of Theoretical Physics*, vol. 5, no. 4, pp. 570–583, 1950.

[22] Y. Hama, T. Kodama, O. Socolowski Jr. hep-ph/0407264, 2004.

[23] Wong Cheuk-Yin. nucl-th/0809.0517, 2008.

[24] E. S. F. Cooper, G. Frye *Phys. Rev. D*, vol. 11, pp. 192–213, 1975.

[25] R. P. Feynman *Phys. Rev. Lett.*, vol. 23, pp. 1415–1417, 1969.

[26] J. F. Grosse-Oetringhaus, K. Reygers *J. Phys. G: Nucl. Part. Phys.*, vol. 37, p. 083001, 2010.

[27] Z. Koba, H.B. Nielsen, P. Olesen *Nucl.Phys.*, vol. B 40, pp. 317–334, 1972.

[28] R.E. Ansorge *et al.* The UA5 collaboration. *Z. Phys.*, vol. C 43, p. 357, 1989.

[29] A. Giovannini, L. Van Hove *Z. Phys.*, vol. C30, p. 391, 1986.

[30] A. Giovannini, L. Van Hove *Acta Phys. Polon.*, vol. B19, p. 495, 1988.

[31] A. Giovannini, R. Ugucccioni *Int. J. Mod. Phys.*, vol. A20, p. 3987, 2005.

[32] G. J. A. *et al.* The UA5 collaboration *Phys. Rept.*, vol. 154, pp. 247–383, 1987.

[33] G. J. Alner *et al.* The UA5 collaboration *Z. Phys.*, vol. C33, pp. 1–6, 1986.

[34] B.B. Back*et al.* The PHOBOS collaboration. *Nucl. Phys. A*, vol. 757, pp. 28–101, 2005.

[35] J. Benecke *et al. Phys. Rev.*, vol. 188, p. 2159, 1969.

[36] W. Busza *Nucl. Phys. A*, vol. 854, no. 1, pp. 57 – 63, 2011.

[37] J.M. Jamal *Phys. Rev. C*, vol. 70, p. 027902, 2004.

[38] Yen-Jie Lee. PhD Thesis, CERN-THESIS-2011-236, 2011.

[39] C.P. Ward *et al. Nuclear Physics B*, vol. 153, no. 0, pp. 299 – 333, 1979.

[40] J. Whitmore *Physics Reports*, vol. 10, no. 5, pp. 273 – 373, 1974.

[41] W. Thomè *et al. Nuclear Physics B*, vol. 129, no. 3, pp. 365 – 389, 1977.

[42] A. Breakstone *et al. Phys. Rev. D*, vol. 30, pp. 528–535, 1984.

[43] C. Albajar *et al. Nuclear Physics B*, vol. 335, no. 2, pp. 261 – 287, 1990.

[44] G. Arnison *et al. Physics Letters B*, vol. 123, no. 1-2, pp. 108 – 114, 1983.

[45] R. Harr *et al. Physics Letters B*, vol. 401, no. 1-2, pp. 176 – 180, 1997.

[46] F. Abe *et al.* (CDF Collaboration) *Phys. Rev. D*, vol. 41, p. 2330, 1990.

[47] S. Clark *et al. Nuclear Physics A*, vol. 544, no. 12, pp. 343 – 356, 1992.

[48] J.F. Sagerer. PhD Thesis, 2008.

[49] B. Abelev *et al.* (STAR Collaboration). *Phys. Rev. C*, vol. 79, p. 034909, 2009.

[50] V. Khachatryan *et al.* (CMS Collaboration) *Phys. Rev. Lett.*, vol. 105, p. 022002, 2010.

[51] V. Berardi *et al.* (TOTEM Collaboration). CERN-LHCC-2004-002; addendum CERN-LHCC-2004-020, 2004.

[52] G. Anelli *et al.* (TOTEM Collaboration) *JINST*, vol. 3, p. S08007, 2008.

[53] P. Aspell *et al.* Proceedings of TWEPP-07, 2007.

[54] J. Kaspar. PhD Thesis, CERN-THESIS-2011-214, 2012.

[55] H. Niewiadomski. PhD Thesis, CERN-THESIS-2008-080, 2012.

[56] F. Sauli *Nucl. Instrum. Methods A*, vol. 386, p. 531, 1997.

[57] S. Lami *et al. Nuclear Physics B*, vol. 172, pp. 231–233, 2007.

[58] M. G. Bagliesi *et al. Nucl. Instrum. Methods A*, vol. 617, no. 13, pp. 134–137, 2010.

[59] B. Ketzer *Nucl. Instr. Meth. A*, vol. 494, p. 142, 2002.

[60] E. Oliveri. PhD Thesis, CERN-THESIS-2010-178, 2010.

[61] F. Ravotti. Proceedings of IEEE-2011 conference, 2011.

[62] M. Berretti. Master Degree Thesis, CERN-THESIS-2008-171, 2008.

[63] W.-M.Yao et al. (Particle Data Group). J. Phys. G 33, 1, 2006.

[64] P. Brogi. Master Degree Thesis, CERN-THESIS-2011-099, 2011.

[65] A. Donnachie, P. V. Landshoff *Physics Letters B*, vol. 387, p. 637, 1996.

[66] M. M. Islam, R. J. Luddy, A. V. Prokudin *Int. J. Mod. Phys. A*, vol. 21, pp. 1–42, 2006.

[67] J. Kaspar *et al. Nucl. Phys. B*, vol. 843, pp. 84–106, 2011.

[68] R. Engel, D. Heck, T. Pierog *Annual Review of Nuclear and Particle Science*, vol. 61, pp. 467–489, 2011.

[69] J. Knappa *Nuclear Physics B (Proc. Suppl.)*, vol. 122, pp. 56–65, 2003.

[70] R.J. Glauber, G. Matthiae *Nucl. Phys. B*, vol. 21, p. 135, 1970.

[71] R. Ulrich, R. Engel, M. Unger *Phys. Rev. D*, vol. 83, p. 054026, 2011.

[72] M.T. Dova, A.A. Watson, A.G. Mariazzi *arXiv:astro-ph/0512408v1*, 2005.

[73] G. Antchev *et al.* (TOTEM Collaboration) *EPL*, vol. 95, p. 41001, 2011.

[74] G. Antchev *et al.* (TOTEM Collaboration) *CERN-PH-EP-2012-239*, 2012.

[75] V. Avati *et al.* Proceedings of 11th ICATPP Conference, 2010.

[76] G. L. Bayatian *et al.* (CMS Collaboration). CERN-LHCC-2006-001, 2006.

[77] S. Agostinelli *et al.* (GEANT4 Collaboration) *Nucl. Instrum. Methods Phys. Res. A*, vol. 506, p. 250, 2003.

[78] R. Veenhof. Garfield - simulation of gaseous detectors,
http://garfield.web.cern.ch/garfield/, 2010.

[79] G. Baur *et al. Physics Reports*, vol. 364, no. 5, pp. 359 – 450, 2002.

[80] R. Mankel *Rep. Prog. Phys.*, vol. 67, p. 553, 2004.

[81] G. Cowan, *Statistical data analysis.* Oxford University Press, USA, 1998.

[82] S. Chatrchyan *et al.* (CMS Collaboration) *JHEP*, vol. 11, p. 148, 2011.

[83] V. Karimki *et al.* CMS-CR-2003-022, 2003.

[84] V. Blobel *Nucl. Instrum. Methods A*, vol. 566, pp. 5–13, 2006.

[85] V. Blobel. Millepede II, http://www.desy.de/ blobel/Mptwo.pdf, 2007.

[86] I. Belotelov,A. Lanyov, G. Ososkov *Physics of Particles and Nuclei Letters*, vol. 3, pp. 261–272, 2006.

[87] P. Z. Skands *Phys. Rev. D*, vol. 82, no. 7, p. 074018, 2010.

[88] M. G. Ryskin, A. D. Martin and V. A. Khoze *Eur. Phys. J. C*, vol. 71, p. 1617, 2011.

[89] R. Engel *Nuclear Physics B (Proc. Suppl.)*, vol. 122, pp. 437–446, 2003.

[90] M. Albrow *et al.* The CMS and TOTEM diffractive and forward physics working group. CERN-LHCC-2006-039-G-124, 2006.

[91] D. D'Enterria *et al. Astroparticle Physics*, vol. 35, pp. 98–113, 2011.

[92] G. Aad *et al.* (ATLAS Collaboration) *New J. Phys.*, vol. 13, p. 053033, 2011.

[93] K. Aamodt *et al.* (ALICE Collaboration) *Eur. Phys. J. C*, vol. 68, p. 345, 2010.

[94] T. Sjöstrand, S. Mrenna and P. Skands *Comput. Phys. Commun.*, vol. 178, pp. 852–867, 2008.

[95] R. Engel *Z. Phys.*, vol. 66, pp. 203–214, 1995.

[96] T. Gleisberg *et al. JHEP*, vol. 0902, p. 007, 2009.

[97] V. Khachatryan *et al.* (CMS Collaboration) *JHEP*, vol. 05, p. 064, 2011.

[98] O. Adriani *et al.* (LHCf Collaboration) *Physics Letters B*, vol. 703, pp. 128–134, 2011.

[99] R. Aaij *et al.* (LHCb Collaboration). CERN-PH-EP-2011-209, 2011.

[100] E.-J. Ahn *et al. Phys. Rev. D*, vol. 80, p. 094003, 2009.

[101] N. Kalmykov and S. Ostapchenko *Phys. Atom. Nucl.*, vol. 56, p. 346, 1993.

[102] S. Ostapchenko *Phys.Rev. D*, vol. 83, p. 014018, 2011.

[103] K. Werner *et al. Phys. Rev. C*, vol. 74, p. 044902, 2006.

[104] K. Aamodt *et al.* (ALICE collaboration). *Phys. Rev. Lett.*, vol. 105, p. 252301, 2010.